THE UNIVERSITY OF QUEENSLAND

AUSTRALIA

Ultra-fast and Ultra-stiff Optical Tweezers

Muhammad Waleed

M.S Information and Mechatronics

A thesis submitted for the degree of Doctor of Philosophy at

The University of Queensland in 2018

School of Mathematics and Physics

Abstract

This thesis describes our efforts to build an ultra-fast and ultra-stiff optical tweezers to be used for many fundamental science, engineering, and biological applications. This thesis is mainly composed of two sections: the first section describes the fundamental Brownian motion theories of an optically trapped particle, the experimental challenges and new techniques to measure it at very short times scales. The second part illustrates the structured illumination of the incident light field to enhance the optical trap stiffness by several orders of magnitude.

In the first part of this thesis, we describe the design procedures to construct a stable and robust customized microscope employing high numerical aperture (1.3) trapping and condenser objectives to trap and track micro/nano-particles with unprecedented high bandwidth. We have developed a customized mechanical design of the microscope which possess heavy structure and provides 6-axis degrees of freedom for relative alignment of objectives having very small 160 μm working distance. The structure is stable enough to measure the motion of the particle as low as close to 1 Hz where mechanical vibrations are of significant concern. Finally, we demonstrate a new split-flipped waveplate based particle tracking scheme which is capable of measuring very high 160 mW of scattered light from the trapped particle resulting in unprecedented ultra-high position measurement bandwidth close to 10 MHz. It allows accessing Brownian motion at very short timescales leading to instantaneous velocity measurement of the particle. These measurements are further used to measure the unknown viscosity of the different fluids at fast timescales.

The second part of the thesis demonstrates the spatial structuring of incident trapping light to create interference in the particle which makes it behave like a beam-splitter. On the contrary to the regular particle scattering phenomenon in which particle changes the direction of incident light, this new type of interferometric technique changes the relative intensity around the optical axis due to the Brownian motion of the particle. This phenomenon enhances the optical trap stiffness for several orders of magnitude especially for the particles larger than incident beam wavelength. These techniques are implemented in a holographic optical tweezers for the particle sizes ranging from $1.5 \sim 10$ μm particle and achieved trap stiffens enhancement by a factor of 27.5 for 10 μm particle. This ultra-fast and ultra-stiff optical tweezers could play a vital role in testing the fundamental physics laws such Maxwell-Boltzmann distribution, quantum ground state cooling, micro-robotics and correct viscosity of the biological fluids, especially in the cell.

Declaration by author

This thesis is composed of my original work, and contains no material previously published or written by another person except where due reference has been made in the text. I have clearly stated the contribution by others to jointly-authored works that I have included in my thesis.

I have clearly stated the contribution of others to my thesis as a whole, including statistical assistance, survey design, data analysis, significant technical procedures, professional editorial advice, financial support and any other original research work used or reported in my thesis. The content of my thesis is the result of work I have carried out since the commencement of my higher degree by research candidature and does not include a substantial part of work that has been submitted to qualify for the award of any other degree or diploma in any university or other tertiary institution. I have clearly stated which parts of my thesis, if any, have been submitted to qualify for another award.

I acknowledge that an electronic copy of my thesis must be lodged with the University Library and, subject to the policy and procedures of The University of Queensland, the thesis be made available for research and study in accordance with the Copyright Act 1968 unless a period of embargo has been approved by the Dean of the Graduate School.

I acknowledge that copyright of all material contained in my thesis resides with the copyright holder(s) of that material. Where appropriate I have obtained copyright permission from the copyright holder to reproduce material in this thesis and have sought permission from co-authors for any jointly authored works included in the thesis.

Publications during candidature

1. M. A. Taylor, M. Waleed, A. B. Stilgoe, H. Rubinsztein-Dunlop and W. P. Bowen," Enhanced Optical Trapping via Structured Scattering," Nature Photonics, vol. 9, no. 10, pp. 669–673, 2015 [1].

2. N. P. Mauranyapin, L.S. Madsen, M. A. Taylor, M. Waleed and W. P. Bowen, "Evanescent single-molecule biosensing with quantum-limited precision," Nature Photonics, vol. 11, no. 8, pp. 477−481, 2017 [2]

Publications included in this thesis

M. A. Taylor, M. Waleed, A. B. Stilgoe, H. Rubinsztein-Dunlop and W. P. Bowen," Enhanced Optical Trapping via Structured Scattering," Nature Photonics, vol. 9, no. 10, pp. 669–673, 2015 [1] is incorporated as part of Chapter 3.

Contributor	Statement of contribution
Muhammad Waleed	Conception and design (40%), Analysis and interpretation (30%), Drafting and production (5%)
Michael Taylor	Conception and design (40%) Analysis and interpretation (50%), Drafting and production (60%)
Alexandar Stilgoe	Conception and design (10%), Analysis and interpretation (10%), Drafting and production (5%)
Halina Rubinsztein-Dunlop	Conception and design (0%), Analysis and interpretation (0%), Drafting and production (10%)
Warwick Bowen	Conception and design (10%), Analysis and interpretation (10%), Drafting and production (20%)

Manuscripts included in this thesis

None.

Contributions by others to the thesis

Apart from original motivation for the project, my primary supervisor Warwick Bowen has provided valuable support in the data analysis and interpretation of the data. My secondary supervisors Lars Madsen and Michael Taylor also provided feedback on a number of experiments, data analysis and proofreading of my thesis.

Statement of parts of the thesis submitted to qualify for the award of another degree

None.

Research Involving Human or Animal Subjects

No animal or human subjects were involved in this research.

Acknowledgements

First and foremost, I am thankful to God for giving me the wisdom to undertake the PhD. Then, I would like to pay my sincere gratitude to my supervisor, Prof. Warwick Bowen for his consistent guidance, motivation and intellectual ideas which put me in the right direction to achieve results. He has been a great mentor and his brilliant scientific approach lead us to achieve good results. I feel very fortunate to work in a group of brilliant people because of him.

My secondary supervisors Dr. Lars Madsen and Dr. Michael Taylor have been a great mentor during my candidature. They also worked with me very hard for building setup, doing experiments and analysis. Dr. Alex Stilgoe has also been very helpful and always open to discussion about my experimental problems and many times gave a valuable feedback. I would also like to thank Catxere Casacio for her help to build detection system and Nicolas Mauranyapin for the fruitful discussion. Also many thanks to the mechanical workshop fellows Dave and Griffo, who fabricated mechanical parts for my optical tweezers. Additionally, I would like to thank especially to Simon Khifets and Akarsh Simha for the fruitful discussion on Brownian motion and Prof. Ping Koy Lam for providing the flipped split waveplate for our experiment. Moreover, many thanks to the school fellows Erick, Yauhen, Marco, Amie, Dave, Varun, Rachpon, Christiaan and Xin for being delightful friends.

I am very grateful to my parents for giving me a wonderful life who supported me throughout and allowed me to go abroad to acquire higher education. I am sure that their prayers have always been a key role to overcome my life goals. Finally, I would like to thank my lovely wife Natasha for being a great companion, giving us a loving daughter Fatmir, and keeping my spirits high throughout the PhD. She took care of me and our daughter above and beyond.

Financial Support

1-The Australian Research Council Discovery Project (contract no. DP140100734).

2-The Air Force Office of Scientific Research and Asian Office of Aerospace Research and Development (grant no. FA2386-14-1-4046).

3-The University of Queensland (UQRTTUIT - UQ Research and Training Tuition Fee Offset and UQI (UQ International) Scholarship).

Keywords Optical Tweezers, bio-optics, biophysics, particle tracking, Brownian motion, ballistic motion, instantaneous velocity, microrheology

Australian and New Zealand Standard Research Classifications (ANZSRC)

ANZSRC code: 020501, Classical and Physical Optics, 70%
ANZSRC code: 029901 Biological Physics, 30%

Fields of Research (FoR) Classification

FoR code: 0205, Optical Physics, 50%
FoR code: 0913, Mechanical Engineering, 50%

Contents

List of Figures

List of Tables

Contributor	Statement of contribution
Muhammad Waleed	Conception and design (40%), Analysis and interpretation (30%), Drafting and production (5%)
Michael Taylor	Conception and design (40%) Analysis and interpretation (50%), Drafting and production (60%)
Alexandar Stilgoe	Conception and design (10%), Analysis and interpretation (10%), Drafting and production (5%)
Halina Rubinsztein-Dunlop	Conception and design (0%), Analysis and interpretation (0%), Drafting and production (10%)
Warwick Bowen	Conception and design (10%), Analysis and interpretation (10%), Drafting and production (20%)

List of Abbreviations

Abbreviations	Description
AFM	Atomic Force Microscopy/Microscope
HPF	High pass filter
DAQ	Data acquisition card
ENTRAPS	Enhanced trapping via structured scattering
SFWP	Split-flipped waveplate
LPF	Low pass filter
TEM	Transverse Electromagnetic
MSD	Mean square displacement
NA	Numerical aperture

List of Symbols

Symbol	Description
E	Electric field
λ	Laser wavelength
ρ	Polarisation
k	Wave vector/Norm
c	Speed of light
r	Particle radius
ω	Light frequency
ε	Permittivity
μ	Permeability
σ	Scattering cross-section
P	Optical Power
n_m	Refractive index of the surrounding medium
m	Refractive index ratio
w	Beam waist
$\hbar$	Plank constant
η	Fluid viscosity
κ	Trap stiffness
Q	Trapping quality factor
x	Particle displacement
I	Light intensity
τ	Measurement time
τ_p	Momentum Relaxation time
τ_f	Fluid interaction time
τ_k	Trap characteristic time
ϕ_f	Fluid interaction equivalent frequency
ϕ_p	Momentum relaxation equivalent frequency

Symbol	Description
ϕ_k	Trap characteristic equivalent frequency
δx	Change in particle displacement
m_p	Mass of the particle
m_f	Mass of the fluid
m_e	Equivalent mass
v_{rms}	Root mean square velocity
k_B	Boltzmann constant
T	Temperature
f	Frequency
ρ_f	Density of fluid
D	Diffusion constant
t	Time
P_x^κ	Position power spectrum
P_v^κ	Velocity power spectrum
$P_x^k(f)_h$	Hydrodynamic position power spectrum
$C_v^\kappa(t)$	Velocity auto-correlation
$C_v^\kappa(t)_h$	Hydrodynamic velocity auto-correlation
$MSD_h^\kappa(t)$	Hydrodynamic mean square displacement

Chapter 1

Introduction

1.1 Background of optical tweezers

Light is the form of energy which has been generally considered only as means of viewing things in the history until the 16^{th} century when Johannes Kepler was looking at a comet in the sky. He noticed that the tail of the comet which comprises hot gases always points away from the sun which led him to think that gases are experiencing some external forces from the solar radiation which was termed as radiation pressure. However, theoretical understanding of the electromagnetic field was quite limited at that time until James Clerk Maxwell proposed the electromagnetic theory of radiation pressure in 1862 predicting that the light has momentum flux which is proportional to the intensity and can be transferred to reflective or absorbing objects resulting in a radiation pressure kick along the propagation direction of light [3].

A few decades later, Nichols, Lebedev, and Hull in 1901 reported the initial experimental observation of the radiation pressure torque acting on a macroscopic mirror attached to a torsion balance [4]. Later on, in 1936, Beth observed the deflection of a birefringent quartz wave plate suspended from a thin quartz fiber after passing the circularly polarized light through it [5]. However, the radiation force per unit area was so small that it was hardly observable which make it impossible to apply in real life applications. However, in 1960, the laser was invented which made it possible to concentrate large optical power into the small area, thus opening a new era of radiation pressure studies.

In 1970, Arthur Ashkin employed a laser beam in a microscope to apply radiation pressure on micron-sized latex particles and observed their acceleration and deceleration [6]. Later on, in 1986, they demonstrated that a tightly focused Gaussian beam creates a high-intensity gradient which can apply a force perpendicular to the optical axis resulting in non-invasive trapping of the particles [7]. This

optical trapping instrument is now called optical tweezers (OT).

1.2 Applications

From the experimental point of view, particles are dispersed in a small fluid chamber in which they undergo free Brownian motion due to the collision of surrounding thermal energy carrying molecules. Einstein postulated that the motion of a particle in a fluid is so random that it is independent of its mass due to which particle undergoes free diffusive motion in a liquid and its velocity cannot be measured at a specific instant of times, rather its mean squared displacement is measurable. In an OT, the motion of a particle is constrained by the optical trap at longer timescales, but at relatively shorter times scale, it diffuses freely in the medium depending upon the diffusion properties. On timescale, this is generally called free diffusion regime. Using back-focal-plane interferometry of the optically trapped particle, its mean squared displacement can be measured with high spatial and temporal resolution [8, 9], therefore, trapped particles has can be used as a probe in several applications such as in classical physics [10–12], nanotechnology [13], quantum physics [14–19] chemistry [20], soft matter [21], Biosensing [22–24] and imaging [25–28].

Especially in biology, it has made possible to do precise measurements such as unbinding force and binding probability for a virus coated bead [29], entropy elasticity of a DNA [30], the binding strength and activation state of single fibrinogen-integrin pairs on living cell [31] the direct observation of base-pair stepping by RNA polymerase [32–35], forces unfolding muscle proteins and RNA hairpins [36–38] and, characteristics of myosin and kinesin motors [39–44].

1.3 Optical tweezers for fast viscosity measurement

Apart from being used as a probe for indirect measurement of many biological phenomena, OT has also been used to do a direct measurement of complex and rare polymer structures to understand their mechanical behaviour at different timescales better. For this purpose, several techniques have been developed to determine the viscoelastic properties of both simple and complex fluids. The most widely used techniques are: diffusing wave spectroscopy [45], video particle tracking microrheology [46], magnetic tweezers [47, 48], atomic force microscopy [49] and optical tweezers [50–53]. For all these cases, techniques can be categorized either active or passive, depending on whether they drive the motion of the suspended particle or their motion is free and can be used to calibrate both position and force in fluids.

In active calibration techniques, an external force field is applied to the particles whereas in passive

techniques only the thermal fluctuations of the fluid's molecules are responsible for displacing the particles. Both types of techniques are based on relating the time-dependent trajectory of the probe to the viscoelastic properties of the surrounding fluid and can be used for position and force calibration both in simple and complex biological environments. Commonly used passive calibrating techniques are based on free diffusive power spectrum [54], mean squared displacement [55], position autocorrelation [56] and equipartition theorem while active calibrating techniques are based on drag force method [57, 58]. Furthermore, a combination of active and passive techniques can be employed to extract the viscoelastic proprieties of complex fluids such as cytoplasm of the cell [59, 60].

Although these techniques allow extracting intracellular information using the probe particle, there are several active phenomena inside the cell which can affect the particle Brownian motion at long times scales yet mimicking the particle undergoing free diffusion. Therefore, information cannot be extracted reliably from the free diffusive motion of the particle. In particular, it has been demonstrated that several active biological systems in a living cell such as actin-myosin interactions create "athermal" fluctuations which take the system away from the thermal equilibrium thus changing the localized viscosity of the fluid at fast times scales. These 'athermal' fluctuations can be present in the entire cell can also influence the equilibrium dynamics of different organelles in the cell and, may alter at different conditions and timescales [61, 62].

Furthermore, several intracellular processes such as protein-protein interaction, polymerization processes, and actomyosin contraction can alter the diffusive properties of the probe particles and can generate active diffusion at timescales from $10-100$ ms which resemble the free thermal diffusion but with different amplitude. For example, in a dense random actin network, diffusive-like trajectories are exhibited by myosin-driven cargoes as they walk from one filament to another [63]. In this case, the cargo motion is affected by the cytoskeleton process to which the cargo is attached, and other cell processes can also influence the fluctuations of the cytoskeleton itself [64]. Since the motion of the probe particle is not thermally driven, any analysis which assumes thermal motion will return inaccurate results. Moreover, these active diffusion phenomena are expected to increase with the probe particle size inside the biological cell and make it even complicated to determine the localized viscosity inside a cell at longer times scales [65, 66]. Therefore, using smaller sized probe particle is advantageous as it will create less hindrance in the intracellular transport mechanism.

Although both elastic and viscous properties can be extracted using the microrheology techniques, it is relatively straightforward to determine the viscosity. Recently, the viscosity of different concentrations of polyacrylamide solutions is measured by calibrating the trap stiffness using equipartition

theorem and then determining the autocorrelation function of the position of a particle [67]. For this purpose, a large sized 5 μm particle is employed as it's position can be measured without the need of achieving measurement bandwidth in the MHz regime. Although several microns sized particles lower the bandwidth requirement of the position sensitivity of the particle, it may not be suitable to use in biological materials having few micron-sized volumes such as red blood and sperm cells where smaller sized particles will be a better choice to be used as a probe. All the above techniques require calibrating the position of the particle from volts-to-meter which changes for slight changes in laser power, fluid localized concentration or viscosity and can be quite complicated for the fluids having time-invariant mechanical properties [68].

All the microrheology techniques measure the viscosity of the fluid at longer timescales typically in milliseconds where the particle is diffusing freely, and its motion is independent of the mass. However, at very short timescale typically in microseconds, the motion of the particle is dominated by its inertia and is not considered to be freely diffusing in the medium. This regime is called ballistic where the position of the particle is highly correlated and can be used to measure its instantaneous velocity which according to Einstein, is nearly impossible to measure. However, recent advances in the detection technologies for larger sized particle has made it possible to measure the instantaneous velocity [69–72].

Based on this principle, if faster measurements are made possible such that the motion of the particle can be measured in ballistic regime and at times scales shorter than the intracellular activities times, where particle is only thermally driven, then it is possible to use instantaneous velocity of the particle to measure the viscosity of intracellular fluids. This alternative and previously unexplored approach have the potential to extract the fluid viscosity at short time-scales, faster than the dynamic restructuring of biological cytoplasm, and without requiring a priori calibration of the position signal.

For this purpose, we have developed an ultra-fast particle position detection technique and tracked 1 μm particle with unprecedented measurement bandwidth as close as 10 MHz. As the particle displacement information is present in the light scattered by the particle, it is essential to be able to detect as much light to acquire short times scales position measurement. The detection scheme that we have developed can detect 160 mW of the scattered power using commercial optics and electronic detectors. This system has made it possible to track the ballistic motion of the particle and determine its instantaneous velocity in three different fluids using 1 μm silica particles. Chapter 4 of this dissertation explains the new detection technique to measure the ultra-fast measurement of the position of a particle.

Previously, the instantaneous velocity of an optically trapped particle is measured using high power threshold customized detectors and larger sized 3.06 μm silica and 5.36 μm $BaTiO_3$ particles [72]. In our OT setup while using only standard commercial equipment, we have measured instantaneous velocity of the smallest sized particle that has been ever measured in ballistic regime, i.e. using 1 μm silica particles which have $\sim$27 times lesser volume than previously used 3.06 μm particle, thus making is more susceptible to be used in biological cell. Additionally, in the ballistic regime, the velocity of a particle is correlated, and the velocity autocorrelation function is independent of units' conversion from volts to meter or trap stiffness calibration. Therefore, it can be computationally fitted to find the unknown viscosity of the fluid without knowing or calibrating the trap stiffness. Chapter 4 of this dissertation demonstrates the applicability of measuring instantaneous velocity of 1 μm particle to measure the viscosity of different fluids at short timescales.

1.4 Structured scattering for enhanced trapping of particles

In most of the optical tweezers, 1.064 μm wavelength is used to trap particles due to non-invasive nature for biological medium. Particle sizes comparable to the light wavelength are used in the experiments as trap stiffness is maximum for the particles comparable to the incident light wavelength. For a same optical system, particle and surrounding fluid properties, trapping efficiency scales inversely as the particle sizes increase [73, 74], making it difficult to trap the larger sized particle. Fundamentally, trap stiffness can be improved for larger sized particles by increasing the incident trapping beam power; however, it induces photodamage in the sample [75, 76] hence cannot be considered a reliable solution to increase trap stiffness.

There are many applications where several micrometer-sized particles carry vital importance and, non-invasive techniques to achieve higher trap stiffness and signal-to-noise ratio are required to understand and explore the fundamental science and biological phenomenon. For instance, light-driven micro-robots are being developed recently in which several micron-sized glass syringe is manipulated by trapping the spheroidal particles attached to the syringe, for targeted delivery of the drug. Similarly, micro gears and rods which act as either active or passive handles in making micro-robots, are usually manipulated using optical forces [77, 78]. Moreover, OT has been used to trap the red blood cells in vivo, to clear the blocked micro-vessels [79] and also for diseases identification [80, 81].

Similarly, biological cell sorting and manipulation are often done with OT where larger sized cell, typically greater than 10 μm, are displaced [82, 83]. In addition, triggering the vestibular behavior in zebrafish is done by applying optical trapping forces on 55 μm sized otoliths where very high

powers ranging from $50 \sim 600\ mW$ were illuminated on zebrafish [84]. Optical levitation of several micron-sized particles in a vacuum has also been used to better understand the particle physics and gravitational forces [17, 18, 85]. From these examples, it is clear that trapping of larger particles is very crucial in many biological and engineering applications and also for understanding a wider range of fundamental science, therefore, new tools to trap larger particles or enhance the trap stiffness are vital.

Trap stiffness depends upon several parameters such as optical scattering, extinction and absorption cross-section and, can be improved using several techniques either by structuring the incident beam profile or by altering the physical properties of the trapped particle. In principle, these techniques increase the light momentum transfer per photon to increase the resulting force due to the momentum transfer. Recently, a slight improvement in the optical trap stiffness has been demonstrated for counter-propagating trapping beams in which scattering forces is minimized resulting in the increased gradient force [86]. Additionally, several techniques based on the structured light fields have been demonstrated to improve the axial or lateral trap stiffness by 1.6 times than that for simple Gaussian trap [87–89].

The state-of-the-art in stiffness has been increased by a factor of 2 by employing specially engineered anti-reflection coated and high refractive index Titania particles to suppress the back-scattered light. Coating ensures stable trapping, while the high refractive index core allows powerful interaction with the trapping field. Using these particles in OT, back-scatter is suppressed, however, particles exhibit forward-scatter with a similar angular distribution to homogeneous spheres, but with far stronger scattered fields [90], resulting in the enhanced trapping. Engineering particle properties can enhance trap stiffness by two order of magnitude whereas; a significant improvement is expected to be achieved by structuring the incident light such that light-particle momentum transfer is maximized. Based on this, we have employed holographic optical tweezers and structured the illuminating light such that the particle scatters light at wider angles than the Gaussian beam scattering. This structured scattering not only enhances the trap stiffness by several orders of magnitude but also improves signal-to-noise ratio significantly. Chapter 5 of this dissertation explains the methodology and implementation of structuring the incident Gaussian beam to achieve higher trap stiffness for larger particles that can be very useful in several fundamental science and engineering applications.

1.5 Contents of this dissertation

Chapter 2 describes the fundamental Brownian motion theories for different sized particles trapped in fluids of different viscosity. Chapter 3 illustrates our efforts to design and construct the robust microscope and D-mirror based split detection scheme. Chapter 4 demonstrates the new flipped waveplate based high bandwidth particle tracking methodology to determine the instantaneous velocity of the Brownian particle in different fluids and extract the viscosity of surrounding fluid with the unprecedented fast rate. Finally, chapter 5 describes the concept and implementation of structured light in holographic optical tweezers to enhance the trap stiffness and signal-to-noise ratio by several orders of magnitude.

Chapter 2

Physics of optical tweezers

2.1 Overview

This chapter describes the theory of the optical forces applied by the incident laser beam on the particle to trap it. The first part of the chapter explains the optical forces on the dielectric particle for different regimes depending upon the particle size, i.e., ray optics, Rayleigh and Lorenz-Mie regime. The second part illustrates the theories of Brownian motion of a particle in a harmonic potential. This section includes the theoretical details of different regimes of Brownian motion of the particle from longer to shorter timescales and transition of different regimes of the Brownian motion depending upon trap stiffness, particle size and viscosity of the fluid.

2.2 Optical force on dielectric particle

The force acting on an optically trapped object is divided into two major components: the gradient (F_{gd}) and the scattering forces F_{st}. (F_{gd}) is directed to the gradient of the electromagnetic field and attracts the particle towards the highest intensity region which is the focal spot. F_{st} occurs as a result of the transfer of optical momentum produced by the incident photons scattering and applies force in the propagation direction of the incident beam. For a stable optical trap in three-dimensions, the gradient force must be larger than the scattering force.

The optical force exerted on the particle due to the incidence of classical light can be explained in two ways. On the one hand, it can be described as the transfer of momentum of incident photons per second $n_m P/c$ to the trapped object by the dimensionless factor generally represented as Q.

$$F = -\frac{Q n_m P}{c}, \tag{2.1}$$

where n_m is the refractive index of the medium, P is incident light power and c is the velocity of the

light. For a perfectly absorbing particle with plane wave approximation, $Q = 1$ which means that all the momentum of incident photons is transferred to the particle in the direction of the incident light propagation while $Q = 2$ for a perfectly reflecting particle. For particles smaller than the incident light wavelength, Q ranges from 0.03∼0.1 [91]. This formula describes how force is generated due to light-matter interaction. When optical force is exerted on the particle to trap it, this force can be approximated as a harmonic potential having trap stiffness κ which displaces the particle from the trap center by a distance x. This position dependent force can be can be written as

$$F = -\kappa x, \tag{2.2}$$

where the negative sign describes the direction of the applied optical force is always towards the equilibrium position.

2.2.1 Rayleigh Regime

For particles having sizes much smaller than the trapping beam wavelength, i.e., $r \ll \lambda$, the electromagnetic field is considered uniform across the trapped object and can be thought of as an induced point dipole. This regime is called the dipole or Rayleigh scattering regime. Then, the force $F_{gd,r}$ applied on the dipole by the electric field is given by [91, 92]

$$F_{gd,r} = \frac{1}{2}|\alpha_p|\nabla\langle E^2\rangle, \tag{2.3}$$

whereδE is the electromagnetic field and α_p is polarizability of particle that satisfies the Clausius−Mossotti equation [93]

$$\alpha_p = r^3\left\{\frac{\varepsilon - 1}{\varepsilon - 2}\right\}, \tag{2.4}$$

where r is the particle radius and ε is the dielectric permittivity. On the other hand, the scattering and absorbing forces can be described using absorbing and scattering cross-section of small particles as follows:-

$$F = \frac{|E|^2}{8\pi}(\alpha_{abs} + \alpha_{scat})\mathbf{k}/|\mathbf{k}|, \tag{2.5}$$

where α_{abs} and α_{scat} are the absorbing and scattering cross-section of the particle respectively and, $\mathbf{k}$

denotes the light vector. A computational toolbox to calculate forces in Rayleigh regime can be found in ref. [94].

2.2.2 Ray optics regime

When the trapped particle is much larger than the trapping wavelength $(r \gg \lambda)$, the interaction of light with the particle can be described by the ray optics method. In this analysis, the incident light field is considered as a ray of light having zero wavelength which can change its direction when reflected or refracted through a medium of the uniform refractive index. On changing its direction, the change in the momentum occurs which results in optical forces on the dielectric particle and these forces on the spherical particle can be calculated using Fresnel formulas [95].

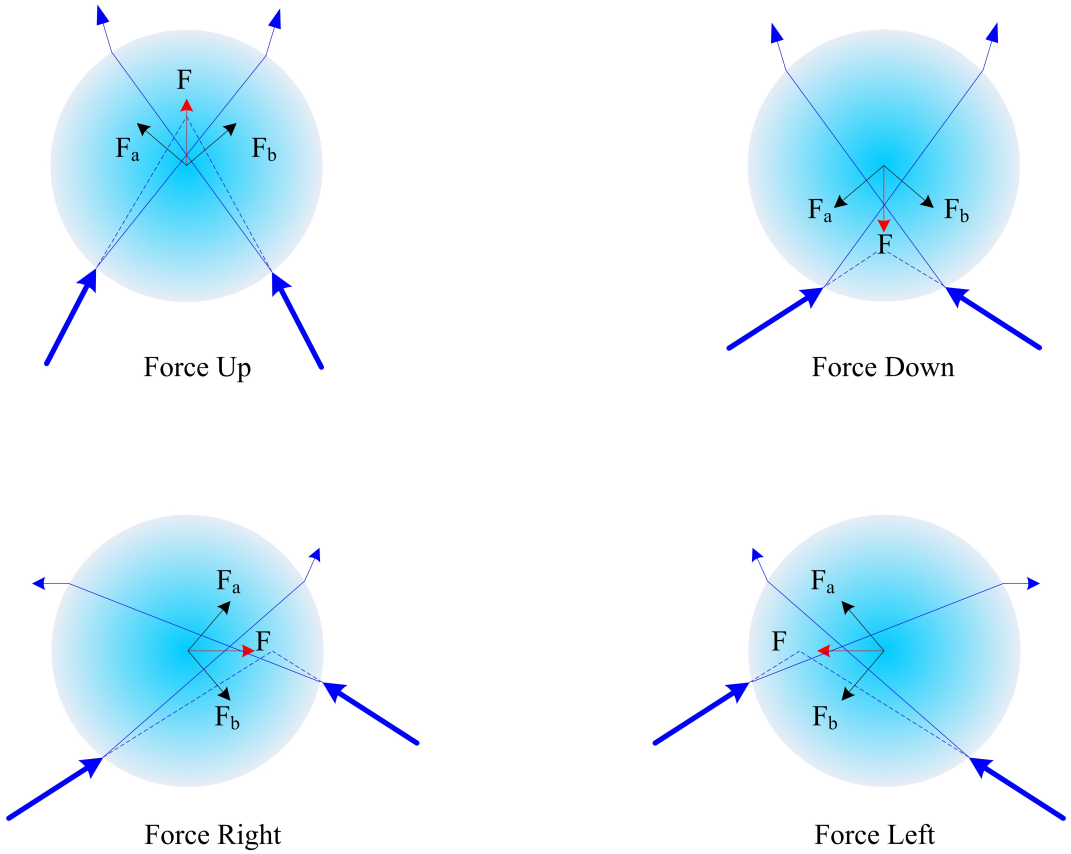

Figure 2.1: **Schematic of optical forces on the particle in ray optics regime.** It shows the ray optics diagrams of four different cases when light is impinged on the particle at four different incidence angles having force components F_a and F_b which results in a net force F on the particle in different directions and displaces it accordingly.

Hence, gradient $F_{gd,ro}$, and scattering forces $F_{st,ro}$ in the ray optics regime are given by

$$F_{gd,ro} = \frac{n_m P}{c}\left\{R\sin 2\theta_i - \frac{T^2[\sin(2\theta_i - 2\theta_r) + R\sin 2\theta_i]}{1 + R^2 + 2R\cos 2\theta_r}\right\} \tag{2.6}$$

$$F_{st,ro} = \frac{n_m P}{c}\left\{1 + R\cos 2\theta_i - \frac{T^2[\cos(2\theta_i - 2\theta_r) + R\cos 2\theta_i]}{1 + R^2 + 2R\cos 2\theta_r}\right\} \tag{2.7}$$

where θ_i and θ_r are the angles of incidence and refraction respectively. As it is evident from the formulas, both gradient and scattering forces are dependent on transparency T and reflection coefficient R of the particle, and on θ_i and θ_r. A computational toolbox to calculate the optical force in the ray optics regime is available at the ref. [74]. A schematic diagram of applied forces based on the ray tracing method is shown in figure 2.1. It shows that the applied force on the particle is different for different angles of incidence and refraction.

2.2.3 Lorenz-Mie Regime

The particle in both Rayleigh and ray optics regime has several fundamental science and sensing applications. However, in biology, particle comparable to the wavelength of trapping beam is mostly employed as the trapping force per mW of optical power is larger when these parameters are close to each other. For the particles, between Rayleigh and Mie scattering region, the applied optical forces are described by classical electrodynamics. The time-averaged net radiation pressure force F_{rp} on the object can be calculated by taking integral of the dot product of the unit vector pointing in the normal direction $\hat{n}$ and Maxwell's stress tensor, for an enclosed surface s $\overrightarrow{T}$ [96–98].

$$F_{rp} = \langle \oint_s \hat{n}\overrightarrow{T}\, ds \rangle \tag{2.8}$$

The computational toolbox to calculate forces in Lorenz–Mie Regime can be found in ref. [99]. It can be used to investigate the forces in OT as functions of several parameters such as r, λ, n_m and NA. The corresponding values of these parameters can be chosen, and resulting forces can be calculated for a given system.

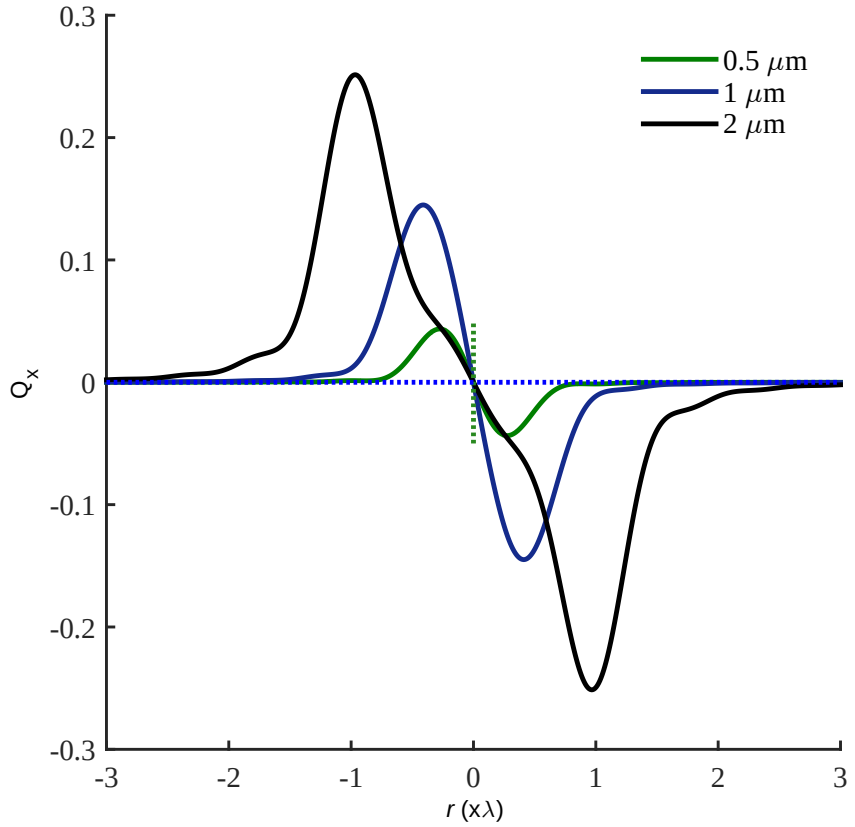

Figure 2.2: **Lateral trapping efficiency of different sized particles in Lorenz-Mie regime.** Q_x is a dimensionless normalized force factor in the lateral direction and r is the particle radius in the units of incident light wavelength. The slope of the graph near the central axis shows the trap stiffness which is larger for 1 μm silica particle when trapped in water n=1.33 using 1064 nm laser and 1.3 NA objective.

Figure 2.2 shows the lateral trapping efficiency of different sized optically trapped silica particles when trapped using circularly polarised 1064 nm laser beam. The slope of the graph near the center exhibits the trap stiffness which larger for particles closer to the trapping beam wavelength $(1\mu m)$. The peaks show the maximum force which is experienced by the particle when its displacement from the optical axis is close to the radius of the particle. At distances larger than r, trap efficiency starts decreasing until scattering forces are dominant and the particle is no longer trapped in the harmonic potential of the laser beam.

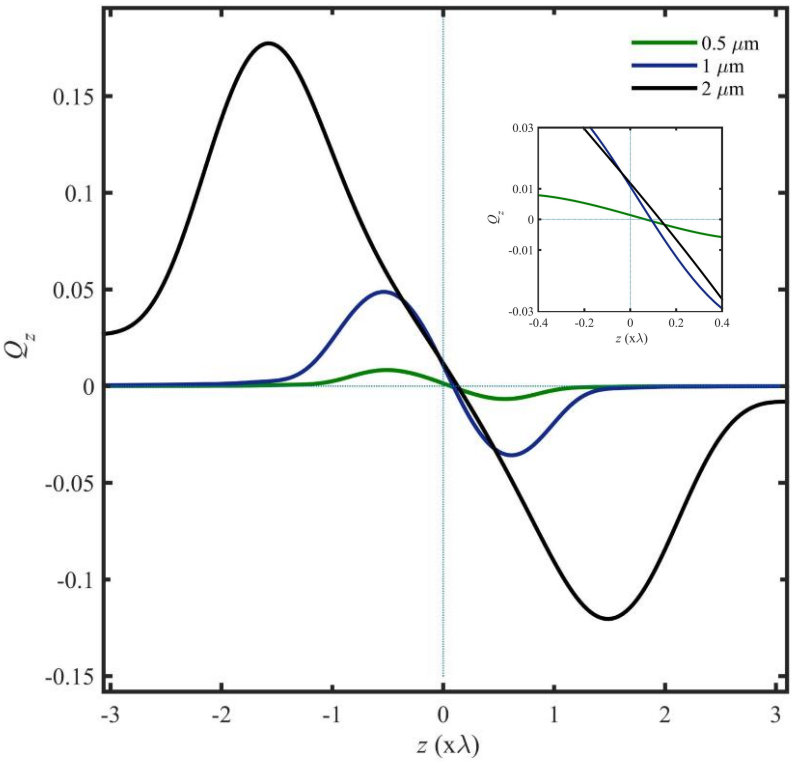

Figure 2.3: **Axial trapping efficiency of different sized silica particles.** Q_z is a dimensionless normalized force factor in the axial direction and r is the particle radius in the units of incident light wavelength. The slope of the graph near the central region describes the axial trap stiffness. It is higher for particle sizes closer to the trapping beam wavelength. Due to the scattering forces in the axial direction, the particle is in equilibrium at a position slightly away from the optical axis.

Similarly, figure 2.3 shows the axial trapping efficiency of different sized optically trapped silica particles when trapped using circularly polarised 1064 nm laser beam. Trap stiffness is larger for particles closer to the trapping beam wavelength $(1\mu m)$. The particle is trapped slightly away from the trap center due to scattering forces, and therefore, maximum axial trap efficiency and stiffness are slightly smaller than lateral. However, a trapping region of displacement of a particle from the center of the trap is slightly larger in the axial direction than lateral.

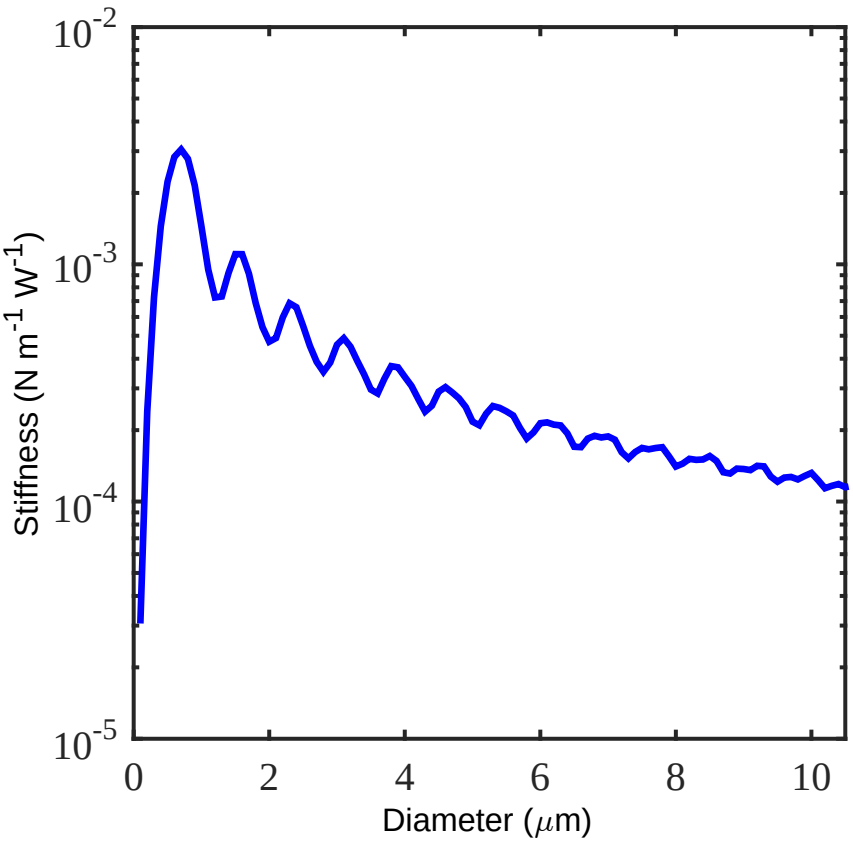

Figure 2.4: **Lateral trap stiffness for different sized silica particles calculated using Lorenz-Mie Theory.** Trap stiffness is maximum for 0.7 *um* diameter particle when trapped using 1064 nm laser and 1.3 NA objective, in water of refractive index=1.33.

Based on the axial and lateral trap efficiencies, most of the optical tweezers based probe experiments utilize lateral forces especially for biology as it governs higher force per mW than axial forces. Figure 2.4 shows the lateral trap stiffness calculated for different sized silica particle, trapped in water using 1064 nm laser. The stiffness is calculated using OT computational toolbox.

2.3 Optical trapping in liquid

Optical forces on the micro/nano-particles can be described based on the models mentioned above. In most of the applications, particles are dispersed and trapped in a liquid, though there are studies of trapping in a gas [69] and vacuum [14, 100] as well. For stable trapping in the fluid, main condition of the trapping is that refractive index of the particle should be higher than that for surrounding fluid. When a particle is dispersed in a fluid, it undergoes the Brownian motion which can be measured using OT. Following paragraphs describe the theories of Brownian motion and how it can be measured and

analysed.

2.3.1 Free Brownian Motion

The Brownian motion of a particle in a fluid is the random motion of the particles as a result of trillions of collisions of the fluid molecules. This motion was first discovered by Robert Brown in 1827 who observed the random motion of the micron-sized particles under the microscope [101]. Later on, in 1905, Einstein described the Brownian motion as the amplification of the statistical fluctuations of the surrounding fluid molecules. He postulated that the average position fluctuation of the Brownian particle is equal to 0 while the average distance explored by the particle, generally called Mean Squared Displacement (MSD), increases with time depending upon the diffusivity of a particle in the medium.

$$MSD_E = \langle (\Delta x(t))^2 \rangle = 2Dt \tag{2.9}$$

where D is the diffusion constant given by:

$$D = \frac{k_B T}{\gamma}, \tag{2.10}$$

where T is the temperature, k_B is the Boltzmann constant and γ is the Stokes' damping coefficient. At such timescales the Stokes' damping coefficient is given by:

$$\gamma = 6\pi\eta r, \tag{2.11}$$

where r is the radius of the particle and η is the viscosity of the fluid. Einstein proposed that it will not be possible to determine the instantaneous velocity of a Brownian particle due to its very rapidly changing and randomized motion due to the kicks from the surrounding molecules. As such, displacement of the particle due to the random kick from fluid molecules is considered as a motion which is differentiable anywhere [102]. Therefore, the instantaneous velocity of a Brownian particle is undefined; however, in time interval t, the root-mean-square velocity is given by [103, 104]

$$v_{rms} = \sqrt{\langle (\Delta x(t))^2 \rangle}/t = \sqrt{2D/t}. \tag{2.12}$$

This result is valid only at long timescales, where statistical approach can be used, and particle momentum can be averaged to zero. At long timescales when $t \gg \tau_p$, the particle motion lies in the

diffusive regime where $\tau_p = m_p/\gamma$ is known as the momentum relaxation time of the Brownian particle having mass m_p. At very short timescales ($t \ll \tau_p$), the dynamics of a particle is dominated by its inertia, the motion is the ballistic and instantaneous velocity of the particle can be measured simply as $v_i = \Delta x(t)/t$. In this regime, MSD of the particle is dependent upon the mass, and it maintains in velocity for a certain time. In contrast to the free diffusive regime, MSD of the particle scales as the square of the time. Hence, it is given by the following expression

$$MSD_E^b = \frac{k_B T}{m_p} t^2. \tag{2.13}$$

In 1908, Paul Langevin deduced a stochastic force and derived Einstein's mean squared displacement expression from Newton's second law. Langevin's approach is more intuitive than Einstein's, and the "Langevin equation" has been used widely in stochastic physics [105]. He described the motion of a Brownian particle having mass m_p as a function of time.

$$m_p \ddot{x}(t) = -\gamma \dot{x}(t) + F_{th}(t).. \tag{2.14}$$

Taking the Fourier transform and solving for the displacement in the frequency domain, it is given by

$$x(\omega) = \frac{(2k_B T\gamma)^{1/2}}{-m_p\omega^2 + i\omega\gamma}. \tag{2.15}$$

Now the power spectrum of the motion of a particle P_x which describes how much amplitude of displacement is present at specific frequency ω is given by

$$P_x = \langle |x(\omega)|^2 \rangle = \frac{2\gamma k_B T}{\omega^2\gamma^2 + m_p^2\omega^4}. \tag{2.16}$$

As the MSD of the particle is correlated in the ballistic regime and can govern its velocity, the amplitude of velocity at given frequencies can be seen on the velocity power spectrum P_v, obtained by multiplying position spectrum to ω^2.

$$P_v = \omega^2 P_x = \frac{2\gamma k_B T}{\gamma^2 + m_p^2\omega^2}. \tag{2.17}$$

Moreover, time domain expression of the velocity of a particle is given by

$$v(t) = v_o e^{-t/\tau_p} + \frac{e^{-t/\tau_p}}{m_p} \int_0^t e^{t'/\tau_p} F_{th}(t') dt'. \tag{2.18}$$

As in ballistic regime, the velocity of a particle is correlated, it can be described in terms of its autocorrelation function which provides a measure of the time it takes for the particle to "forget" its initial velocity. When the particle motion is diffusive, the velocity correlation is zero while in the transition from diffusive to ballistic; it increases exponentially. In the ballistic regime, the velocity correlation is very high and has a finite value. The velocity autocorrelation is given by:-

$$C_v(t) = \int_0^\infty \bar{v}(t'+t)\bar{v}(t') \tag{2.19}$$

where the bar represents a time average. Mathematically, it is calculated by taking the Fourier transform of the velocity power spectrum.

$$C_v(t) = \frac{k_B T}{m_p} e^{-t/\tau_p}, \tag{2.20}$$

where τ_p is the momentum relaxation time τ_p which defines the timescales at momentum of the particle is relaxed and can be considered zero. At timescales shorter than τ_p, particle maintains its momentum and can be considered as a boundary of transition of free diffusion to the ballistic regime or vice versa. Time-dependent position fluctuation of the particle can be calculated by integrating the velocity of the particle.

$$x(t) = x_0 + \int_0^t v(t') dt' \tag{2.21}$$

Now MSD is given by

$$MSD_L = \frac{2k_B T \tau_p^2}{m_p} \left\{ \frac{t}{\tau_p} - (1 - e^{t/\tau_p}) \right\}. \tag{2.22}$$

All the equations mentioned above are for free Brownian motion when no external force is influencing it. In OT, the motion of the particle can be very well analyzed using the velocity autocorrelation function and power spectrum, therefore, we are including their analytical expression to describe the Brownian motion theory and will compare our results in following chapters based on these analytical expressions.

2.3.2 Brownian motion in an optical trap

When a Brownian particle is trapped in an OT, its motion is in a dynamic equilibrium where the thermal noise from the surrounding molecules tries to push it out of the trap, but optical forces drive it towards the center of the trap. The timescale τ_k at which the restoring force of the optical trap acts on the particle is given by the ratio of Stokes drag coefficient γ and trap stiffness κ i.e $\tau_k = \gamma/\kappa$. Normally, τ_k is significantly larger than the momentum relaxation time τ_p for particle size of few microns trapped with few hundreds of mW optical power.

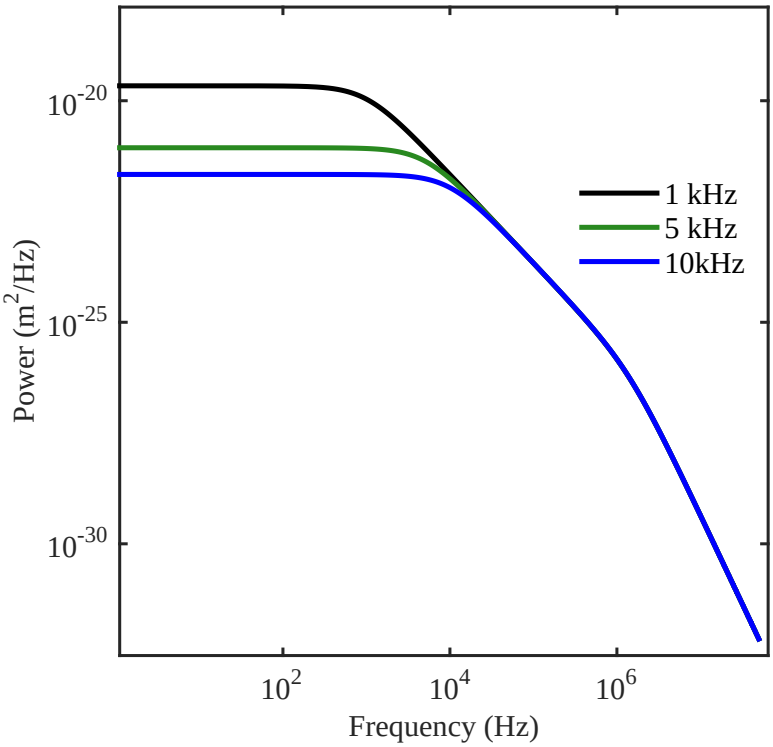

Figure 2.5: **Power spectrum of an optically trapped 1 μm particle at different trapping stiffness.** Optical trap confines the motion of the particle at lower frequencies however, it undergoes free Brownian motion at higher frequencies larger than f_c

The Langevin equation of the Brownian particle in an optical trap is given by

$$m_p\ddot{x}(t) = -\gamma\dot{x}(t) - \kappa x(t) + F_{th}(t), \tag{2.23}$$

$$x(\omega)^{\kappa} = \frac{(2k_BT\gamma)^{1/2}}{-m_p\omega^2 + i\omega\gamma + \kappa}, \tag{2.24}$$

$$P_x^{\kappa} = \frac{2\gamma k_B T}{\omega^2\gamma^2 + m_p^2(\omega_0^2 - \omega^2)^2}, \tag{2.25}$$

where $\omega_0 = \sqrt{\kappa/m_p}$ is the trap resonant frequency. Figure 2.5 shows power spectrum of optically trapped 1 μm particle at different trapping strengths. Optical trap confines the motion of the particle depending upon corner frequency $f_c = \kappa/2\pi\gamma$ and particle cannot undergo free Brownian motion until it is free from the effect of the optical trap.

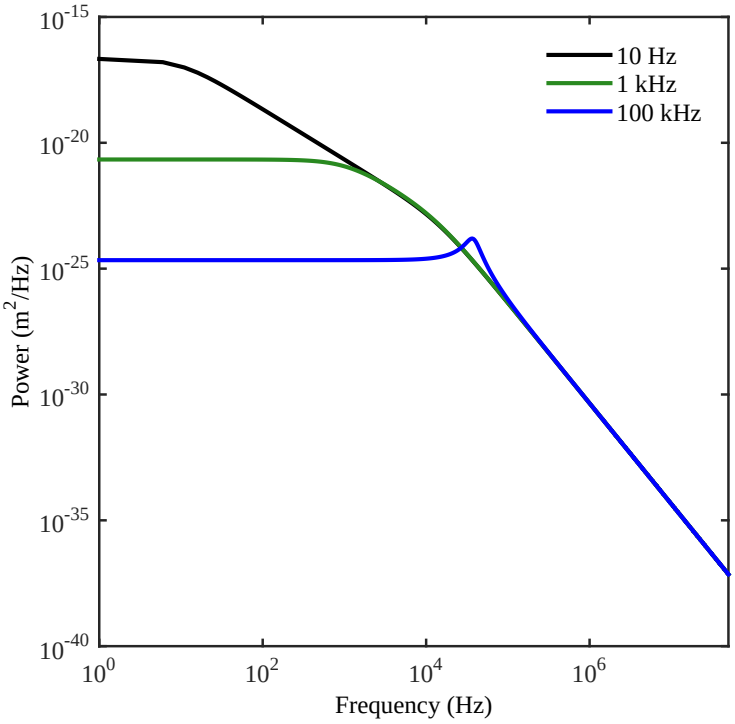

Figure 2.6: **Power spectrum of an optically trapped 10 μm particle at different trapping strengths.** At lower frequencies shown in black and green color, particle has overdamped harmonic motion. However, if trap corner is higher, particle undergoes underdamped harmonic motion and a resonant peak appears at the resonance frequency.

In Eq. 2.25, when $\omega_0 < 1/2\tau_p$, the harmonic potential effects the motion of the particle only in the diffusive region and behaves like an overdamped system. When $\omega_0 > 1/2\tau_p$, the optical trap will force the particle to oscillate until the damping from the fluid make the motion damped out. In this case, the motion of the particle will be underdamped, and this effect will appear as a resonant peak in the power spectrum nearω_0 which will be stronger for lower damping. This resonance effect is shown in Figure 2.6

In most the optical trapping experiments, the trap corner frequency is lower than the resonant frequency, and particle has overdamped harmonic motion as shown in the figure 2.5. For this case, the velocity power spectrum P_v^{κ} is given by

$$P_v^{\kappa} = \frac{2\omega^2 \gamma k_B T}{\omega^2 \gamma^2 + m_p^2(\omega_0^2 - \omega^2)^2}. \tag{2.26}$$

And normalized autocorrelation function $C_v^{\kappa}(t)$ is

$$C_v^{\kappa}(t) = \frac{\langle v(t)v(0)\rangle}{\langle v^2\rangle} = \frac{1}{2|\omega_c|\tau'_+} e^{-t/\tau'_+} - \frac{1}{2|\omega_c|\tau'_-} e^{-t/\tau'_-}, \tag{2.27}$$

where

$$\tau'_{\pm} = \frac{2\tau_p}{1 \pm 2\tau_p|\omega_c|}, \tag{2.28}$$

where $\omega_c = \sqrt{\omega_0^2 - (2\tau_p)^{-2}}$ is the trap corner frequency. Normalizing the autocorrelation function by $C_v(0) = \langle v^2\rangle = k_B T/m_p$ makes the correlation function independent of the volts-to-meter conversion factor and scales between zero to one. Therefore, time is the only independent variable which can be measured accurately with the detection system. As the velocity autocorrelation function describes the time-dependence of velocity fluctuation of the Brownian particle, it makes it much easier to see whether temporal and spatial resolution of the measurement system is enough to measure the velocity of the Brownian particle.

At shorter times scales where the motion of the particle is ballistic, its velocity has high correlation and can be seen in the velocity correlation graph in figure 2.7. The particle has a higher correlation at timescales shorter than 0.1 μs and this correlation decays at longer timescale until it reaches zero. To measure instantaneous velocity of 1 μm particle with high correlation, the temporal resolution of the OT measurement system must be larger than 0.1 μs, though it can be measured with even higher correlation if higher measurement bandwidth can be achieved. For $\tau_k \ll \tau_p$, velocity of the particle is not influenced by the optical trap. Similarly, MSD of the particle incorporating the trap dynamics is described as

$$MSD_L^{\kappa}(t) = \frac{2k_B T}{m_p \omega_0^2}[1 - \frac{1}{2|\omega_c|\tau'_+} e^{-t/\tau'_-} + \frac{1}{2|\omega_c|\tau'_-} e^{-t/\tau'_+}]. \tag{2.29}$$

As shown in the figure 2.8, the motion of the particle is confined by the optical trap at longer

timescales. Higher the trap stiffness, longer the time the particle remains in a harmonic potential. At shorter timescales when it is no longer under the effect of the trap, particle undergoes free Brownian and ballistic motion depending upon τ_p.

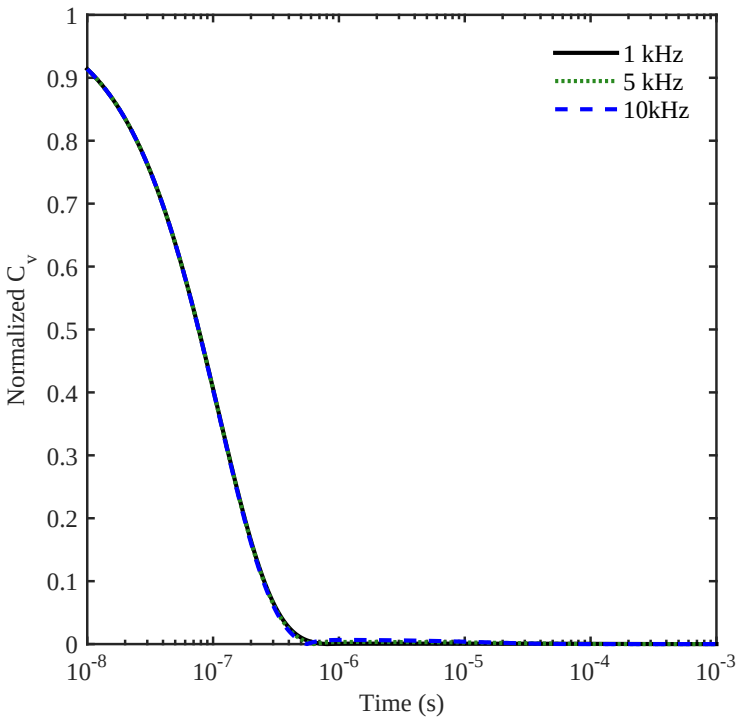

Figure 2.7: **Normalized velocity autocorrelation of an optically trapped 1 μm particle at different trapping stiffness.** This graph shows that for most of the optical tweezers which utilize 1 μm silica/polystyrene particles at $<$10 kHz corner frequency, the velocity auto-correlation function of the particle is unchanged and not influenced by the trap if $\tau_k >> \tau_p$.

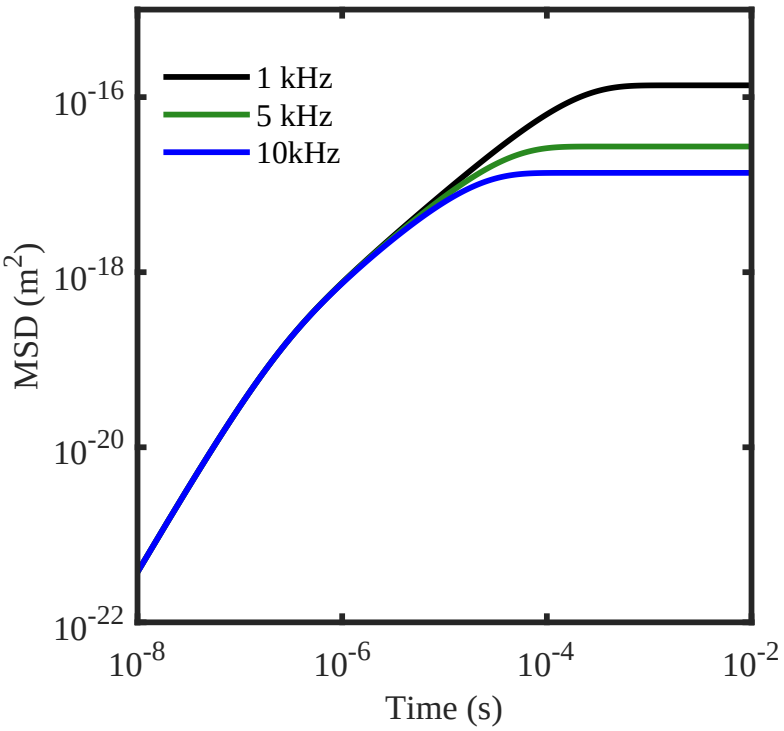

Figure 2.8: **Double logarithmic plot of means square displacement of an optically trapped 1 μm particle at different trapping stiffness.** This shows that the particle undergoes Brownian motion for a longer time for a weak trap, while for a strong trap, its motion is confined by the trap at relatively shorter timescales depending upon trap stiffness.

2.3.3 Brownian motion with memory

Brownian motion of a particle in a gas is a random collision of gas molecules with the particle in a reversible manner where particle experiences random collisions of gas molecules and do not have any back-action effect on the gas. However, in case of liquid, the inertia of the surrounding liquid is as much significant as the particle because of the relatively higher density due to which the particle experiences more collision from surrounding molecules at a similar temperature. There are some specific timescales associated which help to understand the different regions of the Brownian motion better.

The full Brownian motion of a particle over different timescales is described in figure 2.9. The motion is free diffusive and ballistic respectively, at timescales much larger and shorter than τ_p. At longer times scales, MSD is proportional to t, the motion of the particle is random and, independent of both mass of the particle and surrounding fluid displaced by the Brownian particle. This regime is called

free diffusive. After this region, the motion of the particle is in between t and t^2 of the proportionality, called the transition/intermediate regime. In the transition regime, the surrounding fluid dragged by the particle retains the fluid vorticity created due to the particle motion due to which particle motion is influenced by this displaced mass which appears as an added mass to the particle mass. This total displaced mass is called the effective mass m_e and is equal to the sum of the mass of the particle and half the mass of the surrounding fluid [106, 107].

$$m_e = m_p + \frac{1}{2}m_f, \tag{2.30}$$

where $m_p = (4/3)\pi r^3 \rho_p$ is the mass of the Brownian particle and $m_f = 4/3\pi r^3 \rho_f$ is the mass of fluid and m_e is the effective mass. This equation does not depend upon the shape of the particle; rather the displaced mass is the important factor. In this case, particle mass in the Equipartition theorem will be replaced by the effective mass.

$$\frac{1}{2}m_e\langle v^2\rangle = \frac{1}{2}k_B T, \tag{2.31}$$

and effective root-mean square velocity of the Brownian particle v^e_{rms}will be

$$v^e_{rms} = \sqrt{\frac{k_B T}{m_e}}. \tag{2.32}$$

The fluid mass displaced by the particle has the exciting feature of the particle position memory. For example, if the moving Brownian particle is suddenly stopped, the fluid flow vortices caused by the previous motion of the particle will drag the particle to keep it moving along the fluid. Thus the presence of dense fluid displaced by the particle or the fluid vortices, create a memory effect on the motion of the particle. Therefore, future particle positions are not completely random but dependent upon the history of its position due to fluid vorticity. This phenomenon was first observed in 1945 and termed as hydrodynamics memory effect which is significantly dominant on the Brownian motion at short times scales. The fluid vorticity interacts with particle for a certain amount of time and the time over which fluid vorticity propagates a distance equal to the size of the particle is generally called characteristic fluid-particle interaction decay time τ_f. For the particle and fluid density denoted by ρ_p and ρ_f respectively, $\tau_f = 9\tau_p\rho_f/2\rho_p$. These hydrodynamic memory effects are presents for the timescales shorter than τ_f.

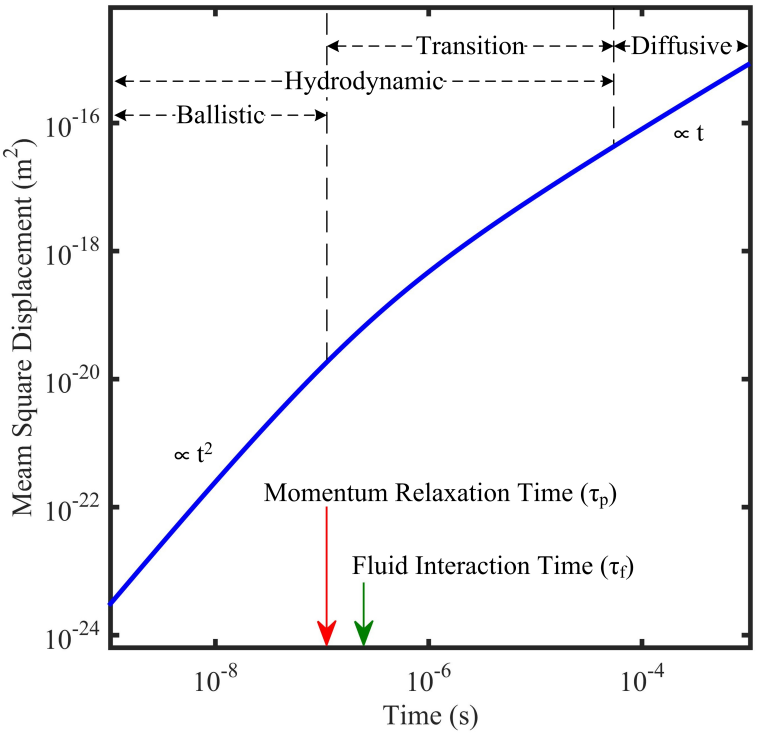

Figure 2.9: **Brownian motion from long to shorter timescales.** At longer timescales, the motion of the particle is free diffusive and ballistic at very short timescales. In the transition from diffusive to ballistic, particle motion is affected by hydrodynamics and particle starts to drag some fraction of the surrounding fluid for all shorter timescales.

At timescales shorter than τ_p, the motion of the particle is not random and it depends upon the effective mass of the particle. For timescales shorter than τ_f, the position of the particle is highly correlated and can be used to determine the velocity of the particle in the fluid. In the case of 1 μm particle in water, hydrodynamic memory effects extend the time for the particle to become ballistic where MSD of the particle is proportional to t^2. Particle motion is purely ballistic when its velocity correlation reaches the plateau. In the complete MSD graph, fluid mass is added into the particle mass for all the timescales shorter than τ_f. However, if the fluid is considered compressible then at timescales $\tau_c = d/c_s$, where d and c_s are particle diameter and speed of sound in the fluid, the particle motion is decoupled from the surrounding fluid. In this situation, fluid is compressed rather than dragging with the particle; therefore, the particle will move with its own mass m_p rather than effective mass m_e.

Presence of the fluid vortices or hydrodynamic memory effects creates damping force on the particle and can be included in to the generalize Langevin equation for the complete description as follows:-

$$m_e\ddot{x}(t) = -\gamma\dot{x}(t) - 6r^2\sqrt{\pi\rho_f\eta}\int_{-\infty}^{t}(t-t')^{-1/2}\ddot{x}(t')dt' - \kappa x(t) + F_{th}(t). \tag{2.33}$$

Eq. 2.33 describes the complete Brownian motion theory in an optical trap which also includes hydrodynamic memory effects. The term on the left-hand side is the accelerating force of the particle. Terms on the right-hand side: the first term describes the Stokes' friction force, the second term illustrates the hydrodynamic memory effect of the fluid, the third term depicts the harmonic trap force, and the last term is the Brownian stochastic force. Detailed description and calculation of hydrodynamic memory term can be found in references [70, 108, 109].

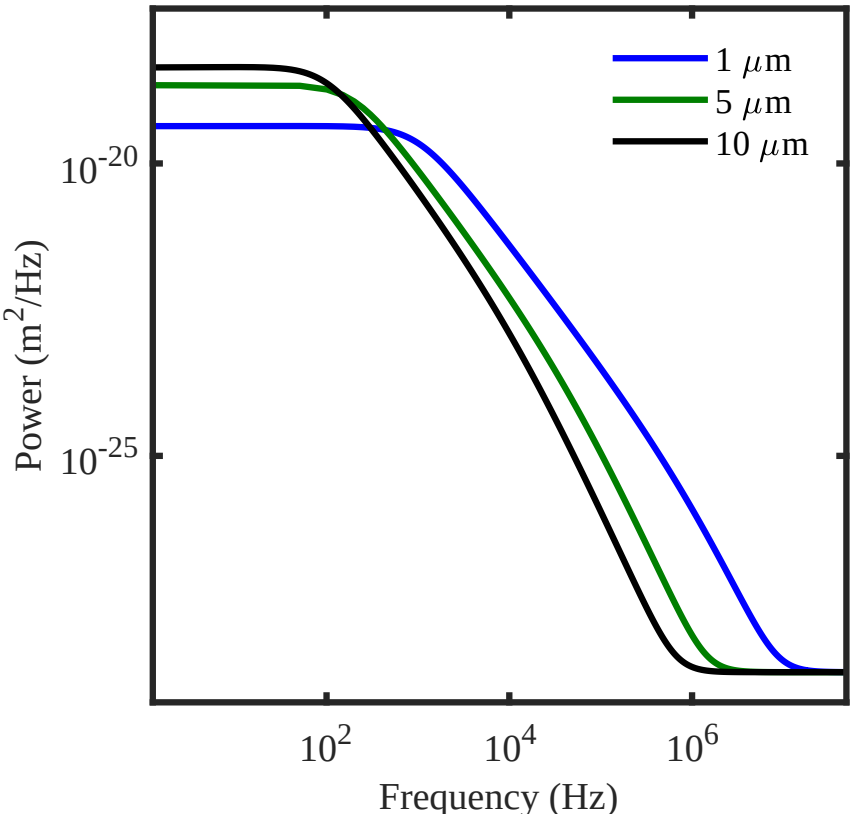

Figure 2.10: **Hydrodynamic power spectrum for different sized particles trapped in water for equal trap stiffness.** Smaller particle sizes have higher amplitude of the displacement while larger sized particles undergo shorter distances for same trap stiffness. Ballistic motion for the 10 μm particle starts earlier than that for 1 and 5 μm. The spectrum becomes flat at higher frequency due to shot noise.

An analytical expression of the power spectrum of optically trapped particles undergoing the hydrodynamics effects is given by [54, 110].

$$(P_x^k(f))_h = \frac{D}{\pi^2 f^2} \frac{1+\sqrt{f/2\phi_f}}{[\phi_k/f - \sqrt{f/2\phi_f} - f/\phi_p - f/9\phi_f]^2 + [1+\sqrt{f/2\phi_f}]^2}, \tag{2.34}$$

where $\phi_{k,p,f} = 1/(2\pi\tau_{k,p,f})$. For simple Brownian motion case neglecting the hydrodynamic effects, power spectrum of the particle rolls of $1/f^2$ in diffusive and $1/f^4$ in ballistic regime. When hydrodynamic effects and included it takes rather a complicated form and particle undergoes $1/f^2$ in diffusive and $1/f^{3.5}$ in ballistic regime. Figure 2.10 shows power spectrum of optically trapped particle where its motion includes the hydrodynamic effects.

Another important parameter which influences the Brownian motion is the viscosity of the fluid. Figure 2.11 shows power spectrum of an optically trapped 1 μm particle for fluids of different viscosity but same density. After the trapping region, particle undergoes Brownian motion which rolls off as $1/f^2$ until $\tau \to \tau_f$ and then the transition region scales differently for different viscosity until ballistic motion is reached where it scales as $1/f^{3.5}$ for all different viscosity.

Now expression for the power spectrum and velocity autocorrelation function is as simple in the hydrodynamic case as described by Eq. 2.25 and 2.29 rather they take complicated form first calculated by Hinch for free particles from the original Langevin analysis [108] and then by Clercx and Schram for a Brownian particle in a harmonic potential [109]. These expressions can adequately describe the Brownian motion of an optically trapped microparticle in a fluid [71, 111, 112].

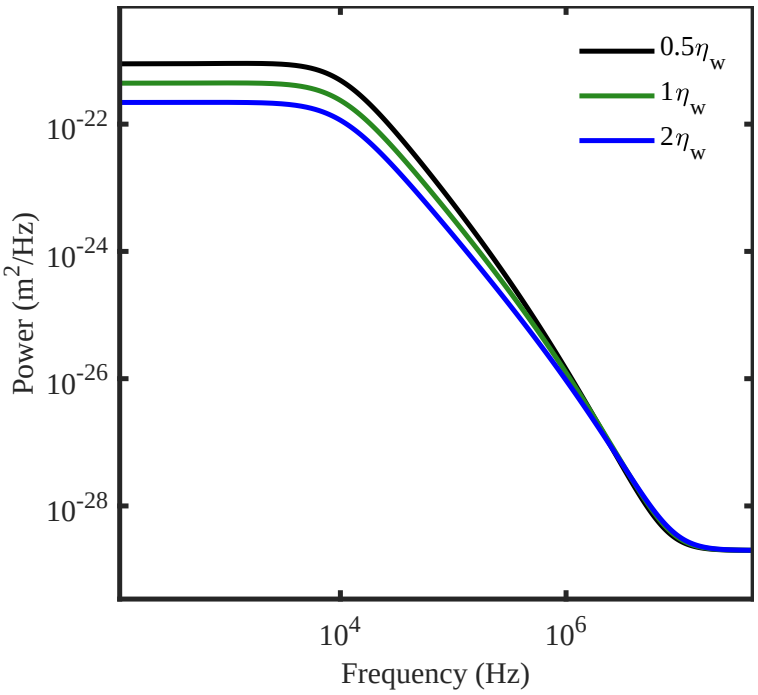

Figure 2.11: **Hydrodynamic power spectrum for different viscosity fluids as compared to water.** Particle motion scales identically both at short and longer timescales, but scales different in the intermediate region due to hydrodynamic effects.

Normalized hydrodynamic VACF is given by:-

$$(C_v^{\kappa}(t))_h = \frac{v(t)v(0)\rangle}{k_B T/m_e} = \frac{c_1^3 e^{c_1^2 t}\mathrm{erfc}(c_1\sqrt{t})}{c_1(c_1-c_2)(c_1-c_3)(c_1-c_4)} + \frac{c_2^3 e^{c_2^2 t}\mathrm{erfc}(c_2\sqrt{t})}{c_2(c_2-c_1)(c_2-c_3)(c_2-c_4)} + \frac{c_3^3 e^{c_3^2 t}\mathrm{erfc}(c_3\sqrt{t})}{c_3(c_3-c_1)(c_3-c_2)(c_3-c_4)} + \frac{c_4^3 e^{c_4^2 t}\mathrm{erfc}(c_4\sqrt{t})}{c_4(c_4-c_1)(c_4-c_2)(c_4-c_3)}, \tag{2.35}$$

where c_1, c_2, c_3 and c_4 are the four roots of the equation.

$$(\tau_p + \frac{1}{9}\tau_f)c^4 - \sqrt{\tau_f}c^3 + c^2 + \frac{1}{\tau_k} = 0 \tag{2.36}$$

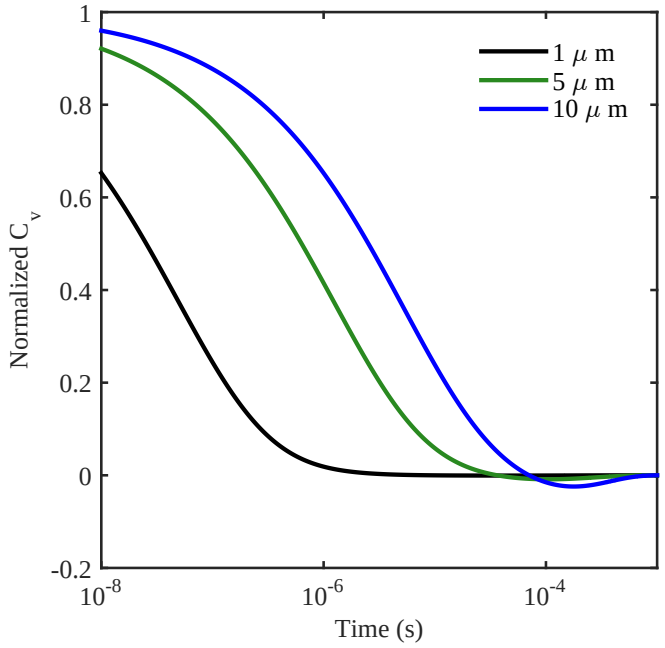

Figure 2.12: **Hydrodynamic normalized velocity autocorrelation for different sized particles trapped at** $fc = 10kHz$**.** Larger size has a relatively higher correlation in velocity than for smaller, at a given time. The velocity correlation decay rate is also slower for larger sized particle than for smaller.

Moreover, the mean square displacement of a trapped microparticle including hydrodynamic effects

in a liquid is given by

$$MSD_h^{\kappa}(t) = \frac{2k_BT}{\kappa} + \frac{2k_BT}{m_e}\frac{e^{c_1^2 t}\mathrm{erfc}(c_1\sqrt{t})}{c_1(c_1-c_2)(c_1-c_3)(c_1-c_4)} + \frac{e^{c_2^2 t}\mathrm{erfc}(c_2\sqrt{t})}{c_2(c_2-c_1)(c_2-c_3)(c_2-c_4)} + \frac{e^{c_3^2 t}\mathrm{erfc}(c_3\sqrt{t})}{c_3(c_3-c_1)(c_3-c_2)(c_3-c_4)} + \frac{e^{c_4^2 t}\mathrm{erfc}(c_4\sqrt{t})}{c_4(c_4-c_1)(c_4-c_2)(c_4-c_3)}, \tag{2.37}$$

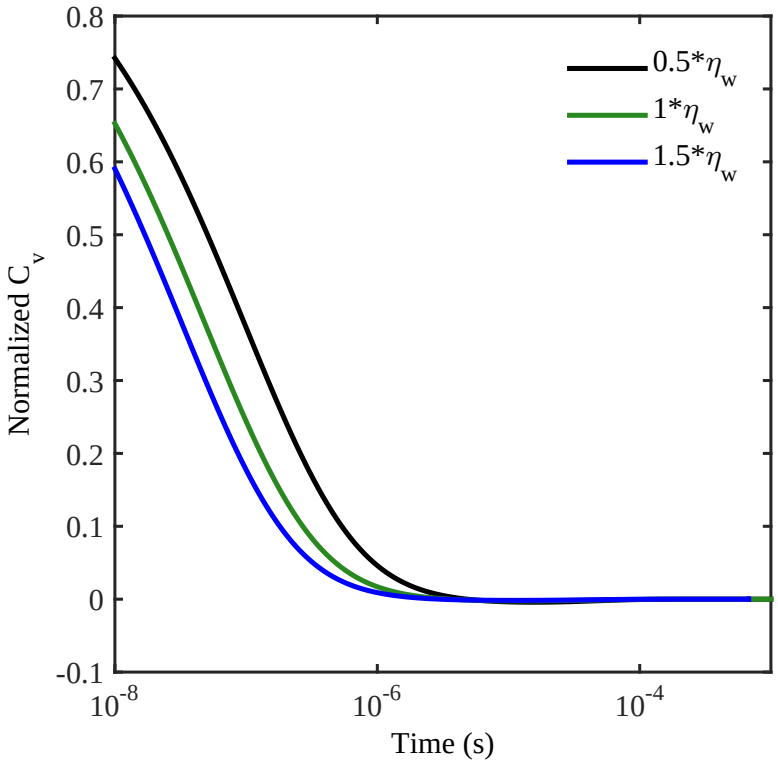

Figure 2.13: **Hydrodynamic normalized velocity autocorrelation for $1\mu m$ particle trapped in different viscosity fluids relative to water, at $f_c = 10kHz$.** The decay rate is faster for fluid having viscosity double than for water and smaller for the fluid with lower viscosity.

Figure 2.12 shows velocity autocorrelation with respect to lag time for different particle sizes. The correlation is very high at the short time and decays at longer time scales until it becomes flat. This decay rate is steeper for smaller particles and slower for a larger particle which means that the velocity of the smaller sized particle is lost quickly as compared to the larger sized particle. The thermal velocity of the particle is $v_{rms} = \sqrt{kbT/m_e}$ which means that larger particles have lower thermal velocity.

The required position resolution with 10% uncertainty is $\Delta x = \tau_{p,e} v_{rms}/100$. Increasing the particle size for the same material increases the product of $\tau_{p,e} v_{rms}$, hence decreasing the requirement of position resolution to measure the instantaneous velocity, with increasing the particle size. Similarly, the required sensitivity s $< \Delta x\sqrt{\Delta t}$ decreases with increasing the particle size. Therefore, it is easier to measure instantaneous velocity of larger sized particles and has been a good choice for measuring instantaneous velocity in water and acetone [72].

Figure 2.13 shows the hydrodynamic velocity autocorrelation for different viscosity fluids relative to water keeping the same density. It shows that velocity decays faster in relatively higher viscosity fluid and require higher temporal resolution to measure instantaneous velocity in viscous fluids.

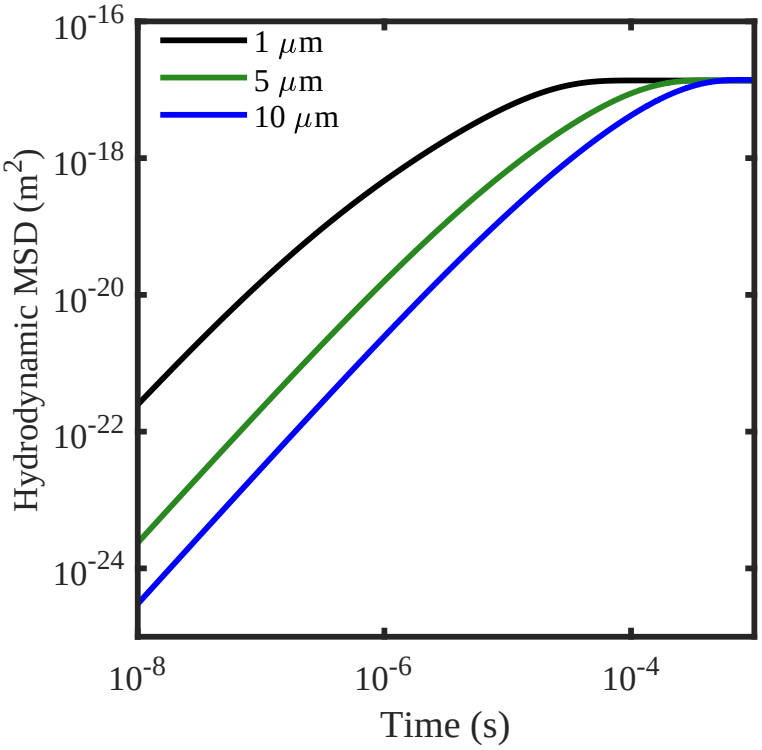

Figure 2.14: **Hydrodynamic Mean Squared Displacement for different sized particles trapped in water at same trap stiffness.** Smaller particle will have larger corner frequency than larger size particle. For smaller sized particle, MSD will be flat for longer time than for larger particle. Larger sized particle has larger τ_p which means its ballistic region will arrive earlier than for smaller sized particles.

Figure 2.14 shows the analytic hydrodynamic MSD of various sized trapped in water with same corner

frequency. MSD is flat at longer time scales but undergoes for $\tau < \tau_k$. The smaller sized particle has relatively larger displacement than for larger, at a given time. Additionally, larger sized particles also drag larger fluid which means hydrodynamic effects are also higher for the larger sized particle.

Similar to velocity autocorrelation analysis, the viscosity of the fluid can be analyzed using MSD of the particle trapped in the specific fluid. Figure 2.15 describe the MSD for various viscosity fluids relative to water. MSD is flat at a longer timescale and has different hydrodynamic effects after the particle is away from the influence of the trap. Higher viscosity fluid has increased hydrodynamic effect and MSD of the particle is larger than for lower viscosity at a given time. It also means that larger spatial resolution is required to measure MSD in lower viscosity medium for given temporal resolution.

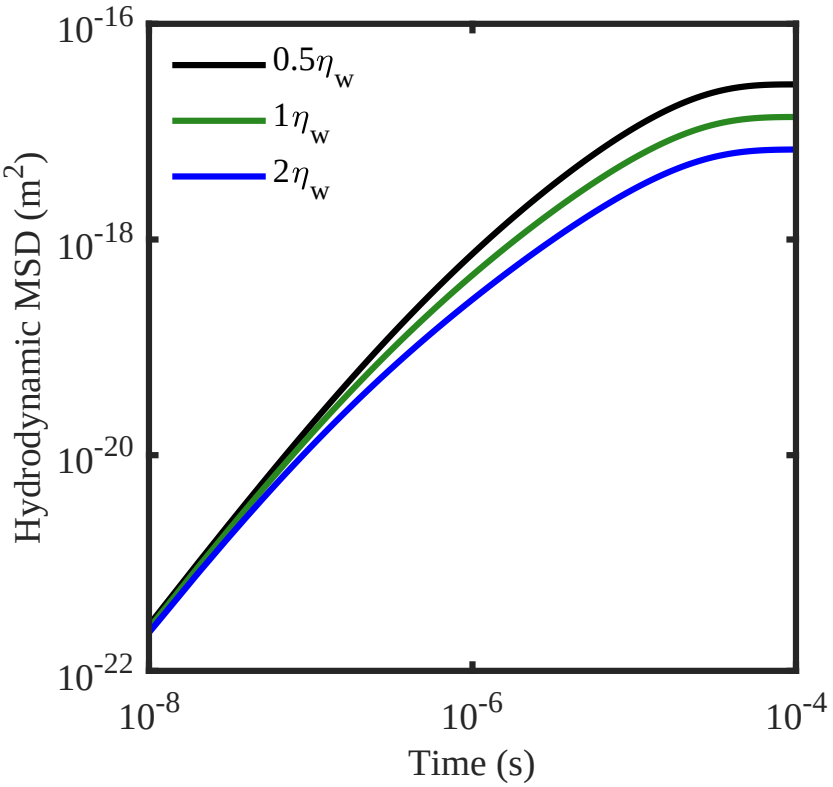

Figure 2.15: **Hydrodynamic MSD for different viscosity fluids at constant trap stiffness relative to water viscosity.** Particle undergoes relatively smaller displacements in denser medium than in lower viscosity fluid. Viscous fluid couple strongly with the particle and hydrodynamic effects are also higher for the viscous medium.

2.4 Conclusions

Light carries momentum and can apply forces on micro/nano-sized particles to trap them. Trapping forces can be accurately described by three different models depending upon the relative size of the particles. In practice, optical forces are applied to the particle which is usually trapped in a fluid and undergoing the Brownian motion. This motion of the particle undergoes free diffusion, transition and ballistic regimes from longer to shorter timescales and it confined by the optical trap depending upon trap stiffness. In the transition from free diffusive to ballistic motion, hydrodynamic effects of fluid interaction with the particle start occurring which increase its effective mass. Based on these effects, the motion of the particle can be analysed by measuring its position and velocity power spectra, mean square displacement and velocity autocorrelation function to differentiate between different sized optically trapped particle in different viscosity fluids.

Chapter 3

Construction and calibration of optical tweezers

3.1 Overview

This chapter describes our efforts to construct optical tweezers that can achieve high stability and state-of-the-art precision. The first part consists of construction and the second part describes the calibration techniques. The main goal of building a customized OT setup is to apply higher trapping forces using 1.3 NA objective and collect the scattered light with the identical objective. The microscope should be stable enough to track the position of the particle at lower frequencies close to 1 Hz, and it should have all the capabilities of easy optical alignment and quick sample change over. Finally, the OT should be able to trap and track a range of particle size typically from a hundred nanometer to several micron sized particles with high temporal and spatial resolution.

For optical trapping, light is tightly focused on a sample specimen using high NA objective and the scattered field is collected using similar or lower NA objective. Higher NA objectives are used to apply and measure larger forces in an optical trap. There are commercially available microscope structures that can be used to mount high NA objective for trapping purpose. However, perfect alignment of 1.3 NA objective (to collect the scattered light) with trapping objective still need customized mechanical design. Correct alignment of 1.3 NA trapping and collection objective (generally called condenser) is a more significant challenge, and at least 5-axis degree of freedom is required for their proper alignment.

There are also commercially available 5-axis travel objective mounts; however, they carry small

weight, typically 500 g or less and are often sensitive to thermal drifts and mechanical vibrations especially when working with higher NA objectives. For these reasons, we have constructed a home-made design of the microscope to mount trapping and condenser objectives with 5-axis degree of relative freedom for easy and robust alignment. The structure is also made heavy for more stability, and design is moderately compact for easy sample change over. This design is mainly inspired by the atomic force microscope (AFM). To track forces and displacements of the trapped particle, a calibration of the detected optical signal is required. The particle is trapped using a 1064 nm laser, and its position is detected using the D-mirror based split detection system. Calibration of OT is done by fitting the power spectrum, including hydrodynamic effects (See Chapter 2).

This optical tweezers can stably trap and track the particles with few Å spatial and less than a μs temporal resolutions. Additionally, it is also capable of measuring the position of the particle at larger frequencies close to 1 Hz.

3.2 Construction of optical tweezers

3.2.1 Overview of experimental setup

To optically trap the particle in three dimensions, a high-intensity gradient is required to apply forces in all directions with net force pointing towards the focus of the beam. For this purpose, We will utilize a continuous wave Gaussian beam, as is the most common choice for OT, but other beam shapes such as Bessel [113] and pulsed Gaussian beam [114] can also be employed for trapping purpose. The schematic of our optical tweezers setup is shown in figure 3.1. In this setup, the laser source is a 1064 nm wavelength Nd: YAG Innolight Prometheus. This laser has a maximum output power of 850 mW and 1.3 mm. $1/e^2$ beam diameter in the fundamental TEM_{00} mode. The trapping objective (Nikon Plan Fluorite, NA1.3, oil immersion) has a back aperture of 6mm, so a 5x beam expander is used to enlarge the beam waist at its back-focal plane.

A combination of half waveplate and beamsplitter is used to control the power going into the objective. It is slightly overfilled to achieve a planer wavefront and a tight focal spot for higher trap stiffness [115]. After the beam expansion, a dichroic mirror is used to direct the laser towards the trapping objective which traps the particles in the sample. Scattered light is collected from another objective, and then the scattered light is directed towards a D-mirror based split detector. A 532 nm diode laser is used to illuminate the sample for visual observation of the particles in the sample.

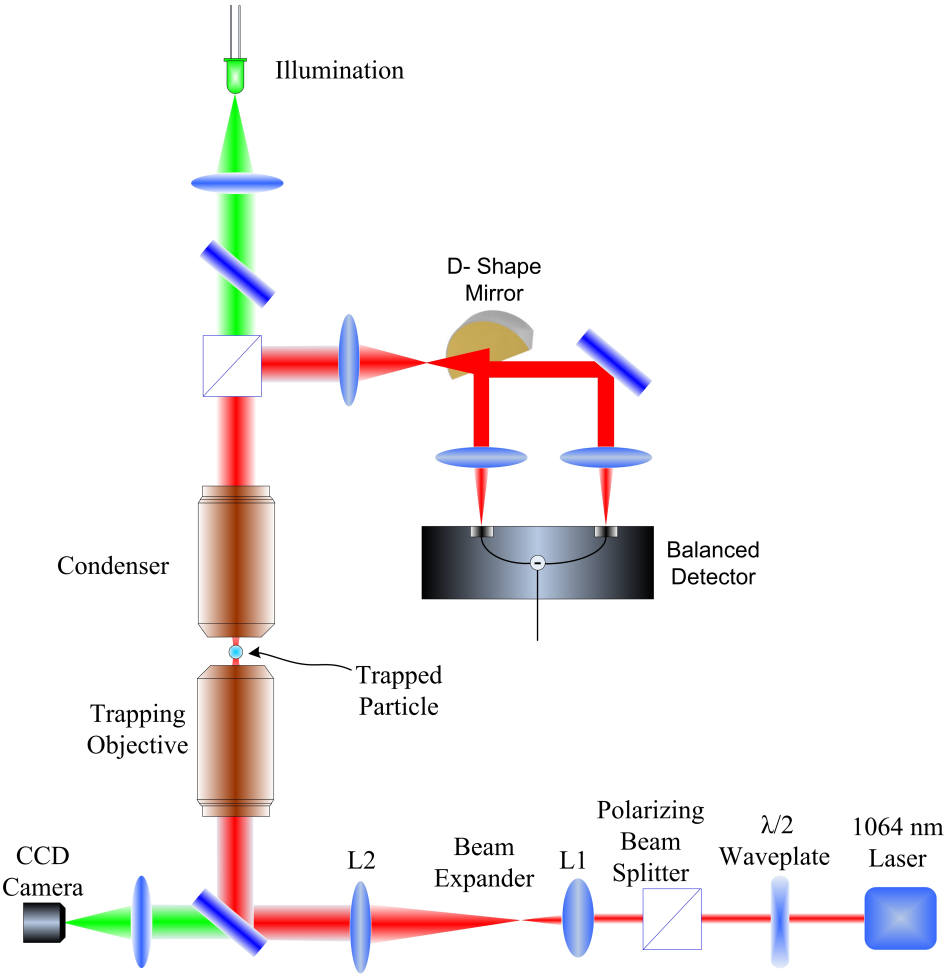

Figure 3.1: **Schematic of optical tweezers setup.** TEM_{00} Gaussian mode is emitted from an Nd: YAG laser, half waveplate and PBS is used to control power going into the microscope, then a beam expander expands the laser beam to slightly overfill the back-aperture of trapping objective. Scattered light is collected from similar specs objective as for trapping. The back-focal plane of the condenser is imaged on a D-shape mirror using a relay lens, and light is then focused on the balanced photodetector to measure the position of the particle.

3.2.2 Microscope Design

The microscope of optical trapping experiments mainly consists of four parts: trapping, collection, illumination, and detection. A stable microscope is very important for particle tracking experiments. We designed the microscope based on the principle that all the parts are mechanically coupled with each other and the optical table so that mechanical vibrations are minimized. For trapping purposes, both water and oil immersion lenses can be used. A water immersion lens has better refractive index matching with water-based sample than an oil immersion lens thus avoiding the spherical aberrations associated with oil immersion objectives. However, there is a disadvantage of water evaporation dur-

ing longer measurement. On the other hand, the oil immersion lens has relatively shorter working distance but have better resistance to thermal drifts and evaporation, and are suitable for measurement which requires more time to set-up. Recently, silicone immersion objective lenses have been introduced which have both better refractive index matching, longer working distance and smaller aberrations which could be a better but expensive choice a water immersion lenses with oil that has n=1.33 can also be used. Details of the design are mentioned in the following paragraphs.

Lower part

A customized 25.4 mm thick and 40 $\times$ 40 cm sized rectangular shaped aluminium plate is made which has three mounting holes in a triangular fashion, i.e. two holes near the two corners and one held in the middle of opposite side. A dichroic mirror is mounted underneath this plate using a right angle kinematic mount to direct the laser into the trapping objective. This plate is mounted firmly on 51.4 mm thick steel posts using brackets (Thorlabs, C1515/M). One end of the steel post is bolted on the optical table, and the other end has customized structures whose purposes are described in the next sections.

A nanopositioner (MAD City Labs: Nano-F200S) which has 200 μm travel distance and 0.2 nm resolution is mounted in the middle of the rectangular plate and trapping objective in tightly screwed on it. This nanopositioner is used to adjust the focus of the trapping objective. Then a motorized two-axis microstage (MAD City Labs: MCL-MOTNZ, 25 $\times$ 25 mm travel distance) is placed on the rectangular plate for coarse lateral movement of the sample and another 2 axis nanopositioner (MAD City Labs: Nano-BioS200) having travel distance 200 $\times$ 200 μm and 0.4 nm resolution is mounted on this microstage.

The sample is placed on the two-axis nanopositioner for experiments. Initial characterization experiments used silica particles (Bang Laboratories Inc, SS04000) dispersed in between two coverslips of thickness 85$\sim$120 μm and then sealed with commercially available fast drying ($\sim$ 1 min) super glue. It is essential that objective and condenser combined working distance should be larger than sample thickness; therefore, care should be taken on selecting the coverslip and sample total thickness.

Upper part

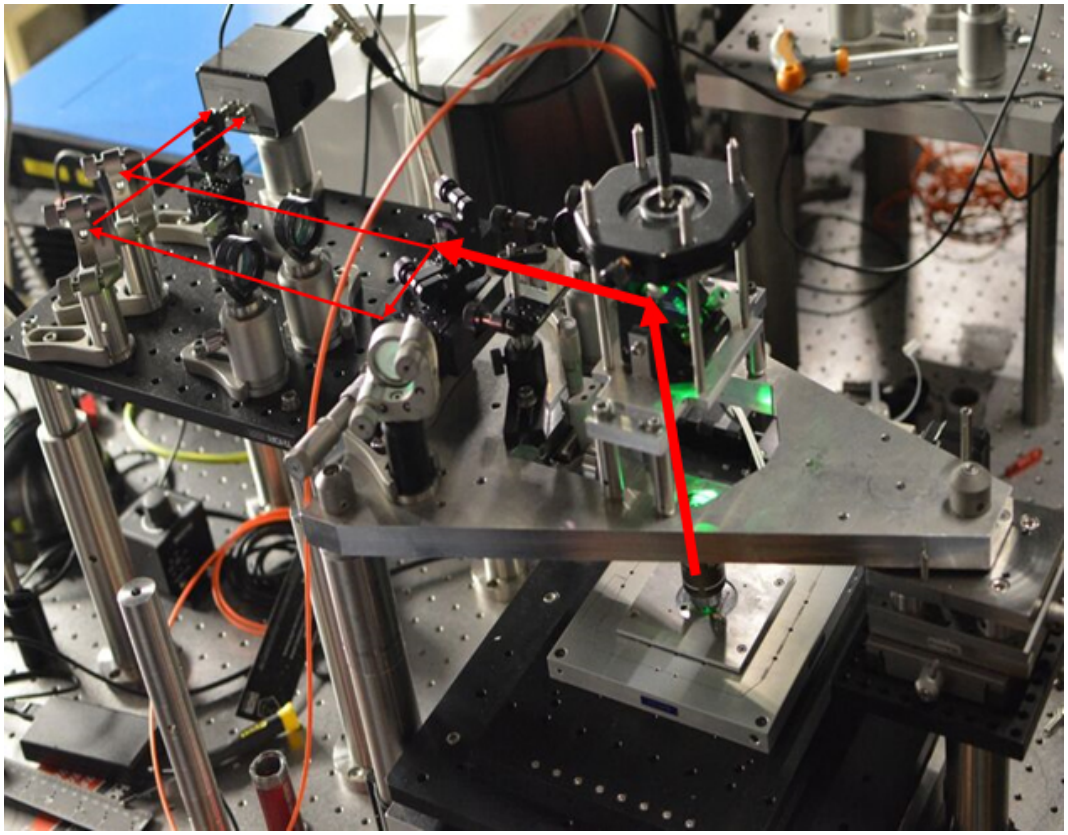

Figure 3.2: **Condenser holder plate design.** A triangular shaped heavy aluminium plate is designed to hold condenser. Each corner of the plate is equipped with vertical movement micrometers for angular alignment of the objective.

The scattered light from the particle is collected using 1.3 NA condenser. In our case, it is identical to trapping objective and is mounted on a $\sim$ 5 kg heavy custom-made holder which have threads for axial movement of the condenser like a vertically mounted microstage. It is made of aluminium which is a smooth material for machining fine threads. It is further attached to a triangular shaped plate whose design is similar to AFM stages for holding AFM scanning tip. In this design, a high load carrying and high precision manual micrometer (Newport: BHC30.10, 40 kg, 4 μm) is attached on each corner of the triangular plate for angular alignment control of the condenser. At one corner, the ball-bearing head of the micrometer is placed in between three coinciding steel balls such that it is touching each ball at only one point. The steel balls are made fixed on the custom steel plate which is mounted on two single axes high load (90 kg) carrying capacity, lockable microstage (Newport: M-UMR8.4) for lateral movement of the triangular plate and hence condenser.

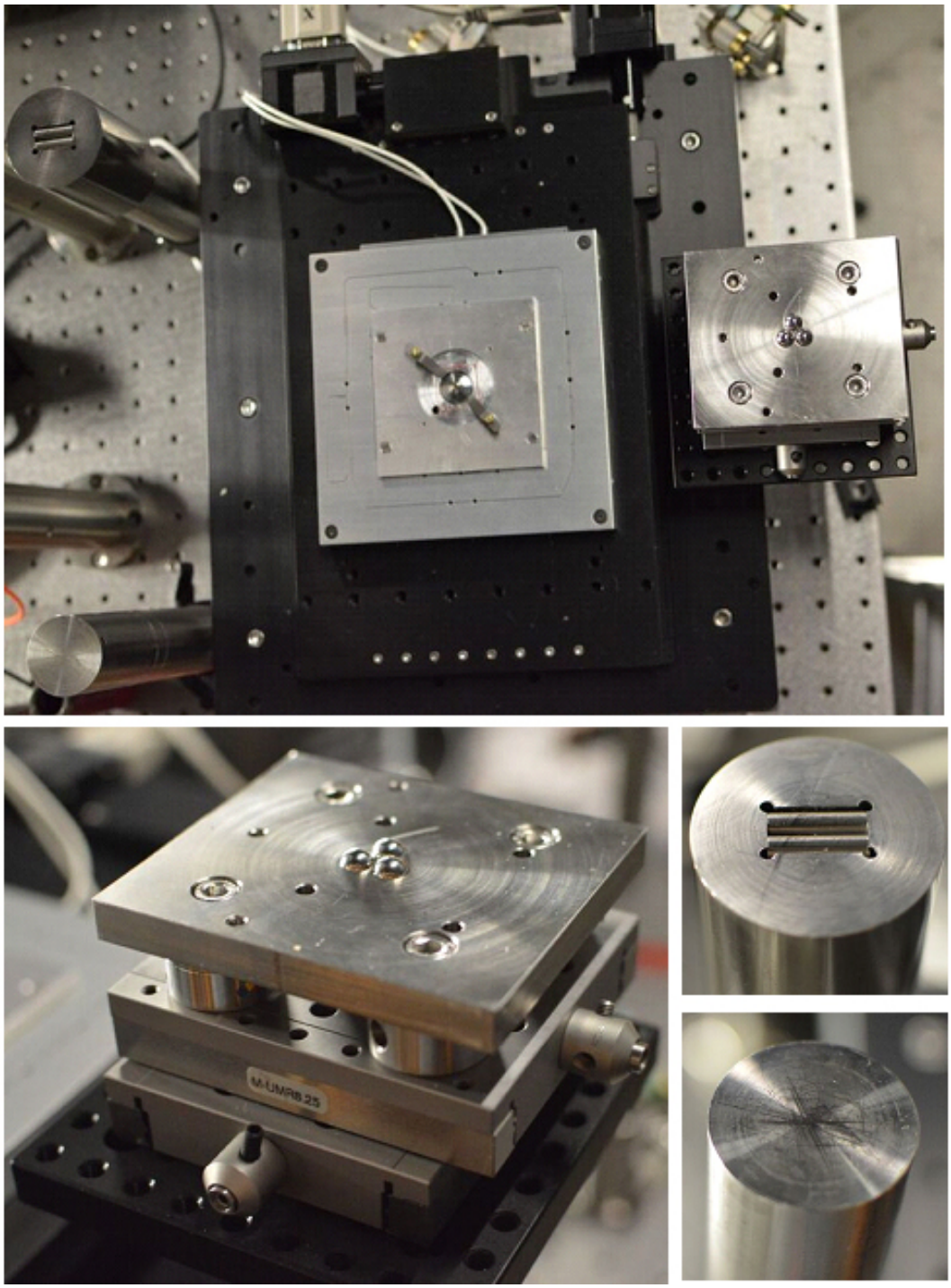

Figure 3.3: **Condenser plate holder design.** The triangular plate is placed on three custom designed base plates. One corner consists of firmly fixed 4 mm steel balls on which one corner of the plate is placed. This corner is equipped with lateral movement stages for lateral alignment of condenser objective. The second corner consists of fixed rails, and the third side is a flat surface.

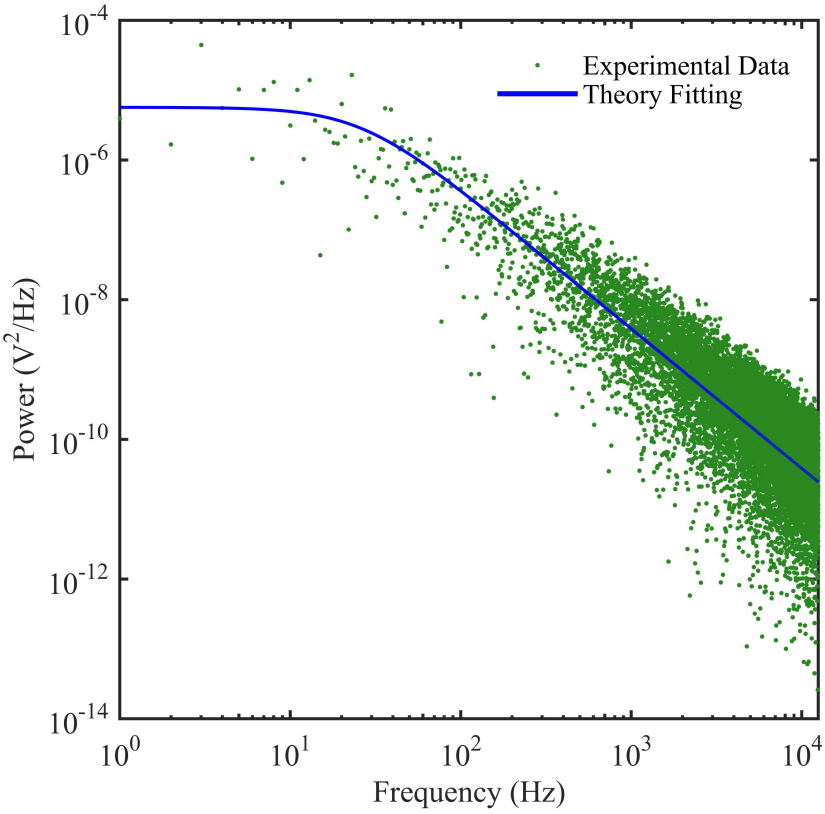

Figure 3.4: **Longer times measurement of the trapped particle.** Green dots are the experimental raw data, and blue is the least-square curve fit which governs trap corner equal to 30 $\pm$3 Hz. This spectrum shows that position information can be extracted for a long time as close as 1s which determines the stability of the OT setup. Measurements are taken for 50 mW optical power on the sample which gives a relatively weak trap stiffness.

Second, axially fixed, micrometer of the plate is placed on steel rails (5 mm $\times$ 10 mm) such that its head makes a single point contact. Finally, the third-micrometer head is placed on the flat surface of the steel post making one point contact, which serves as a freely moving point in the lateral direction for the alignment of triangular plate or condenser. The design of the triangular plate holder is shown in figure.3.3 This design of the upper plate provides robust sample change as it can be mounted and unmounted easily and makes the relative alignment of the objectives simpler which is challenging in case high NA objective and condenser. On the same plate, a fiber-coupled LEDs (Thorlabs: M530F2) based illumination system is set-up imaged on a CCD camera (AVT Manta G-031B). The mechanical design of the condenser holder plate with illumination system is shown in figure.3.2.

For particle tracking, firstly a sample containing particles in prepared and kept on the sample holder. Then the triangular plate is placed, and the alignment of the condenser is performed using the manual stages as mentioned previously. This OT design is quite robust as it provides quick sample changeover

and realigns the microscope easily, stable optical trapping is achieved until some external perturbing force tends to take particle away from the optical trap. From the power spectrum of the trapped particle (which is described in detail in later sections), the motion of the particle can be measured for the frequencies as low as 1 Hz as shown in the figure 3.4.

3.2.3 Interferometric particle detection scheme

To track the position of a particle from the trap center, generally, two types of schemes are used. First one is CCD camera based image processing and the second is interferometric. In-camera tracking, multiple particles can be observed and tracked simultaneously; however, the particles tracking speed is limited by the camera frames per seconds (fps) which is usually at most few thousands of frames per second for a commercial camera. Thus the tracking bandwidth is limited to a few kHz. For fast cameras, the large onboard buffer memory is required to capture and process the acquired images hence limiting the recording time. High-speed cameras or smart cameras can also be employed which are based on center-of-mass tracking, but they are quite expensive and still require large buffer memory [116].

An alternative and relatively cost-effective technique are based on detecting the interference or phase shift in the scattered light of the trapped particle due to its displacement from the trap center. The scattered light from a trapped particle contains information about its displacement from the trap center. The displacement of the particle can be measured by detecting the interference or deflection of light depending upon the size of the particle. In the Rayleigh regime in which particle sizes are smaller than laser wavelength, the particle behaves like a dipole. Light is scattered as a new dipole wave that interferes with the light which has not interacted with the particle. In ray optics regime in which particle sizes are larger than laser wavelength, light is instead deflected at an angle depending upon the particle displacement. In both cases, scattered light is collected by the condenser, and either angular change in the transmitted light or interference pattern are present at the back focal plane.

When a trapped particle is displaced from the trapping axis, the intensity pattern is changed at the back-focal plane of the condenser. Therefore, by imaging the back-focal of the condenser, its possible to track the three-dimensional motion of the particle with high-resolution [9, 42, 117, 118]. To do this, usually transmitted light from the condenser is shined on a quadrant photodiode for three dimension particle tracking. In quadrant photodetector, four diodes are placed in the vicinity such that light is shined on all the diodes. The difference of the sum of diode current governs the lateral movement of

the particle:-

$$S_x = (D_1 + D_2) - (D_3 + D_4), \tag{3.1}$$

$$S_y = (D_1 + D_3) - (D_2 + D_4), \tag{3.2}$$

while the sum of the current of all diodes determine the axial position

$$S_z = D_1 + D_2 + D_3 + D_4, \tag{3.3}$$

where S_x, S_y and S_x are the detector signal in x, y and z-direction respectively and D_1, D_2, D_3, D_4 are four diodes of quadrant photodetector. Commercially available quadrant detector have $\sim$ 1MHz measurement bandwidth. In our setup, the transmitted light is instead directed towards a D-shape mirror, placed at the back-focal plane of the objective using a relay lens and mounted on a linear axis stage for the lateral alignment. D-shape mirror can be used to cut the incident beam into two halves where one half is reflected, and the other half is passed through. Then these light sections are focused on a balanced photodetector which has two well-separated photodiodes joined in an electronic circuit such that resultant current is the subtraction of two diodes and is generally called a balanced detector. This is equivalent to the subtraction current recorded with a quadrant eq. 3.2.3 and facilitates to use high-bandwidth and low electronic noise commercially available detectors. Hence it can provide greater particle tracking bandwidth and sensitivity than a commercial quadrant detector.

As the resultant current from the two diodes is subtracted, only the difference current goes into the inbuilt current amplifier circuit which minimizes the capacitance and saturation requirement of the detector, hence increasing the measurement bandwidth. It can also measure the z-axis motion of the particle based on the similar principle of quadrant detector in which z-axis particle motion changes the focusing diameter of the scattered beam on to the photodiode which can be measured according to Eq. 3.3. In our experiment, we are only tracking x-axis motion of the particle. Data from the detector is recorded using high speed and resolution digitizer (Infiniium DSOS204A, 10 Bit, DC to 2 GHz). Using back-focal-plane interferometry based detection system, particles can be tracked with Angstrom spatial and microsecond temporal resolution. Apart from this detection system, particles can also be tracked using digital video microscopy with millisecond and nanometer resolution [119, 120]. Schematic of optical tweezers with D-shape mirror based detection is shown in figure.3.1.

There is another type of particle position and force detector called position sensitive detector (PSD) whose signal is proportional to the position of the laser intensity centroid on the detector element, and this is directly proportional to the applied optical force. Unlike quadrant style photodiodes, PSDs are independent of beam size and shape. As long as the scattered light is hitting the detector, centroid position can be tracked using PSDs. In contrast to QPD, a PSD possesses several electrical contacts. This results in a distribution of the photocurrent among the contacts, depending on the position of the laser spot

3.2.4 Optical Tweezers calibration

In OT, the position of the particle is detected using a photodetector which governs signal in the units for volts instead of physical units. Therefore, it is necessary to do volts-to-meter conversion to measure the applied force and trap stiffness in physical units. This calibration can be performed using active or passive techniques. In active calibration techniques, an external force field is applied to the particles whereas in passive techniques only the thermal fluctuations of the fluid's molecules are responsible for displacing the particles. Both types of techniques are based on relating the time-dependent probe particle trajectories to the fluid properties and can be used for position and force calibration both in simple and complex biological environments.

Both types of techniques govern the same calibration parameters; however, active techniques require a motorized or piezo-stage to displace trap the particle relative to trap center and require more instrumentation yet they are more reliable for calibration in complex biological environment [50]. On the other hand, passive techniques are relatively easy to implement and can be used for OT calibration in a pure solvent like water. Calibration of both trap stiffness and determining volt-to-meter conversion is required to further calibrate applied optical force on the particle in physical units. Following is some discussion about methods to calibrate OT.

Equipartition theorem analysis

The Equipartition theorem is a fundamental theorem of thermodynamics which states that each degree of freedom in a physical system at thermal equilibrium possesses $\frac{1}{2}k_BT$ of energy. As the optical trap gives a harmonic potential, the trapped particle contains $\frac{1}{2}\kappa x^2$ energy where x is the displacement from the trap center. At thermal equilibrium with temperature T, the average energy of the trapped

particle will be equal to the thermal energy.

$$\frac{1}{2}\kappa\langle x^2\rangle = \frac{1}{2}k_B T, \tag{3.4}$$

where $\langle x^2\rangle$ is the mean square displacement of the particle which is caused due to random collisions of the fluid molecules with the particle. Once the displacement is normalized into physical units, trap stiffness can be measured with high precision. This method of determining the trap stiffness requires a calibrated position sensing device in units of a meter, but does not require calculating the viscous drag coefficient γ of the trapped bead or knowing the viscosity of surrounding medium η and hence can be used in an unknown viscosity environment. However, it requires a position calibrated detector in physical units which can be done by scanning the laser over a stuck particle for a known displacement [121, 122].

Although trap stiffness can be measured accurately using this method, it involves two steps: first determining the detector sensitivity, i.e. volt-to-meter conversion using stuck particle in the same sample and then trapping another freely floating particle in the sample. This adds up the complexity of calibration when the particle needs to be trapped inside the biological cell where making the particle stuck is not easy. Additionally, this method is not suitable for calibration at higher trapping power and as compared to other following methods, offers smaller reliability in determining the stiffness at higher power typically larger than few hundreds of *mW* [123].

Power spectrum Analysis

Apart from equipartition theorem, the motion of the particle in an optical trap can be given by Langevin equation from which power spectrum, MSD and position autocorrelation function are deduced and can be used to calibrate the OT. In this regard, the power spectrum analysis of a trapped particle provides a robust way of determining trap stiffness and the volt-to-meter conversion factor. A freely moving particle in water exhibit Brownian motion, which has a mechanical power spectrum that scales with the inverse square of the frequency. The optical trap suppresses low-frequency motion, resulting in a spectrally flat region at low frequency. The corner frequency f_c quantifies the transition between these two spectral regions and is directly proportional to the trap stiffness. The power spectrum of the particle can be described using Eq. 2.3.3 [54, 110]:-

$$P_x = \frac{D}{2\pi^2}\frac{1}{f^2 + f_c^2} \tag{3.5}$$

Therefore, by measuring the power spectrum of the position of a particle, analytic eq.3.5 can be used to fit the spectrum using least-square methods with f_c as an unknown fitting parameter and trap stiffness can be determined from the expression $\kappa = 2\pi\gamma f_c$. Additionally, volts-to-meter conversion factor can also be determined by the following equation:-

$$c_f = \sqrt{\frac{D_{exp}}{D}}, \tag{3.6}$$

where D and D_{exp} are theoretical and experimentally measured diffusion constants respectively. After determining the calibration factor in the units of V/m and trap stiffness from the corner frequency, displacement signal is divided by the c_f to determine the applied forces F, MSD and C_v etc in physical units. This method governs the highest sensitivity for change in trap stiffness due to particle size variation and also provides information about the presence of classical noises of the OT system. Additionally, it can also give information about the drag coefficient of arbitrarily shaped trapped particles [121].

Mean square displacement analysis

Another useful characterization of the Brownian particle is determining its mean squared displacement which quantifies how much it has displaced from the equilibrium position. For an optically trapped particle, it can be determined using the following equation [55]:-

$$MSD(\tau) = 2\frac{k_B T}{\kappa_x}\left\{1 - e^{-|\tau|\gamma/\kappa_x}\right\} \tag{3.7}$$

At short timescales in the free diffusive regime, the motion of the particle is linear while at longer timescales, it is constrained by the optical trap. By measuring the MSD of the particle, Eq. 3.2.4 can be computationally fitted using the least square method with trap stiffness κ and γ as the fitting parameters to determine their values accurately. Hence, optical tweezers can also be calibrated using this MSD method.

Position Autocorrelation Analysis

Position autocorrelation function calculates the autocorrelation of the randomly fluctuating position signal. In an OT, it determines how much the position of the particle is correlated with the successive position at a given amount of time or how much time the particle takes to reach a new position. From

the Langevin equation, it can be given by:-

$$C_p(t) = \frac{k_B T}{\kappa} e^{-|t|\gamma/\kappa} \tag{3.8}$$

Experimental particle position autocorrelation function can be computationally fitted using the least square method with trap stiffness κ and γ as the unknown fitting parameters. Calibration using position autocorrelation function is straightforward and easy to implement as compared to other techniques. Moreover, this method is particularly suitable for the presence of non-spherical particles and non-conservative effects in the sample. It has been used to measure the unknown viscosity of different water-based solutions [67].

3.2.5 Calibration including the hydrodynamic effects

All the above-mentioned calibration techniques are valid for timescales much longer than the fluid-particle interaction time τ_f. As described in the previous chapter, when a particle undergoes free Brownian motion, the particle drags fluid with it, but the dragged mass does not influence its future position. However, at shorter times scales, the dragged fluid retains the current position information of the particle which influences its next position which is like the position memory effect and is generally called the hydrodynamic effect. Therefore, a complete theory including hydrodynamic effects is essential to be used for OT calibration which could be used for both timescales shorter or larger than τ_f. Additionally, it has been shown that neglecting the hydrodynamic memory effects in the Brownian motion measurement causes an underestimation of more than 10 % in detector sensitivity and traps stiffness for particles as small as 0.27 μm and sampling frequency larger than 200 kHz. Therefore, it is essential to include the hydrodynamic memory effects and use the expression of the power spectrum and mean square displacement which includes the memory functions [109, 110].

Figure.3.5 shows the powerspectrum of $1\mu m$ particle trapped with 330 mW of optical power on the sample, having a corner frequency of 5.06 kHz which shows a very stiff optical trap. The averaged powerspectrum shows an excellent agreement with hydrodynamic theory. Generally the particle motion is influenced by the fluid properties however, there are other factors which can affect the Brownian motion of the particle. For example, boundary effects are present when the particle is very close to the surface of coverslip typically for less than 2 μm and are very minimal beyond this distance. In our experiments, 1 μm particle has been kept at a distance of 6 μm from lower coverslip and 15-20 μm from upper coverslip in the sample chamber. Therefore, for small changes in the particle or fluid parameters, boundary effects are very minimal in our experiments and haven't been accounted for,

although including these effects will give more accurate results [54]. Additionally, the number of particles in the sample are kept very low and usually, 1 μ m particle is present per 500 μm. Therefore, Casimir forces which arise due to the presence of other particles in the vicinity usually at a distance less than 200 nm, are negligible.

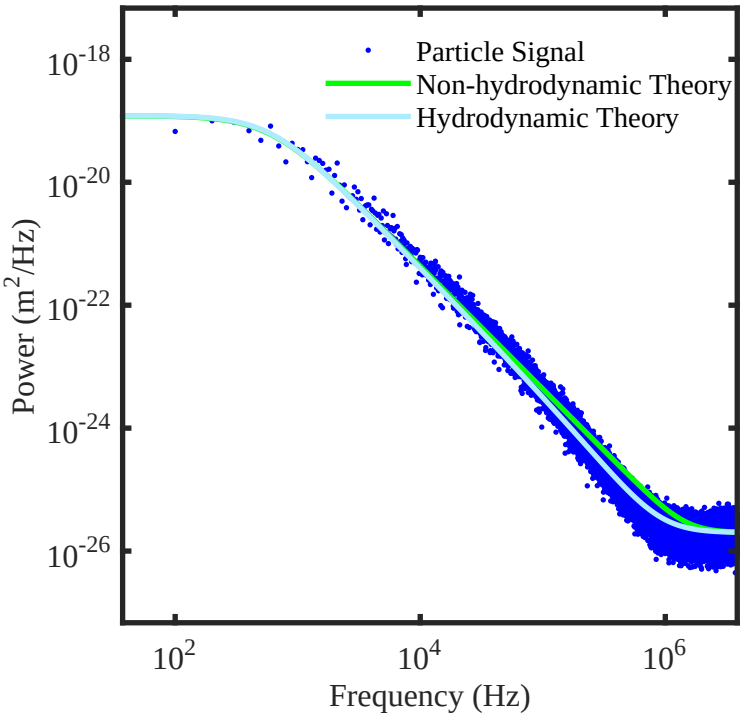

Figure 3.5: **Position power spectrum of optically trapped particle.** Green dots show the position amplitude of the particle averaged over 10 successive points and the blue color line shows the theoretical least square curve fit which includes hydrodynamic memory effects given by Eq. 2.3.3. The flat region shows the confinement of particle by the optical trap at lower frequencies while it undergoes free Brownian motion at higher frequencies

.

Similarly in time domain, MSD of the particle can also be calculated. In practice, its MSD has the contribution from the laser noise. Therefore, it is not an independent measurement of MSD; rather it is the sum of MSD of trapped particle and MSD of the laser noise. This laser noise is uncorrelated to the motion of the particle and appears only as an offset in the measured MSD. Therefore, MSD of laser noise which is measured in the absence of trapped particle should be subtracted from total MSD to govern MSD from particle alone [71].

$$MSD_p(\tau) = MSD_t(\tau) - MSD_n(\tau) \tag{3.9}$$

Figure.3.6 shows the MSD of the trapped particles. MSD of laser noise is subtracted from the particle signal to determine the MSD of the particle from the total signal. It has an excellent agreement with MSD theory including hydrodynamic effects.

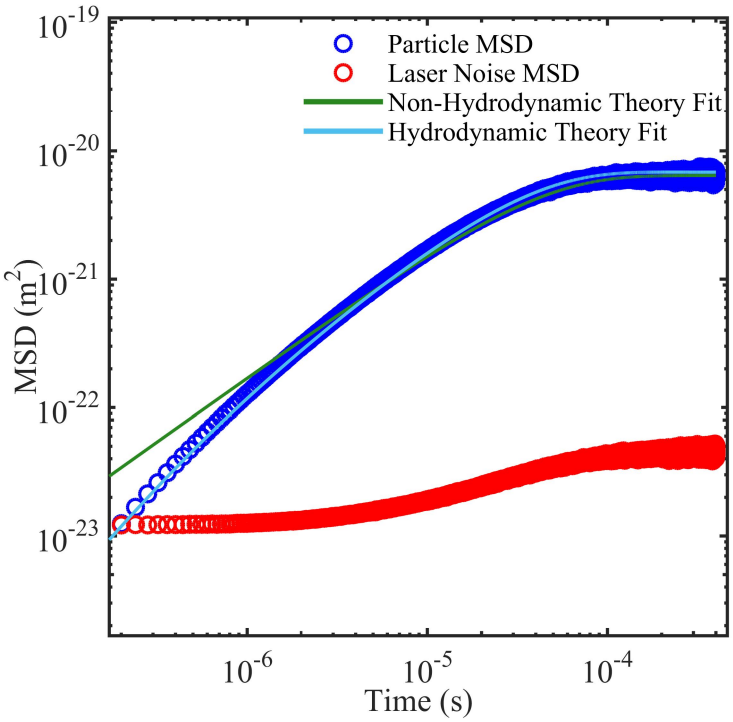

Figure 3.6: **Hydrodynamic MSD of the trapped particle.** The flatline at longer timescale shows particle is optically trapped while at shorter timescale, particle undergoes free Brownian motion. Measured MSD of trapped particle agrees well with hydrodynamic theory.

3.2.6 Spatial and temporal resolution of Brownian particle

Once OT and particle tracking systems are set-up, it is important to characterize it in terms of spatial and temporal resolution of the measurement system. For Brownian motion measurement, this resolution can be described as the minimum mean square displacement that can be measured in an OT system at a minimum measured time. At longer timescales, MSD is flat due to trap potential confinement while at short time, it scales with power one or two until the laser noise becomes dominant. The minimum point where MSD of the particle is larger than for the laser noise determines the spatial and temporal resolution of OT. Based on this, we have achieved 0.1 μs temporal and 3.1 Å resolution for 1 μm.

3.2.7 Conclusions

We have constructed a stable microscope using a 1.3 NA objective to trap the particle and similar 1.3 NA condenser objective to collect the scattered light. Mechanical design of the microscope is quite robust and, provides angular and lateral controls for easy alignment of high NA objectives for fast-tracking of the trapped particles. Calibration is done using hydrodynamic theory based power spectrum of the trapped particle to determine the trap stiffness and detector position measurements conversion factor from volts-to-meter.

Then, using the mean square displacement analysis, spatial and temporal resolutions of the system is determined which are the important parameters to observe the Brownian motion of a particle at fast times scales typically in ballistic regime. Stability of the microscope is assessed from the power spectrum which shows measurable particle signal for as long as 1s. Additionally, we are also able to determine the position of the particle at timescale as small as 0.1 μs and 3.1 Å for 1 μm silica particle. This optical tweezers setup can be employed for several biological and fundamental physics applications.

Chapter 4

Ultra-fast optical tweezers for viscosity measurement

4.1 Overview

In this chapter, an elegant technique is described which could allow measurement of the Brownian motion of a particle in the ballistic regime for standard biologically compatible optical tweezers. The chapter starts by giving an intuitive explanation of how the filter works. It is shown theoretically that up to 82.7 % of the signal can be transmitted while not detecting the trap field. The experimental setup is described and the experimental results are presented. The spatial filter allows a reduction of 10^3 to 10^4 in optical power, thereby allowing the full signal from a high power optical tweezer to be detected on a standard commercial detector. In the experiment we achieve bandwidths up to $\sim$ 10.75$\pm$ 0.46 MHz for a 1μm silica particle in water, surpassing state-of-the-art. We explore the options for extracting further information from the acquired data and show that we can extract the viscosity of the liquid around the particle.

4.2 Split-flipped waveplate based detection scheme

In standard OT, the quadrant photodetector or the D-mirror based balanced detection scheme is employed for particle tracking. In both techniques, all the scattered light is illuminated on the detector which saturates the commercial photodetector at reasonably low power $< 5mW$. In principle, only the fraction of light carries the displacement information of the particle and detecting all the scattered light is not required except collecting enough light to overcome the electronic noise of the system. However, in standard detection techniques, all the scattered light is detected and this principle is the

major limitation in acquiring higher measurement bandwidth as it saturates the detector.

Typically, particles are trapped with few hundreds mW of optical power to acquire higher trap stiffness; however, commercial detectors are not designed to detect this enormous amount of light to acquire higher bandwidth and can only handle few mW of power, thus limiting the possible effective measurement bandwidth. Recently, higher bandwidth has been achieved using customized high power damage threshold photodetector which can detect 140 mW power [72].

However, this still has not been sufficient to detect ballistic motion of standard particles under standard conditions, such as 1μm silica in water. Additionally, electronic design of the detector is quite complicated and may not be readily accessible to wider optical tweezers community. Therefore, an alternative technique is required to filter out the more substantial portion of scattered light possessing more than 99% of light having no displacement of the particle information, so that fraction of scattered light with useful information can be detected with commercially available fast measurement detectors.

Here we develop a technique based on a spatial filter which separates the optical signal from a trapped particle from the unscattered light. The spatial filter allows a reduction of 10^3 to 10^4 in optical power, without attenuating the signal. Thereby the spatial filter solves the problem of detector saturation, and a commercial detector can be used to detect the full signal. The filter is constructed using a split-waveplate and a single mode optical fiber. The split-wave plate turns even optical modes into odd and vice verse. The single mode fiber only allows the even fundamental mode to enter. The filter can thereby suppress even modes, while it can transmit light from an odd mode. The trap field is in an even mode and is thus heavily suppressed. The signal from a displaced particle is in an odd mode, and the filter is optimized to maximize transmission of this signal.

The optical mode of light scattered from 1μm silica is a combination of dipole scattering and geometrical scattering as described by Lorenz-Mie theory. To get an intuitive understanding of the filter process, assume that the trap field is in the fundamental Gaussian mode and that the particle scatters fundamental and other Gaussian modes. The trap field can be written as

$$E_{usct} \approx Ae^{-x^2/w_0^2}, \tag{4.1}$$

where x will be the coordinate of trap center and A is a normalization constant depending upon the particle, medium and incident wave parameters. Under the above assumption, when a trapped particle is moved from the center of the trap at a small nano-metric displacement, the scattered field from the

particle can be approximated

$$E_{sct} \approx Be^{-(x-\delta x)^2/w_0^2}, \tag{4.2}$$

where δx is the particle displacement, and B is proportional to A and the particle scattering cross section. Figure 4.1 shows the simple Gaussian function when displaced by a small distance δx.

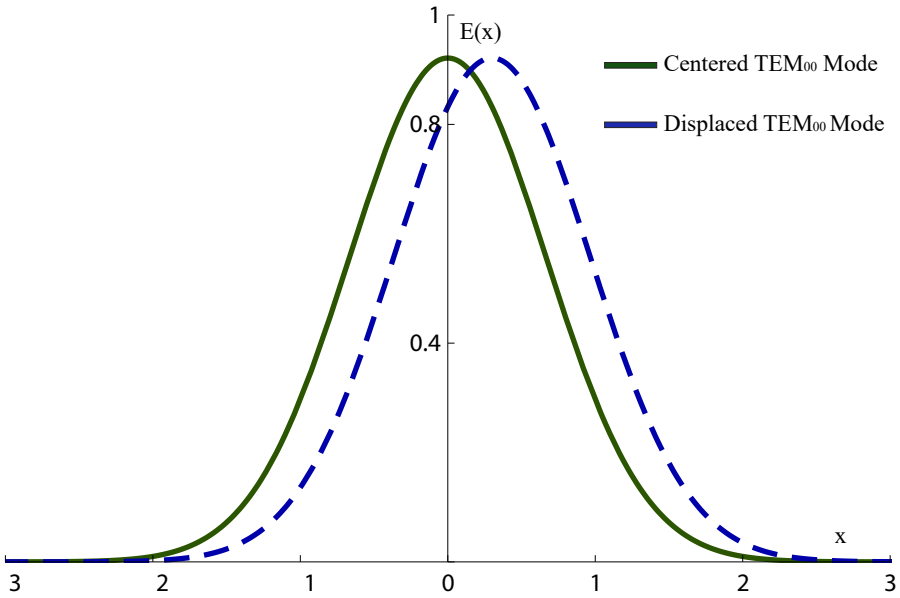

Figure 4.1: **Scattered field from the trapped particle.** When the particle is in the center, then the Gaussian mode is also in the center. When the particle is displaced by δx, the Gaussian field also displaces accordingly. The x-axis units are normalised by the beam waist.

The scattered field can be further expanded into smaller amplitude terms using Taylor series as

$$E_{sct} \approx Be^{-x^2/w_0^2} - \frac{2Bx(e^{-x^2/w_0^2})\delta x}{w_0^2} + O[\delta x^2]. \tag{4.3}$$

The first term in Eq. 4.2 is independent of the particle displacement. The second term which is proportional to δx will, therefore, contain all the information of small displacements. In terms of optical modes, the first and second term can be called as Transverse Electromagnetic TEM_{00} and TEM_{10} modes. These modes are displayed in figure 4.2 where it can be seen that the 01 mode (green) is antisymmetric around the origin. This means that the optical mode which carries the information is an odd mode while the optical modes of the trap field and scattered field, from the particle which do not carry information, are symmetric.

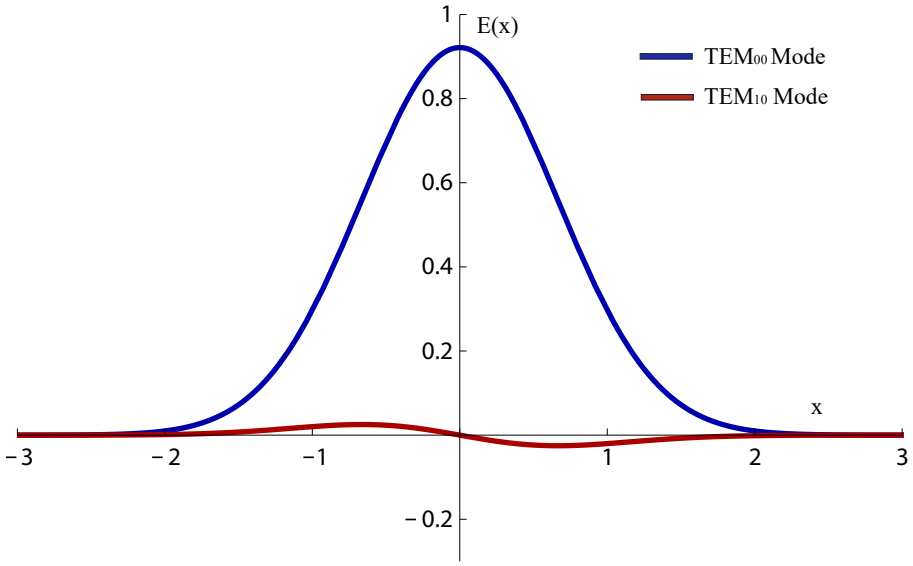

Figure 4.2: **Scattered field modes.** Scattered Gaussian mode can be expanded in terms of other higher order TEM_{00} and TEM_{10} modes.The x-axis units are normalised by the beam waist.

As an approximation, higher order terms O can be neglected for nanometer-sized displacement as they have a very low amplitude ($< 10^3$) as compared to first two modes; therefore, the scattered field can be approximated to first two terms in Eq. 4.2. This expression is an approximation to understand the basic principle of governing techniques; however, full electromagnetic theory based on Mie Scattering can describe more accurate electric field profile. In the scattered field, almost all the light is present TEM_{00} mode and the only fraction of light usually in femtowatt is present in other modes. The information of the particle displacement is present only in higher order odd modes mainly in TEM_{10}, which means that collecting and detecting TEM_{00} mode is not useful except generating enough current to overcome the electronic noise.

To do this, we have developed an alternative technique using a split-flipped waveplate (SFWP) which is very simple and robust to use. It can be made by taking a commercially available half-waveplate, cut into two halves, flip one half of the plate along the vertical axis and then join the two cut sections. When half of the light is passed through the un-flipped section and another half from the flipped section, then there will be a π phase shift between two halves. This π phase shift on one half will reverse the mode shapes of scattered light. Therefore, one half of light will be passed unchanged, and another half will have opposite mode shapes, converting the even modes in odd and odd modes into even as shown in figure 4.3. We called these modes as flipped TEM_{00} and flipped TEM_{10} modes.

When these modes are focused on the single-mode fiber, the trap field flipped TEM_{00} which is now in an odd mode are entirely suppressed as it has zero overlap with the even fundamental mode of the

fiber. However, the symmetric flipped TEM_{10} mode which carries the information of the particle will have a limited overlap with the fiber as shown in figure 4.4.

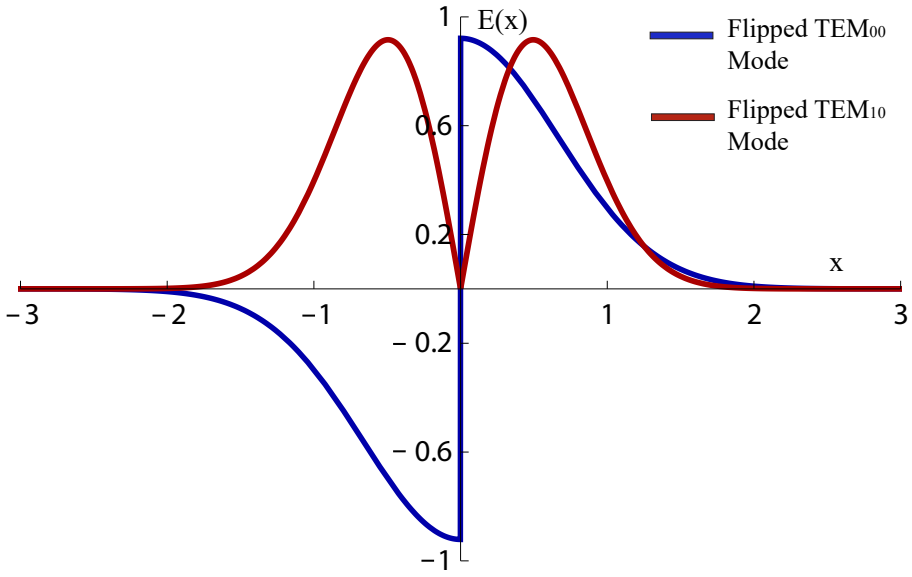

Figure 4.3: **Flipped modes.** When the waveplate is introduced in the center, it flips the mode only in one half, converting odd mode into even and vice versa.The x-axis units are normalised by the beam waist.

This overlap can be optimized by changing the waist of the flipped TEM_{10} mode using lenses, and maximum efficiency of 82% can be achieved for 0.54λ. The intensity of flipped TEM_{10} modes can be described by

$$I_e = \left\{ \int (Ae^{-x^2/w_0})(sgn(B\frac{(e^{-x^2/w_0^2})x\delta x}{w_0^2}))dx \right\}^2, \tag{4.4}$$

where A and B are normalization constants for Gaussian and flipped TEM_{10} mode. *sgn* function acts on TEM_{10} mode and flips one half of the electric field to convert it from being an odd mode to even mode.

Using this spatial light filtering technique, even Gaussian modes, which carry most of the light and are the primary reason for saturation of the photodetector, are filtered out. Therefore, the only a fraction of light carrying particle displacement information is shined on the photodetector. This greatly enhances the capability of the detection system to put more light on the detector and acquire larger signal-to-noise ratio which in turn will increase the measurement bandwidth depending upon the flipped TEM_{10} mode coupling efficiency.

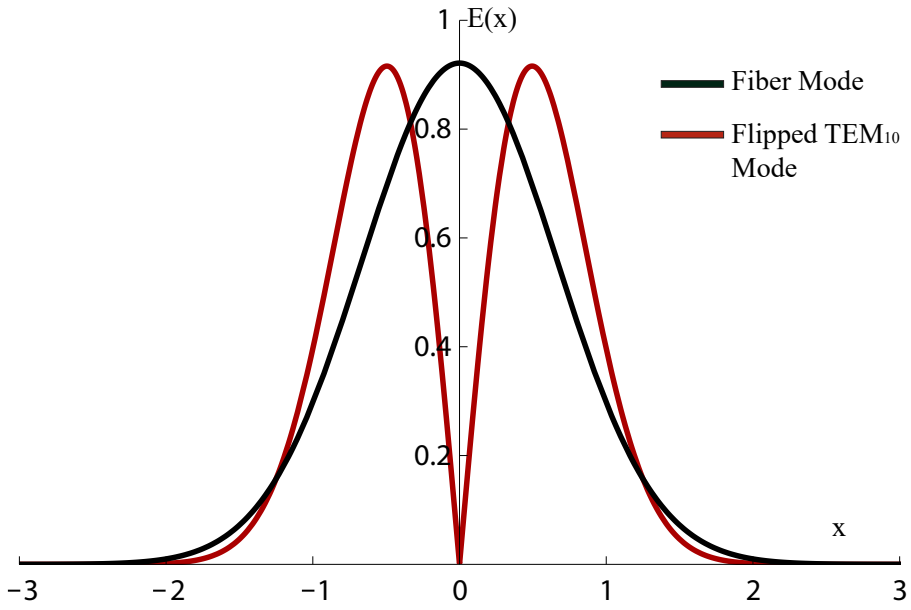

Figure 4.4: **Coupling Flipped TEM $_{10}$ mode to the fiber.** The flipped HG 01 mode is even mode and can couple into the single mode fiber mode which can be approximated as the fundamental Gaussian mode. The x-axis units are normalised by the beam waist.

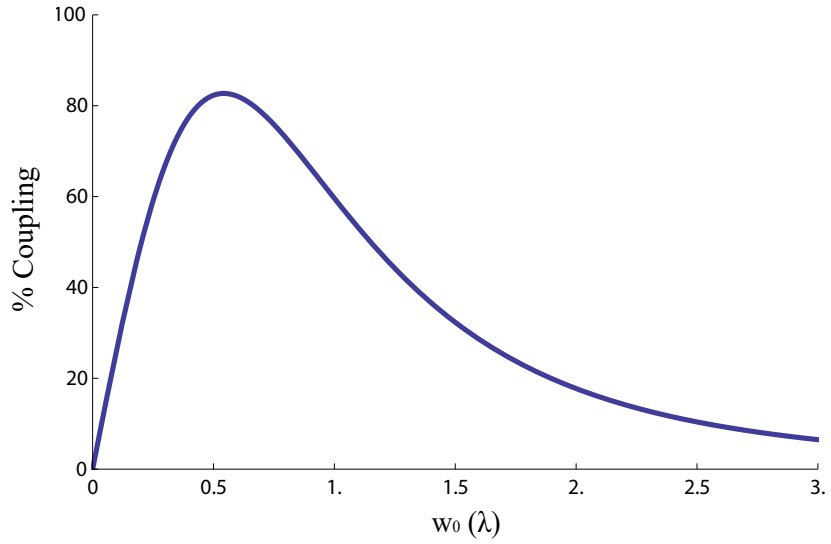

Figure 4.5: **Coupling efficiency of flipped TEM$_{10}$ mode.** It depends upon the waist of the flipped HG 01 modes which can be changed experimentally using set of lenses. The maximum coupling efficiency of 82.7 % is achieved for beam waist equal to 0.54λ.

It is notable that the waveplate based detection method does not remove information of whether the particle direction. This method detects the amplitude of the asymmetric mode, which can be both positive and negative. In the current setup, one-dimensional position information is extracted. But,

the overall method does not have the limitation of three-dimensional particle tracking and a more complicated optical setup can be constructed to do three-dimensional particle tracking using flipped waveplate. Similar techniques of modes flipping have been employed recently for high-resolution imaging. Ping Koy Lam supplied the flipped split waveplate for our experiment.

4.2.1 High bandwidth particle tracking measurements

Based on the idea mentioned above, the waveplate is placed in the optical setup as shown in figure 4.6. Scattered light collected from the condenser is passed through a half-wave plate and polarizing beam-splitter which transmits some light $< 0.5mW$ towards D-shape detection platform where a balanced photodetector (Newport, 1807-FC) is placed. The rest of the light having 6 mm diameter is directed to the SFWP detection platform. SFWP is placed at the back-focal-plane of the condenser-objective, same as a D-shaped mirror. It is mounted on linear and rotational microstages, which are perpendicular to the laser beam axis. The diameter of the beam transmitting from the SFWP is decreased from 6 mm to 2 mm using collimation lenses of 150 mm and 75 mm respectively to increase the coupling efficiency in the fiber. Then the beam is directed towards the single-mode fiber using a combination of mirrors and focused on the fiber tip using an aspheric lens having 4.1 mm focal length which is fixed on a rotational mount. The position of this lens is carefully changed to maximize the coupling efficiency.

The waveplate can now be aligned for maximal suppression of the trapping field, typically giving a suppression down to 10^{-4}. To do this, firstly, all the scattered modes are passed through one half of the flipped plate and then it is displaced towards the beam center using linear microstage until maximum suppression is achieved. This suppression is highly sensitive to vibrations but is typically stable for $\sim$1 minute. To enhance the signal in the flipped mode so that a more significant signal is acquired to overcome the electronic noise, a phase reference field is required. This field needs to be phase locked with the signal field, but independent of the particle position. Conveniently this local oscillator is obtained by displacing the waveplate a little from maximum suppression to allow 1 mW power to enter the fiber.

The output light from the single mode fiber is illuminated on to a photodetector (Thorlabs, PDA10A). The photo-current is high-passed with a 100 kHz filter, amplified, low passed at 32 MHz and then digitized with a fast 12-bit oscilloscope sampled at 100 MHz. The high pass filter is used because the 12 bits are insufficient to digitize the full signal. The amplifier reduces the influence of electronic pick-up from the cables. The low-pass filter avoids aliasing from frequencies above the Nyquist

frequency.

With 1 mW of power, the detector has around 6 dB of clearance between electronic noise and shot noise. 1 mW is used to stay clear of saturation (at 1.4 mW) and at the same time maximise clearance to the electronic noise. With 1 mW of power, the laser is shot-noise limited at frequencies greater than ~ 4 MHz. Below this frequency, a noise-eater in the laser creates some high frequency excess classical noise. To reduce this noise contribution at lower frequencies, we record a reference beam on an identical photodiode before the microscope. This reference beam is separated from the optical before going into the microscope using a polarising beam splitter and delivered to the second single-diode photodetector using free-space optics. This reference beam is digitalized in the same way as the signal field and can be subtracted in post-processing. This procedure eliminates the classical noise same as the balanced detector does and signal approaches the shot-noise. As this is not an interferometric measurement, therefore, reference and particle signal beams are not required to be phase-locked.

It is important to note that a balanced detection approach is used in both techniques which allows particle position measurement only in one direction. Although, three-dimensional position information can be acquired using the quadrant photodetector most of the commercially available quadrant detectors are not high-bandwidth detectors. On the other hand, commercial balanced detectors provide high measurement bandwidth, but they usually have low saturation power typically less than 500 μ W. As our purpose is to compare our proposed detection scheme with previously available fast detection scheme, therefore, we used a balanced photodetector instead quadrant photodetector. For both types of detection schemes, the more complicated optical setup can be constructed to separate the scattered beam into four halves and then adding/subtracting them in the same manner as quadrant detector does to acquire three-dimensional particle information.

The experimental procedure is as follows. The sample is placed in the microscope, and the light is aligned with the single mode fiber without the waveplate. The waveplate is then moved to maximum suppression and then moved to allow a 1 mW local oscillator. The measurement is taken after this procedure and repeated for every measurement. The data is binned in 5 and then plotted as shown in the figure. Here 160 mW was sent on to the spatial filter. This data is distinguishable from normal Brownian noise as it looks like it has been low-pass filtered at around 1.6 MHz. This is, however not the case; instead, the momentum of the particle dominates the thermal noise, as is the main characteristic of ballistic motion.

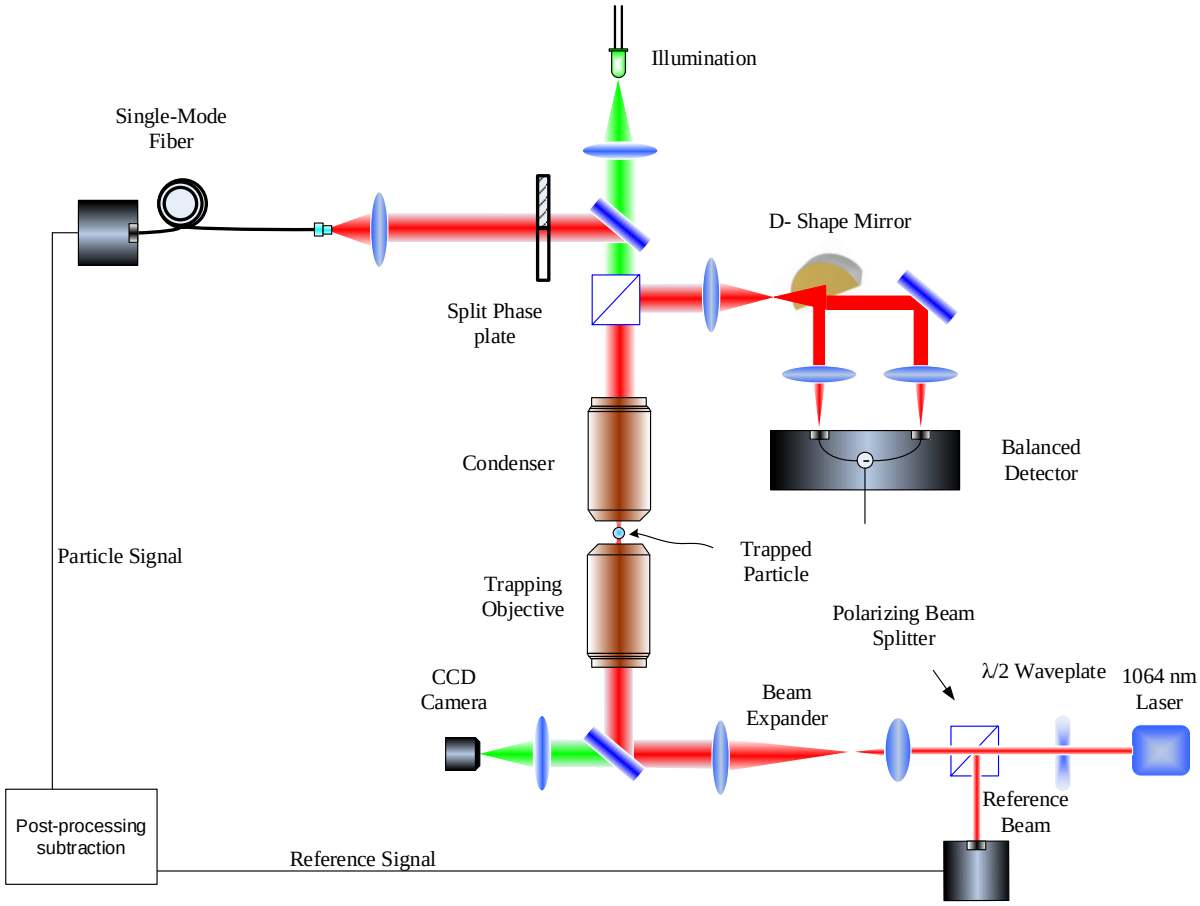

Figure 4.6: **Schematic of complete optical setup.** This schematic includes both D-mirror and waveplate based detection schemes. The scattered light from the trapped particle is distributed towards both detection systems using a combination of a half waveplate and a polarizing beam-splitter. The waveplate is placed at the back-focal-plane of the objective similar to the position of the D-mirror. Then the light is focused into a single mode fiber using a combination of lenses. The output from the fiber is illuminated on a single diode detector. The reference beam has similar 1mW power as for the particle signal on the detector, is illuminated on another detector. Data from both single-diode detectors is recorded on oscilloscope and subtraction is done computationally using MATLAB.

Experimentally, fiber output is connected to a power meter to check how much light is passing. When SFWP is brought in to the beam path using linear stage, modes start to flip, and transmission efficiency starts to drop. Based on this, mode suppression of more than 99.95 % is achieved. For example, for 100 mW scattered light on the waveplate, light with an intensity lower than 50 μW is transmitted through the fiber at full suppression. However, in practice, 50 μW is not enough to overcome the electronic noise of the detectors. Therefore, the waveplate is slightly displaced to pass through some amount of the Gaussian modes which acts as a local oscillator to enhance the particle signal that is

coupling into the fiber.

4.2.2 Comparison of D-mirror and split-flipped waveplate detection schemes

Based on this scheme, the particle is optically trapped, and simultaneous measurements of positions of the particle are made using both detection schemes. Data is sequentially acquired for both schemes, and the power spectrum is analyzed to observe the trapped and Brownian motion of the particle. For the D-shape mirror based balanced detection schemes, maximum 0.5 mW of power is illuminated on D-shape mirror and balanced detector, while for SFWP scheme, up to 160 mW is passed through SFWP, but only 1 mW is illuminated on single diode photodetector which is enough to acquire all the particle position information in 160 mW of transmitted power. In our OT, $\sim$ 500 mW of power is going into the microscope, and only 160 mW is coming out due to transmission losses into the objective and sample.

The position of a trapped particle is tracked, and similar trap stiffness/corner frequency was found with both techniques when measured without the high-pass filter. As shown in the power spectra in figure 4.2.2, the motion of the particle is constrained by the optical trap at lower frequencies $< f_c$ and at a higher frequency, the amplitude of power spectrum rolls off with $1/f^2$ and/or $1/f^{3.5}$ until it is limited by the laser or digitization noise of the oscilloscope.

In these measurements, the corner frequency is around 5.25 kHz and means that both detection schemes are recording the Brownian motion of the optically trapped particle. The high trap stiffness retains higher position amplitude for longer time which saturates the detector quickly, and we do not have the higher dynamic range to acquire data. Additionally, powerspectrum of the waveplate detection scheme seems to deviate from the flat behaviour slightly. This is because mode suppression at 160 mW scattered power on the waveplate is more sensitive to mechanical and echo vibration in the room, than 500 μW scattered power on the D-mirror. The noise at low-frequency region seems to be increasing with noise in the experimental room.

The particle Brownian motion intersects with a noise floor at $\sim$ 1 MHz, and displacement of the particle at higher frequencies are not accessible. For this reason, we have used 100 kHz high pass filter so that higher voltage amplitudes at lower frequencies are suppressed, and we have the more dynamic range to acquire the signal at frequencies higher than 1 MHz. Moreover, 32 MHz low-pass filter is also used to avoid aliasing of high-frequency noises in the low frequency where the motion of the particle is dominant.

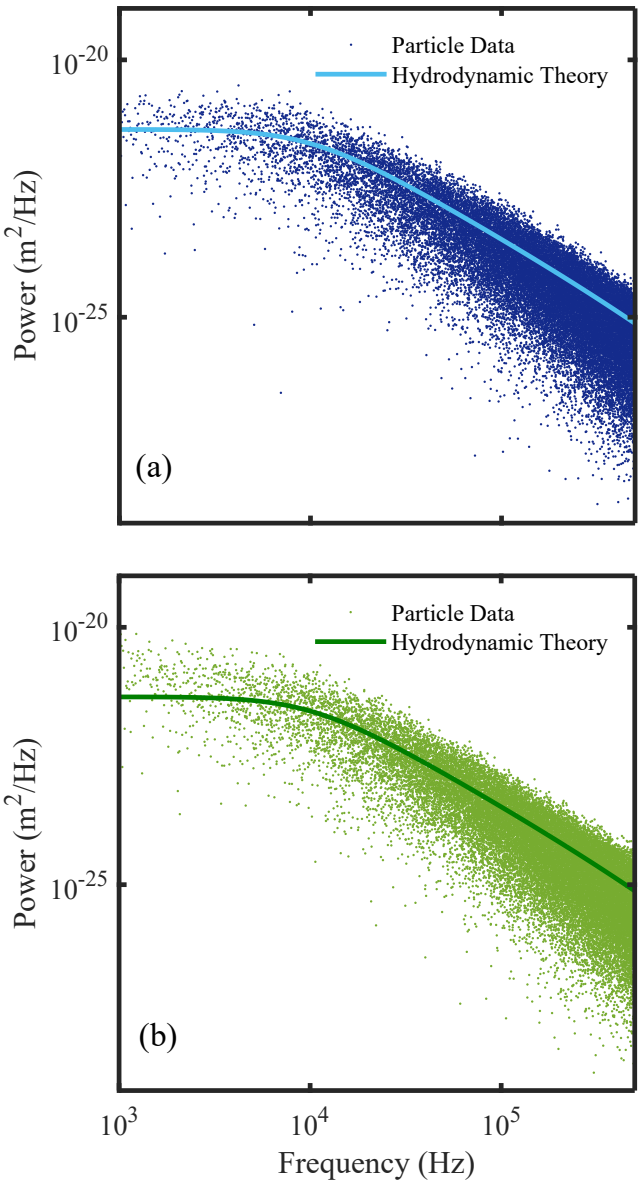

Figure 4.7: **Power spectra of trapped particle using both D-mirror and waveplate based detection schemes.** (a) and (b) are the power spectra acquired using D-mirror and split-flipped waveplate based detection schemes respectively. Trap corner frequency was acquired 5.45 $\pm$0.37 kHz and 5.25$\pm$0.23 kHz respectively. SFWP based detection method is more sensitive to mechanical vibrations of the optical setup, therefore, power spectrum in (b) has non-flat response at lower frequencies.

Based on this, reference and particle signals are acquired from separate detectors using the oscilloscope, and computational subtraction of the reference signal is done from the particle signal. Figures 4.8 and 4.9 show the reference, particle and subtracted signal for 20 mW and 160 mW power on waveplate. This subtraction is necessary to minimize the classical laser noise shoulder from the particle signal at lower frequencies. In our measurements, this subtraction reduces classical laser noise

by approximately 20 dB. At higher bandwidth, the contribution of classical laser noise is lesser than at lower bandwidth.

Based on this computational method, power spectra of the trapped particle for different scattered power on the waveplate are shown in figure 4.10. The acquired bandwidth for this power scaling is shown in figure 4.11, and comparison of bandwidth acquired using both detection methods is shown in figure 4.12. In our experiments, we have acquired one- dimensional particle motion, however, three-dimensional particle tracking can also be done using a more complicated optical set-up. As per the basic principle of the SFWP detection technique, it detects the amplitude of the asymmetric mode, which can be both positive and negative and therefore, does not remove the directional information of the particle.

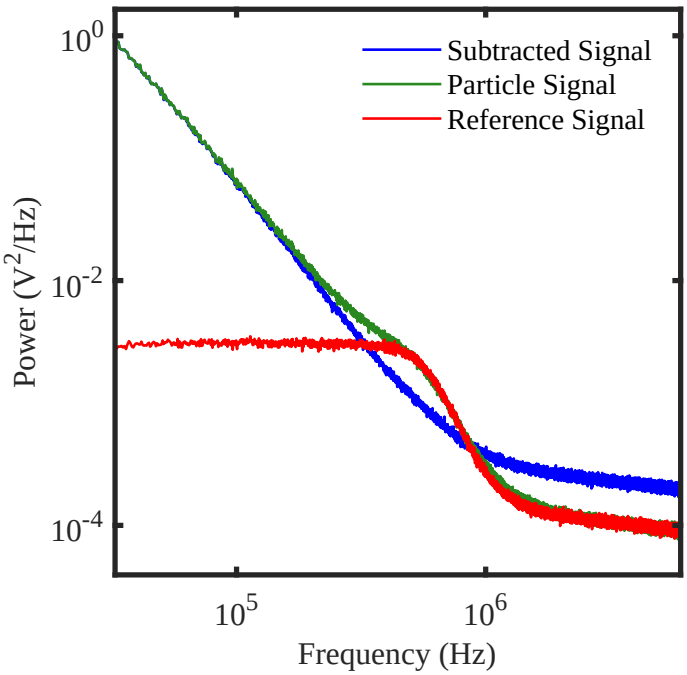

Figure 4.8: **Power spectrum of particle, reference and subtracted signal at 20 mW scattered power on waveplate.** Laser classical noise has a shoulder which has significant contribution in the particle signal. Computational subtraction of reference signal from particle signal minimizes this noise and particle dynamics are acquired.

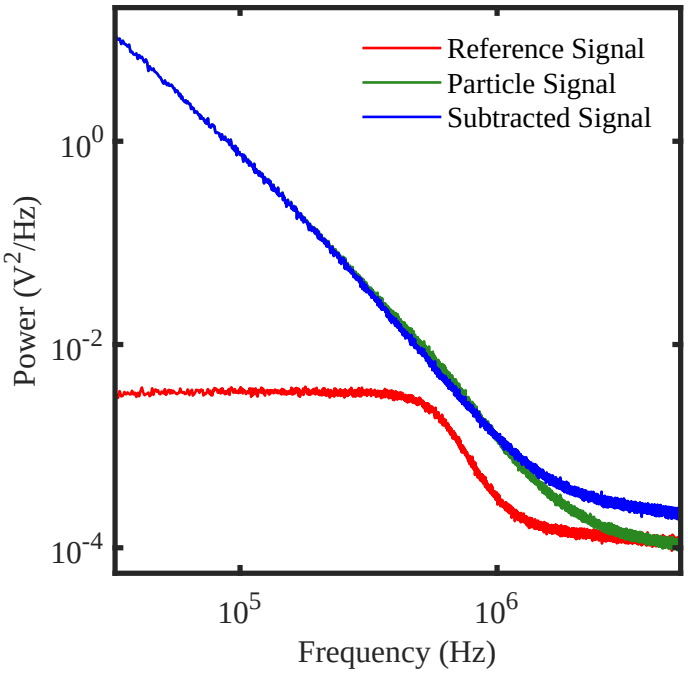

Figure 4.9: **Power spectrum of particle, reference and subtracted signal at 160 mW scattered power on waveplate.** Higher bandwidth is achieved at higher power and laser classical noise has small contribution in the particle signal. This small classical noise is also diminished by computational subtraction of particle and reference signal.

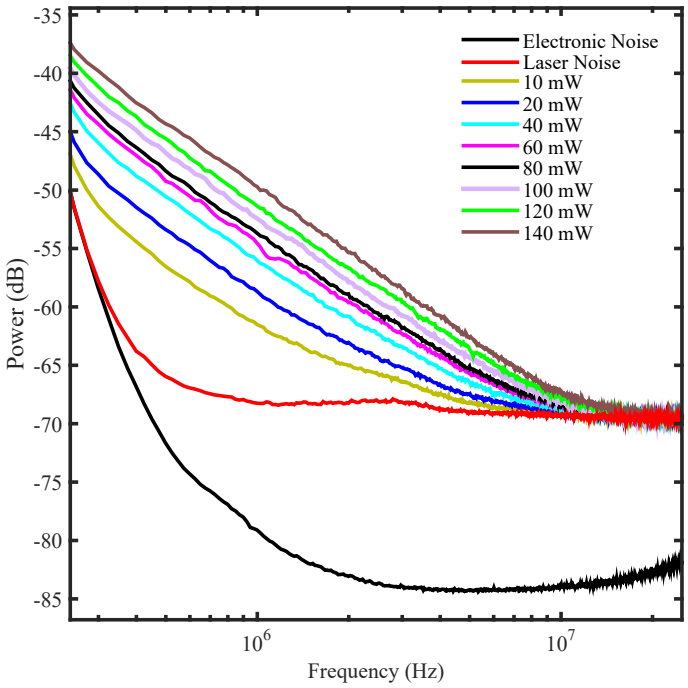

Figure 4.10: **Power spectrum for optical power scaling on the SFWP.** Bandwidth increases with increasing detection power on the waveplate. The little hump on the laser noise is due to the laser relaxation noise.

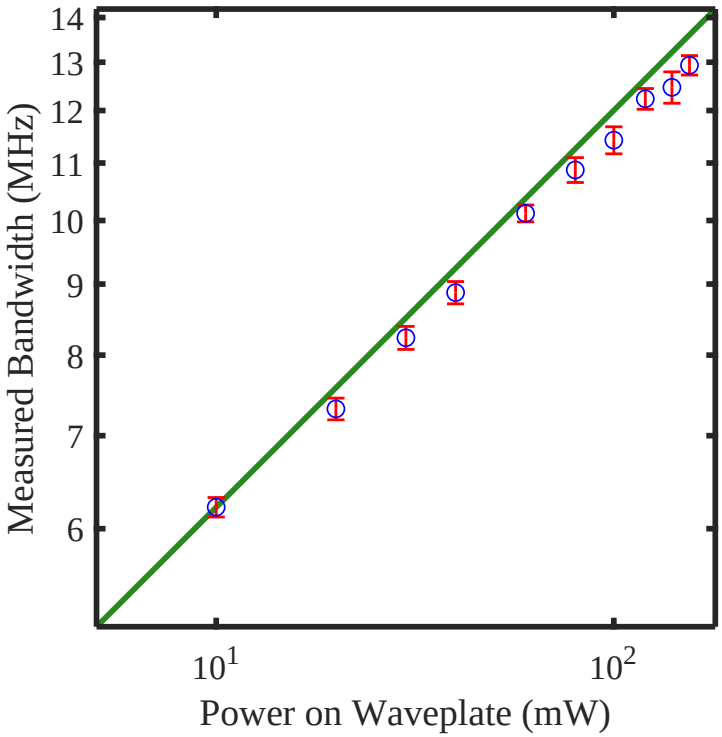

Figure 4.11: **Measured bandwidth of 1 μm for optical power scaling on the SFWP plotted on linear scales.** Circles are the mean bandwidths of three experimental measurement for a particle and error bars are calculated from . The first point is 6.13 MHz at 10 mW power which in the ballistic region and it scales with root power 3.5 for increasing power. The measured bandwidth is lower at higher power as it becomes difficult to acquire $>$ 99.95 % mode suppression with increasing power.

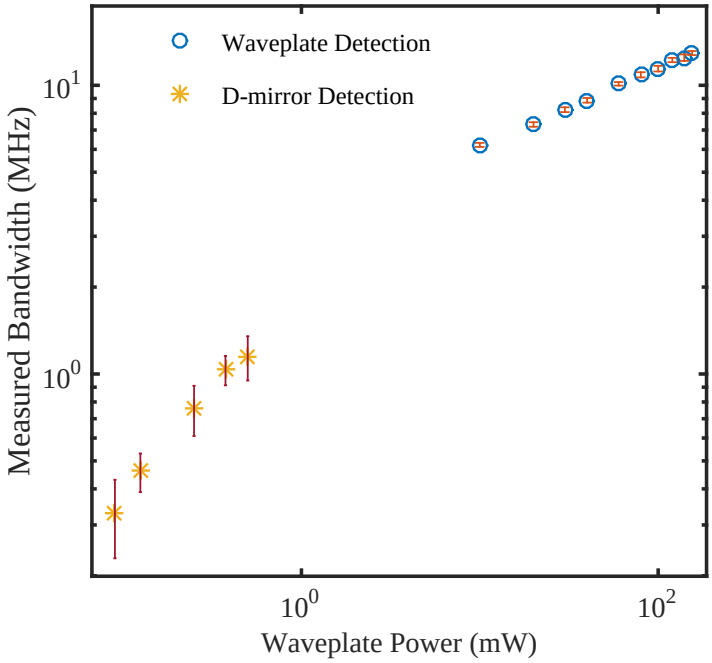

Figure 4.12: Bandwidth comparison of the D-mirror and the SFWP detection schemes plotted on logarithmic scales. Stars and circles are the mean bandwidths of three experimental measurements for a particle and error bars are calculated from standard error. The D-mirror detection scheme saturates at 0.5 mW of scattered power and bandwidth is limited to 1.36 $\pm$0.51 MHz. For the SFWP detection scheme, 160 mW of the scattered power is measured and bandwidth of $\sim$ 10.75$\pm$ 0.46 MHz is measured.

4.3 Ballistic motion of the Brownian particles

According to definitions of ballistic motion mentioned in ref. [70,71], particle motion is called ballistic when MSD is proportional to t_2. For 1 μm silica particle, motion starts to become proportional at timescales shorter than 0.1 $\tau_{p,e}$. Using larger sized particle and lower viscosity medium, this requirement to approach ballistic regime is relaxed. Therefore, it is easier to measure the ballistic motion of a larger sized particle in lower viscosity medium such as acetone. Additionally, at timescales $\tau_{p,e}$ in the region where the transition from free diffusive to ballistic happens, particle undergoes hydrodynamic effects which extend the region of particle transition from free diffusive to ballistic. In our results, we have measured particle motion at timescale close to $0.18\tau_{p,e}$ which means that we are close to measuring the ballistic motion of the particle, yet haven't the region where MSD is proportional to t^2.

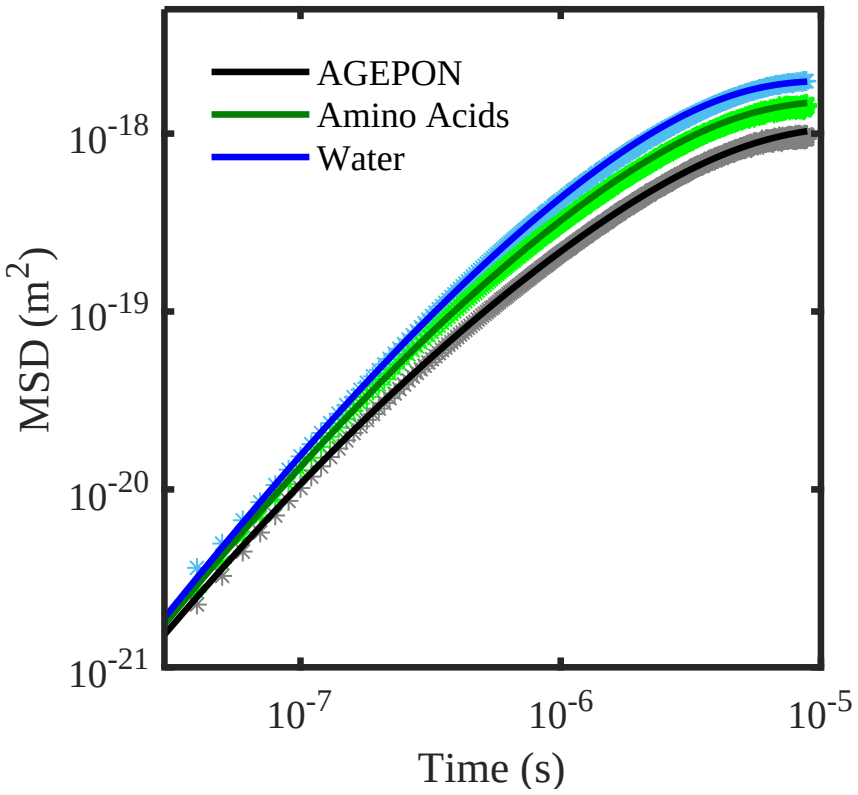

Figure 4.13: **MSD of 1 μm particle in different fluids.** Motion of the particle has been measured at timescales shorter than τ_p. Least-square curve fit of data has been fitted with hydrodynamic theory with roots of the equation 2.36 as fitting parameter.

Figure. 4.13 shows the MSD of 1 μm silica particles measured using the SFWP based detection scheme. The minimum time for which the minimum displacement of the particle is measured can define the temporal and spatial resolutions of our system which are 9.08 ns and 0.35 $\AA$ respectively. The acquired temporal resolution is $0.18\tau_p$ which means that we are close to the ballistic regime. As mentioned in the previous section, we have used an electronic high pass filter due to limitations of measurement bandwidth of oscilloscope, its effect in MSD appears similar to trap corner at the cut-off frequency and at longer timescales. For the data in the figure 4.13, the cut-off frequency of 45 kHz fitted the MSD at longer timescales.

4.4 Particle instantaneous velocity and fluid viscosity measurement

When the particle is measured in the ballistic regime, then its inertia is no longer negligible and instantaneous velocity can be determined by measuring the change in displacement measured over

specific interval i.e. $v = \Delta x/\Delta t$ where Δx is the measured displacement in time Δt. In the ballistic region, velocity is highly correlated and this correlation increases with increasing the measurement bandwidth as given by Eq. 2.3.3 in chapter 2. Experimentally, the instantaneous velocity is affected by the presence of electronic or laser noise at a higher frequency, but with sufficient averaging of successive position measurement, velocity can be extracted reliably [71, 72]. In our experimental data, 5 successive position data points are averaged and the velocity is acquired by $v = \Delta x_{avg}/\Delta t_{avg}$ and then its numerical correlation C_v is computed as shown in figure.4.14.

To measure the instantaneous velocity with 10% uncertainty, the required temporal resolution of the detection system should be better than $\Delta t = \tau_{p,e}/10$ where $\tau_{p,e} = m_e/6\pi\eta r$ is the effective momentum relaxation time calculated with effective mass m_e. The average displacement of the particle during this time Δt is equal to $\tau_{p,e}v_{rms}/10$. Therefore, the displacement uncertainty of the measurement system should be better than $\Delta x = \tau_{p,e}v_{rms}/100$. In the case of 1 μ m silica particle in water, required temporal and spatial resolutions are 0.14 ns and 2.45 pm while the required sensitivity is 0.28 fm/$\sqrt{Hz}$. These calculations show that measurement sensitivity requirements are relaxed for larger sized particles, and instantaneous velocity can be measured at relatively lower bandwidth. The accuracy of the measured velocity can be quantified by how well the measured velocity approaches the thermal velocity $v^e_{rms} = \sqrt{k_B T/m_e}$. The standard error in the velocity measurement can be found by taking repetitive measurements, calculating average histogram and then dividing the standard deviation of each velocity point by square root of the number of measurements for each point.

As we have used a high pass filter due to the limitation of the available bandwidth of the oscilloscope, it is mandatory to incorporate the filter effects in the theory so that experimental data can be fitted with the theory to extract unknown parameters. To do this, we recorded a white noise spectrum from the function generator including the high-pass filter. From the white noise spectrum, the filter function and cut-off frequency is found and are included in the theoretical hydrodynamic simulation of the particle to use it for analysis for experimental data.

Then the velocity correlation of the experimental data is found, and it fitted with the theory which includes this filter effect. The figure 4.14 shows the velocity correlation of $1\mu m$ particle in different fluids. The amplitude of the correlation shows that we have measured the instantaneous velocity of 1 μm particle with high correlation in three different fluids: pure water, 20% v/v AGEPON (AgfaPHOTO) solution in water, and 0.1 mg/ml L-tyrosine (T3754 SIGMA-ALDRICH) amino acid solution in water.

As these experiments give access to the velocity of the particles with correlation C_v given by Eq.

2.3.3, the velocity damping which is the viscosity of the fluid, is directly accessible. As a proof of principle demonstration, we have measured the viscosity in 3 fluids. These measurements are done by tracking 1 μm particle at timescales shorter than 1 μs where biological activities in the cell do not influence the Brownian motion of the particle, and hence, the trapped particle can be used as a probe for viscosity measurement. These fast measurements make our OT biologically compatible as we are using small sized 1 μm silica particle which is relatively easy to trap other higher refractive index Barium titanate, gold or polystyrene particles.

Experimentally, 5 points from 100 million samples of the position data for each fluid were binned and differentiated to obtain the velocity. The correlation function of the velocity was then calculated. Theory curves including the high-pass filter were then fitted by least-square curve fitting using the volt to meter conversion and viscosity as free parameters. The results are shown in figure 4.14. We see that we get distinct traces for each fluid and the fitted viscosity are 0.97, 1.79 and 2.49 $\mu m^2/s$ for water, amino acids and AGEPON solutions. Figure 4.14 shows our preliminary results of the C_v of 1 μm particle measured in different solutions. For these three solutions, a clear difference in the C_v can be seen. Marker points show that experimentally measured data and lines are the C_v from theoretically simulated particle position including hydrodynamic and high pass filter effects.

Velocity autocorrelation does not explicitly give the measurement of instantaneous velocity; rather it tells how much average velocity points are correlated to each other. To measure velocity with 10%uncertainty, required δt can be estimated by measuring the time interval on autocorrelation graph for 10% change in the velocity correlation region where correlation changes fast. It is 2 ns for 1 μm silica particle. During this time interval, the particle displacement is 3.53 pm, and position uncertainty will be 0.35 pm. Based on this, our achieved spatial and temporal resolution of 0.35 A and 9.09 ns are close to measuring the instantaneous velocity in the ballistic regime.

The theoretically simulated C_v governs identical correlation as given by Eq. 2.3.3 in chapter 2 and therefore, can be matched to the experimental data with C_v amplitude and fluid viscosity as free parameters. In the figure 4.14, the viscosity of the fluids is independent of the amplitude of C_v and governs same viscosity result for the different amplitude of C_v. This means that viscosity measurement is calibration free, and we do not need to do volts-to-meter conversion to find viscosity of the fluid. Additionally, Using C_v of the particle has the advantage that its velocity timescales are far from the biological activities primarily in the cell and can be used as a probe for microrheology measurements.

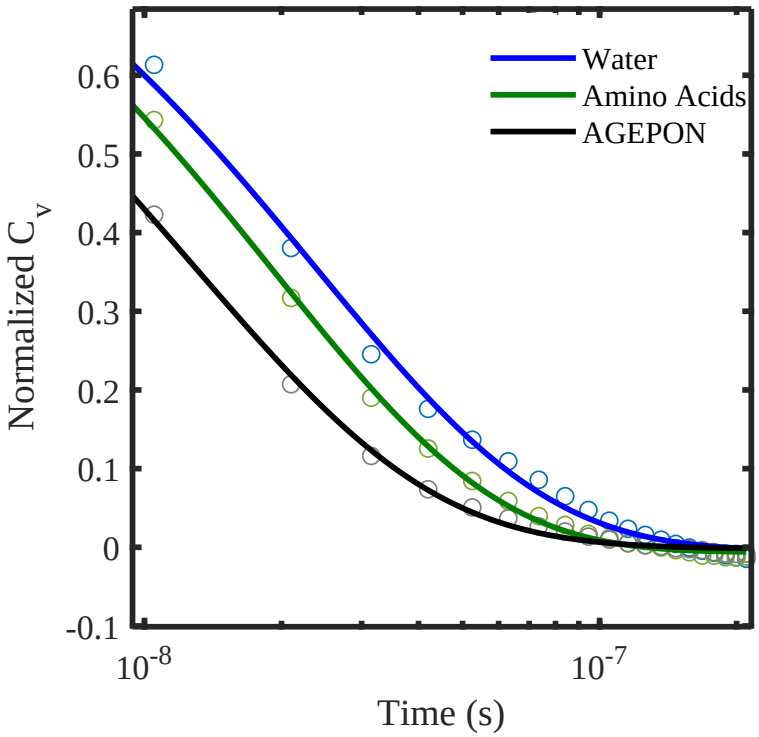

Figure 4.14: **Semilogarithmic plot of velocity Correlation Function of 1 μm particle in pure water, 20% v/v AGEPON solution and 0.1 mg/ml L-tyrosine amino acids.** Marker points shows that experimentally measured data and lines are the C_v with viscosity and volts-to-meter conversion factor as the fitting parameters.

4.5 Conclusions

We have described a new particle tracking scheme in optical tweezers based on split flipped waveplate which filters the even modes of the scattered field and detects the odd modes which have information about the displacement of the particle and enables to extract the information at very high powers. This technique has enabled us to measure the motion of 1 μm silica particle at an unprecedented $\sim 10.75\pm$ 0.46 MHz bandwidth. On the contrary to the D-mirror based detection scheme which saturates at a few mW optical power, it has enabled us to measure 160 mW of scattered light collected from the condenser and extracting position information of the particle. If we have access to high-power laser and high transmission objectives, this technique can measure even higher power and hence increased measurement bandwidth.

The mean squared displacement of the particle shows that we have observed the free diffusive motion, hydrodynamic effects and most importantly, the ballistic motion of the particle. The instantaneous

velocity of the particle is measured, and its correlation function is used to determine the ultra-fast viscosity measurement in pure water, 20% v/v AGEPON solution and 0.1 mg/ml L-tyrosine amino acids. By using high transmission objectives, it is possible to measure even higher optical power which would give even higher bandwidth and acquiring C_v at even shorter timescales. This high bandwidth and ultra-fast optical tweezers will be very helpful to test the Maxwell-Boltzmann distribution and viscosity measurement in a relatively complex environment such as a biological cell.

Chapter 5

Ultra-stiff optical tweezers

5.1 Overview

In this chapter, a new type of interferometric-based phenomenon is demonstrated in which a particle can be made to behave as a beam-splitter when phase structured light is incident on the dielectric particle. On contrary to the standard deflection based optical force exertion phenomenon, this new type of interferometric enhanced optical trapping technique produces constructive and destructive interference of the incident light field over the wide range of angles around the optical axis which can enhance the trap stiffness by several orders of magnitude for the particles in Mie regime. This chapter is based on the following publication:-

Michael A. Taylor, Muhammad Waleed, Alexander B. Stilgoe, Halina Rubinsztein-Dunlop and Warwick P. Bowen, "Enhanced Optical Trapping via Structured Scattering", Nature Photonics 9, 669–673 (2015) [1].

5.2 Introduction

In standard optical tweezers (OT), optical forces are exerted on a dielectric particle when propagation direction of the incident light field is altered by the particle due to refraction at the surface of the particle. Due to redistribution of incident light by the spherical particle, it experiences a restoring force towards the focus of the field, remains trapped until some other external forces tend to dominate. This trapping phenomenon is based on the deflection of incident light by the dielectric particle in which light is deflected at displacement dependent angles which also governs the position of a particle in the optical trap. However, for the Gaussian distributed intensity pattern, the trap stiffness can only

be increased by increasing the incident optical field intensity. Increasing optical intensity is highly unsuitable for a wide range of applications especially in biology where damage due to localized heating effects is quite cumbersome and also changes the dynamics of system.

The trap stiffness is maximum only for the particle sizes comparable to the incident laser beam wavelength and loses stiffness with increasing diameter (see fig. 2.4 of chapter 2). Consequently, few experiments have explored trapping with larger diameter particles. Although most of the biophysics experiments employ smaller sized particles, the regime of the larger sized particle is less explored, however, there are several areas of studies in which larger particles or objects are of considerable importance. For instance, light-driven micro-robots which provide targeted delivery of drugs, are being developed in which few micrometer sized glass syringe is manipulated by trapping the spherical particles attached to the syringe [124]. Similarly, microgears and rods which act as either active or passive handles in making micro-robots, are usually manipulated using optical forces [77, 78]. Moreover, infrared laser beams are transparent or non-invasive to biological samples at lower power, it has been used to trap the red-blood cells in vivo which are larger than λ, to clear the blocked micro-vessels [79] and also for diseases identification [80, 81].

Similarly, biological cell sorting and manipulation are often done with OT where larger sized cell, typically greater than 10 μm, are displaced [82,83]. In addition, optical trapping forces are used to trigger vestibular behavior on 55 μm sized otoliths where very high powers ranging from $50 \sim 600\ mW$ were illuminated on zebrafish [84]. Furthermore, optical levitation of several micron-sized particles in vacuum has also been used to better understand the particle physics and gravitational forces [17, 18, 85]. From these examples, it is clear that trapping of larger particles is very crucial in many biological and engineering applications and also for understanding a wider range of fundamental science, therefore, new tools to trap larger particles or enhance the trap stiffness are vital.

Performance of the optical trap is usually determined by the optical trap stiffness which depends upon several parameters such as optical scattering, extinction and absorption cross-section and, can be improved using several techniques either by structuring the incident beam profile or by altering the physical properties of the trapped particle. For instance, a slight improvement in the optical trap stiffness has been demonstrated for counter-propagating trapping beams in which scattering forces is minimized resulting in the increased gradient force [86, 125–127]. Secondly, several studies based on the structured light fields have been demonstrated to improve the axial or lateral trap stiffness by maximum 1.6 times than that for a simple Gaussian trap [87–89]. The state-of-the-art in stiffness has been increased by a factor of 2 by employing specially engineered high refractive index and anti-

reflection coated Titania particles to suppress the back-scattered light. The coating ensures stable trapping, while the high refractive index core allows very strong interaction with the trapping field. While the back-scatter of such particles is suppressed, they exhibit forward-scatter with a similar angular distribution to homogeneous spheres, but with far stronger scattered fields [90].

As mentioned in chapter 2, dipole approximation and ray optics models are for the particles sizes much smaller and greater than λ and for particle size close to λ, the extended Mie or Lorenz-Mie theory is used for full description of electromagnetic field, although it also governs correct solutions for particle sizes in ray-optics regime. In all the above-mentioned techniques, the deflection of light incident light happens which governs a measure of the trap stiffness.

In this work, we demonstrate a new type of light-particle interaction in which it is shown that spatial structure of light in Mie scattering can be altered to create and enhance the interference fringes. In this way, instead, particle being deflecting the incident light, it creates an interference pattern in the scattered field. It means that the structured incident light can make spherical particles behave like a beam-splitter which separate a phase-structured input field into distinct output fringes. The Mie scattering of low contrast microparticles separates the light from each incident angle into a collection of scattering fringes. These fringes combine the fields from a range of incident angles and therefore allow the particle to act as an effective beam-splitter between different incident angles which enhances the optical trap stiffness by orders of magnitude than a simple Gaussian trap.

5.3 Upper limit on optical trap stiffness

Light consists of tiny energy packets photon whose energy is given by $U = hc/\lambda$ where λ is the light wavelength, h is the Plank constant and c is the speed of light in vacuum, and momentum $p = h/\lambda\hat{r}$, where $\hat{r}$ is a unit vector describing the direction of motion of photon. When a photon is elastically scattered by an object, no change occurs in its energy rather a change in momentum happens which applied a recoil force on the object. The magnitude of the optical forces fundamentally depends upon the momentum flux transferred per unit area and is given by $n_m P/c$, where n_m is the refractive index of the surrounding medium, c is the speed of light and P are the incident optical power [128].

When light-matter interaction occurs, all the momentum is not transferred to the object instead a fraction of the momentum is transferred which is generally described by a normalized force quality factor Q (see chapter 2). In case of complete reflection of light in which a propulsion force is applied by the light on the mirror in the direction of propagation of light, the applied force F is equal to $2n_m P/c\hat{r}$ and the quality factor Q has a maximum value of 2. For trapping application, light is not

completely reflected rather it is deflected and stable optical trapping is achieved when the range of applicable forces is powerspectra about zero.

$$x = -\frac{F}{\kappa}. \tag{5.1}$$

where κ is the optical trap stiffness. If measured force uncertainty is δF then the associated measurement uncertainty is then given by:-

$$\delta x = \frac{\delta F}{\kappa}, \tag{5.2}$$

Consequently, the largest achievable trap stiffness $kappa_{\max}$ is constrained by the quantum limits to both position sensitivity and optical force noise, with

$$\kappa_{\max} = \frac{\delta F_{\max}}{\delta x_{\min}}. \tag{5.3}$$

In the case of ideal detection with perfect coherent light, the optical force noise is limited by radiation pressure shot noise given by

$$\delta F_{\max} = (n_m h/\lambda)\sqrt{N} \tag{5.4}$$

where $N = \frac{P\lambda}{hc}t$ is the number of photons included in the measurement time t, and h is Plank's constant. In this case, the standard lower limit to measurement precision is given by [129].

$$\delta x_{\min} = \frac{\lambda}{4\pi n_m \sqrt{N}}, \tag{5.5}$$

Substituting these into Eq. 5.3, the upper limit to trap stiffness is given by

$$\kappa_{\max} = \frac{4\pi n_m^2 hN}{\lambda^2} = \frac{4\pi n_m^2 P}{c\lambda}, \tag{5.6}$$

where $P = Nhc/\lambda$. in principle, this trap stiffness $\kappa_{\max}$ corresponds to the highest stiffness which is achievable for classical far-field optics. Trap stiffness basically depends upon the minimum resolvable distance $\delta x_{\min}$which could possibly be minimized further using non-classical states of light resulting a measurable increase in the trap stiffness.

5.4 Spherical particle as a beam-splitter

In the present work, particles having a size greater than λ are used and the light scattering profile from the particle is described using Mie scattering theory. For a near-collimated incident Gaussian beam, the Mie scattering profile comprises concentric rings of positive and negative scattering amplitude. If the light is incident over a broader angular range, the collective scattering can be described by combining the Mie scattering from each individual incident angle. In this case, the Gaussian illumination is homogeneous over a broad angular range such that the neighbouring positive and negative scattering fringes overlap and are suppressed via interference. As a consequence, Mie scattering fringes can usually be ignored in optical traps [130].

However, by using a highly structured illumination, it is possible to strengthen these fringes with constructive interference between the Mie scattering from different incident angles. The structured optical field can populate the fringes with fields having near-orthogonal phase, such that any small phase shift can lead to constructive or destructive interference; and similar to the beam-splitter analogy, particle transforms the field into well-separated output fringes which leads to a higher trapping force. Even small particle displacements can alter the phase completely, governing a stable optical trap. This new beam-splitter-like optical trapping can be termed as 'enhanced trapping via structured scattering (ENTRAPS)'. The schematic of this concept is shown in the figure 5.1.

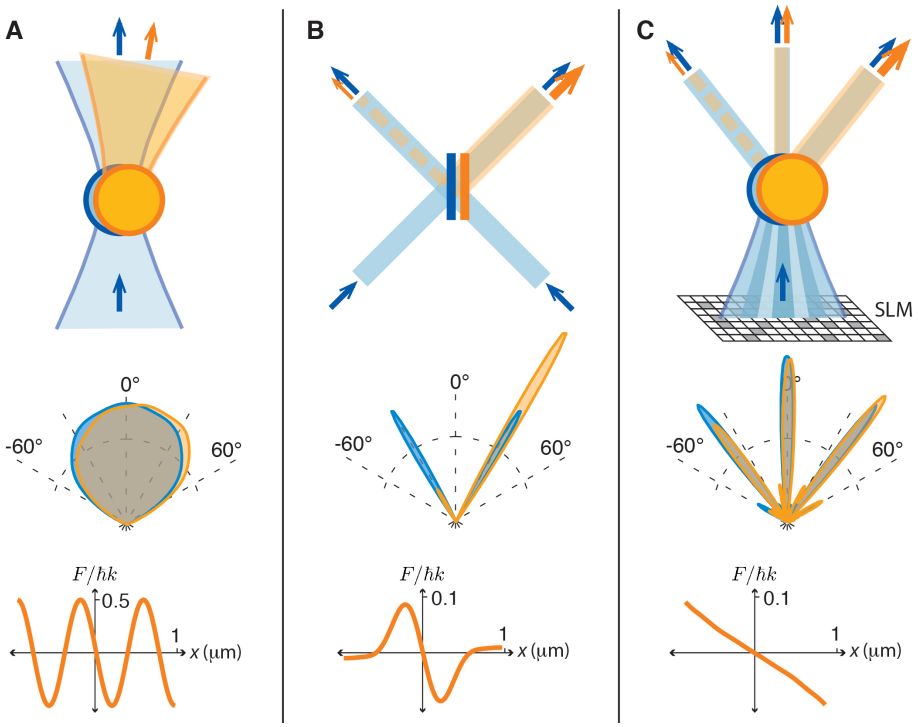

Figure 5.1: **Schematic of trapping via Mie interference.** **(a)** shows the deflection of light from spherical particle, the calculated polar plot of the transmitted intensity with fields and particles shown in blue for a centered particle and orange for a displaced particle and force vs displacement curve for the particle. **(b)** similar things for planar beam-splitter and and (**c**) shows that structured incident light on the particle can govern structured scattering similar to beam-splitter. Figure 5.1 is taken from ref. [1]

Optical traps function by redirecting light as the trapped particle moves. In typical optical traps this is achieved via deflection of the incident field, as shown in **(a)** both schematically and with a calculated polar plot of transmitted intensity. When the particle is displaced, the transverse momentum of the light (as plotted in the lowest panel) is changed thus inducing an optical force. Trapping can also be achieved via interferometry at a beam-splitter as shown in **(b)**. Here, the motion of the beam-splitter causes relative phase shifts that reroute light between the outputs without deflecting them. This achieves far stiffer trapping forces though with a far smaller trapping range. ENTRAPS achieve a similar force using a scattering microparticle instead of a planar beam-splitter. For a trapped particle via beam-splitter phenomenon, a structured trapping field is split into distinct scattering fringes via Mie scattering, with particle position the power in each fringe, rather than the propagation direction, dependent on particle position as shown in (**c**).

5.5 Optical force on a beam-splitter

When two fields are incident on a beam-splitter, the intensity at the two outputs is determined by their relative phase ϕ. Since the two output fields propagate in different directions, any imbalance in the powers leads to an optical force on the beam-splitter. The mean difference in the output powers is given by:-

$$\langle \Delta P \rangle = P \sin(4\pi n_m x/\lambda) \tag{5.7}$$

with a resulting optical force of

$$F = -\frac{n_m P}{c} \sin\theta \cos\phi \tag{5.8}$$

with c the speed of light and θ the incident angle on the beam-splitter. Lateral movement of the beam-splitter by a distance x causes the relative phase between the input fields to change by $\Delta\phi = 4\pi n_m (x/\lambda) \sin\theta$. By examining Eq. (5.8) one can see that this phase shift will change the force on beam-splitter, and that if the phase is set to $\phi = \pi/2$, the force achieves a stable trap of the form $F = -\kappa x$. For normally incident light ($\theta = \pi/2$), the trap stiffness reaches:

$$\kappa_{\max} = \frac{4\pi n_m^2 P}{c\lambda} \tag{5.9}$$

This represents the upper limit on the achievable stiffness for beam-splitter phenomenon based optical trapping and corresponds exactly to the maximum trap stiffness achieved in deflection based optical trapping [131]. Consequently, the trap stiffness derived for this system corresponds to the highest stiffness which is achievable for propagating coherent light.

5.6 Modeling of electromagnetic field using Mie theory

The scattering of light can be thought as the redirection of light that takes place when an electromagnetic (EM) wave is incident on a homogeneous material such as a scattering particle in this case. As described in chapter 2, the electromagnetic field modeling using extended Mie theory can be used to accurately describe the scattered electric field in terms of the far-field angular profile which can fully describe the electric field at every point in the space, with the assumption of isotropic homogeneous particles and plane wave illumination [132]. In this framework, the electromagnetic field can

be decomposed into orthogonal vector spherical harmonic functions VSWFs Φ and Ψ

$$E(\theta,\phi)^{inc} = \sum_{n=0}^{\infty}\sum_{m=-n}^{n} a_{n,\,m}\Phi_{n,\,m}(\theta,\phi) + b_{n,\,m}\Psi_{n,\,m}(\theta,\phi), \tag{5.10}$$

where a and b are the beam shaping coefficients for incident wave VSWFs and, n and m are the principal and azimuthal mode indices which describe integer orbital and angular momentum respectively. Representation of a three-dimensional vector field strictly requires three separate vector functions; however, these functions are defined in the far-field where the radial polarization component is assumed to be zero. Each of the VSWFs is an eigenmode of the scattering interaction when the light is incident on a homogeneous spherical particle which is powerspectra at the origin and this scattered field can be written as

$$E(\theta,\phi)^{scat} = \sum_{n=0}^{\infty}\sum_{m=-n}^{n} p_{n,\,m}\Phi_{n,\,m}(\theta,\phi) + q_{n,\,m}\Psi_{n,\,m}(\theta,\phi) \tag{5.11}$$

where p and q are the beam shaping coefficients for scattered field VSWFs Φ and Ψ and these coefficients can be connected to each other via a multiplicative matrix which is generally called as T-matrix T. This matrix is basically a description of the scattering properties of a particle where the incident and scattered fields can be expanded in series of discrete basis functions.

$$\begin{pmatrix} p \\ q \end{pmatrix} = T \times \begin{pmatrix} a \\ b \end{pmatrix}. \tag{5.12}$$

The T-matrix completely describes the scattering process and can transform between arbitrary input and output fields. When the incident and scattered fields are modelled for a given system, the applied optical radiation pressure force F_{RP} can be determined by calculating the change in momentum of the field as follows

$$F_{RP} = \varepsilon/2 \int |E(\theta,\phi)|^2 \,\hat{u}\, dA, \tag{5.13}$$

where ε is the material permittivity, $\hat{u}$ is the normal unit vector and dA is the area element calculated in the direction (θ,ϕ). This calculation forms the basis of calculations presented here, with the implementation relying on functions from the OT Computational Toolbox (OTT) [99]. In this framework, the number of modes n and m with which a spherical particle of radius r will interact strongly, is given approximately by $(kr)^2$ in the limit that $r \gg \lambda$. For a Gaussian beam optical trap, the beam

has homogeneous intensity profile over wide angles, the first order modes are dominant in Rayleigh regime and higher trap stiffness is achieved for particle size close to the wavelength as shown in figure 2.4 of chapter 2.

However, for larger particles, scattered light is populated into higher order VSWFs modes which have qualitatively different spatial structure, with both positive and negative amplitudes at different angular positions. This allows the interference to have a non-trivial spatial structure that is not possible for n = 1 modes and consequently allows new characteristics in the applied optical force. For 1064 nm wavelength, particles larger than 1800 nm, the first order modes are no longer dominant in the scattering terms in the T-matrix, and the particle interacts more strongly with higher order modes. As the particle size increases, the most strongly scattering VSWFs modes become even higher [99]. For instance, a 10 μm diameter silica particle interacts most strongly with the n = 38 modes.

Therefore, by structuring the incident field, the scattered light can be populated into the strongly interacting higher order modes. However, simply populating light into these modes is not adequate to achieve strong trapping. Strong trapping requires not only strong scattering but also efficient interference between the different modes to maximize the radiation pressure force F. Because the high-order modes exhibit considerable spatial structure, the interference can vary strongly with angular position and, with appropriate structuring, this can be used to achieve well-controlled interference in the output field. This spatial control over the interference pattern is not possible with n = 1 modes, and therefore the resulting force can be engineered with quantitatively different characteristics.

5.7 Algorithm to locally optimize trapping profiles

To calculate the trapping profile for ENTRAPS, we performed an iterative optimization routine to maximize the trap stiffness. In principle, incident beam can be optimized for combined phase, amplitude and polarization. However, demonstrating such control in experiments is technically very difficult, and non-uniform polarization is expected to reduce interference visibility and may not improve trap stiffness. In ENTRAPS, the optical force is based on interferometry, and it is the phase of the light which determines if the interference is constructive or destructive, therefore, interferometry can be performed with phase-only control, though full-wavefront control might give even higher trap stiffness. In the experiment, phase control of the trapping light is straightforward to achieve with a spatial light modulator and is used widely in holographic OT and we find allows orders of magnitude enhancement in the trap stiffness.

The trap stiffness can be efficiently optimized when the particle interacts strongly with a large number

of spatial modes of light, as this allows greater control over the scattering interaction. Larger sized particles can interact with a higher number of optical modes, and consequently, allow greater levels of control over the scattered field. The algorithm is basically based on the calculation of scattered field and radiation pressure force described by the Mie theory which is quite complex. These T-matrix based calculations have been simulated in ref. [99].

As described earlier, an incident field in expanded as the sum of VSWFs whose amplitude is controlled by the beam shape coefficients a and b which are further decomposed into integer angular and orbital momentum mode parameters m and n respectively with a condition that $\mid m \mid \leq n$. The VSWFs can be expanded into infinite sums of mode field amplitudes a and b which is not favourable computationally, therefore, n needs to be truncated at an arbitrary value N_{max} where it should be large enough to be able to describe enough details of the trapping field.

For a specific value of N_{max} , the total number of modes included in the calculation are $4N_{max}+2N_{max}^2$. Based on this simple expression, there are 8710 modes $N_{max} = 65$ and 20400 modes for $N_{max} = 100$. Similar phase profiles for the scattered field are observed for $N_{max} \geq 65$ however, choosing smaller values of N_{max} is lesser computationally expensive. In OTT, the optical field is calculated over an angular grid of points which makes it computationally in-efficient, therefore, it is better to describe them in terms of angular field distribution $E(\theta,\phi)$ at angular co-ordinates θ and ϕ. Two matrices A_p and B_q are introduced which implicitly contain the angular grid and can be used to convert between the bases by simple matrix multiplications which makes computation faster [133].

$$E(\theta,\phi) = A_p \times a + B_q \times b \tag{5.14}$$

$$a = A_p^{tr} \times (E(\theta,\phi) \cdot dA) \tag{5.15}$$

$$b = B_q^{tr} \times (E(\theta,\phi) \cdot dA), \tag{5.16}$$

where the superscript tr indicates a complex transpose. To control the trapping light, an iterative phase optimization routine is performed to maximize the trap stiffness. For this purpose an arbitrary phase (or amplitude) plate with 8000 modes ψ_i is defined, where the spatial frequencies describe the modes decomposition. Here i denotes the mode number, and the phase plate can be fully described by the coefficients c_i of these modes. The phase plate is applied to a Gaussian trapping field in the angular field basis, and the field converted back to the spherical harmonic basis and the resulting force is determined using calculations adapted from the OTT [99], with modifications mentioned above. Then the trap stiffness defines the fitness F_t of the phase plate, which is the variable to be maximized in this algorithm.

To structure the incident field, firstly, change in trap stiffness for small changes in each of the coefficients c_i of the phase plate is calculated. Once this is known, a collective mode Ψ of the phase plate is defined which can most strongly improve fitness, defined as:-

$$\Psi = \sum_i \frac{\delta F_t}{\delta c_i} \psi_i. \tag{5.17}$$

This collective mode is added to the phase plate with varying amplitudes until a local optima in fitness is found. The phase plate is then updated, and the optimization algorithm then repeats as many times as necessary. The phase plate is deformed towards the local minima for each iteration of the algorithm and different optimization solutions are found for different starting values. Therefore, the algorithm does not locate the global optimum for the best achievable trap stiffness, yet governs reasonably close solution.

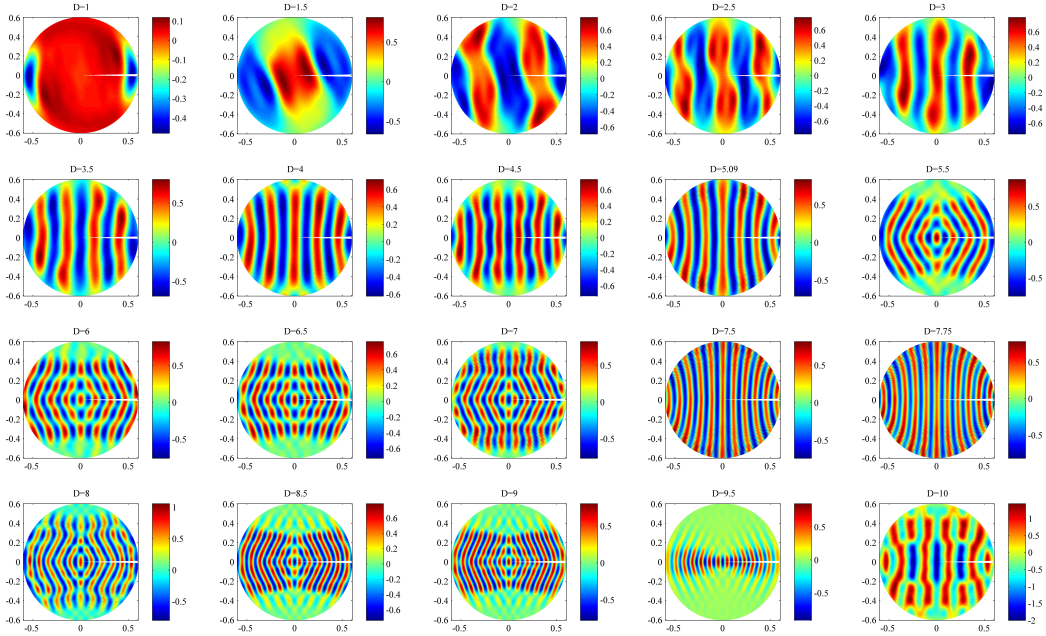

Figure 5.2: **Calculated phase holograms for a range of silica particles that are implemented in experiments using SLM**. The stripy lines are due to the constructive and destructive interference of Mie scattering fringes. As the particle size increases, scattering modes become more complex due to interference. Phase profiles are scaled to the back aperture size of the objective having NA=1.25.

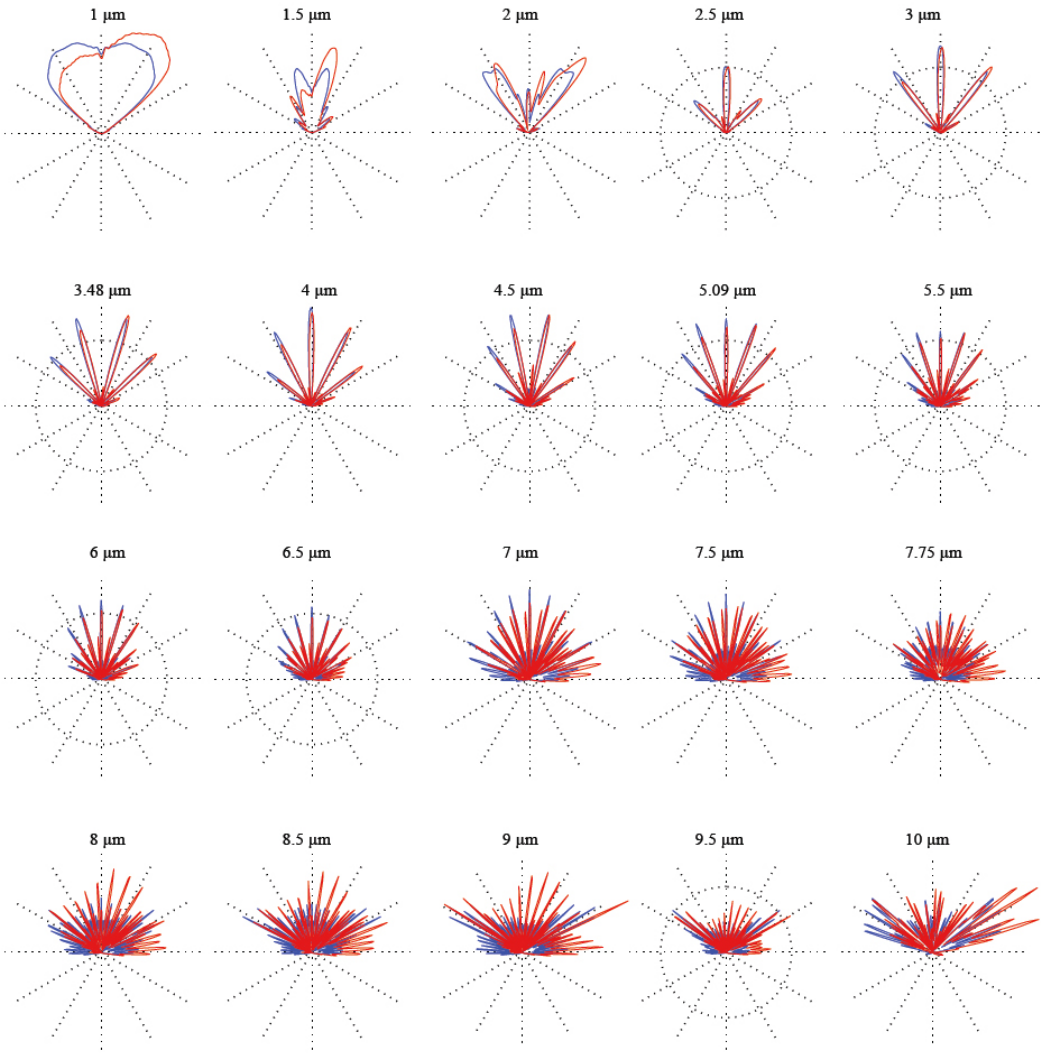

Figure 5.3: **Polar plots of the transmitted intensity at the focal plane when using the calculated holograms for silica particles**. Blue and red curves respectively show the intensity when the particle is power spectra, and displaced 150 nm right. The characteristic beam-splitter-like trapping of ENTRAPS is observed over the entire size range. For 1 μm particles this effect is somewhat weak and provides minimal enhancement. As the size increases, the interference fringes become more well defined and the ENTRAPS effect more pronounced. Further increasing the particle size results in many more fringes, and an increasingly complex transmission pattern. The figure is taken from ref. [1]

This optimization algorithm is not limited to optimizing only phase profile rather it can also be used to full wavefront control with both phase and amplitude structuring for even better trap performance. Amplitude control can be simply included in the above algorithm in the same way as phase control, with an amplitude plate perturbing the default Gaussian intensity profile. To incorporate this, the algorithm can be alternated between optimizing phase and amplitude until both reach a local optimum. It is noted that the Optical Eigenmode method can find the global optimum for the case of amplitude

and phase control [134, 135] which is described in detail in later studies [131]. As the implementing both amplitude and phase structured profile is technically quite challenging, only phase control is demonstrated in the current experiment which still provides significant enhancements in trap performance. Using this method, phase profiles or generally called holograms which optimize the trap stiffness for any particle size can be found.

Figure 5.2 shows the phase profiles for silica particles ranging from 1-10 μm in diameter and this profile is displayed on the SLM to implement ENTRAPS. The stripe patterns in the phase hologram are the Mie scattering interference fringes which are weaker for smaller and stronger for larger sized particles. These phase holograms convert the incident Gaussian beam into a structured beam whose intensity profile about the focal plane is shown in figure 5.3. Again, these fringes are suppressed for smaller sized 1 μm particles and therefore, large fringe patterns are present over the wide angles. As particle size increases, more interference fringes can be incorporated in the particle and fringes becomes more distinct and sharper. This algorithm is written by Michael Taylor in MATLAB , and a later improved version is available online [131].

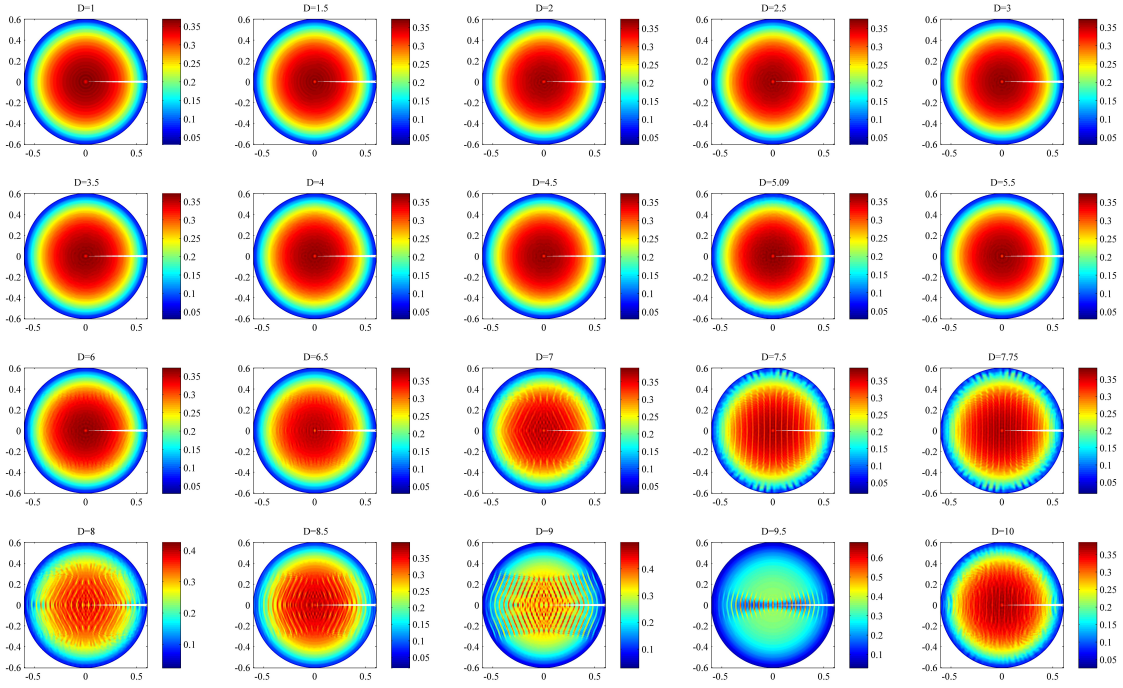

Figure 5.4: **Intensity profiles at the back-focal plane of the trapping objective**. These are calculated for a range of silica particles that are implemented in experiments using SLM and imaged at the back-focal plane of the objective. Intensity profile is Gaussian but after interaction with the particle, light is separated into its discrete fringes in the far field which is measured at the PSD. Intensity profiles are scaled to the back aperture size of the objective having NA=1.25.

5.8 Holographic Optical Tweezers to implement ENTRAPS

To demonstrate ENTRAPS experimentally, a holographic OT setup was employed. Briefly, in holographic OT, a reflective spatial light modulator (SLM) (Holoeye HEO-1080P) is employed which spatially modulates the phase and resulting amplitude of an optical wavefront in two dimensions and is placed on the plane conjugate to the back focal plane of the trapping objective using relay lenses to allow arbitrary phase control of the trapping light. SLM can be programmed to generate light beams with various optical waterfronts and can be used as mirrors, lens, and gratings [136]. However, it is inefficient in terms of modulation power to do simultaneous modulation of phase and amplitude, therefore, SLMs are mostly used only as a phase control devices. To modulate ENTRAPS, home-made programs written in MATLAB are used to map the calculated hologram on the SLM, along with a blazed grating to eliminate zero-order reflections, and an aberration compensation pattern for better implementation of phase profile, which is determined in advance using similar scheme used in ref. [137].

As the hologram phase profile is present in the first-order mode, therefore, a mechanical aperture is used to eliminate all the diffraction modes except the first order which is then directed towards the back-focal plane of an oil-immersion objective , employed for trapping the particles. Calculations of the holograms are done in spherical coordinates (θ, ϕ) while holograms are mapped on the SLM in cylindrical coordinates (ρ, ϕ) which are more convenient to program the SLM. Therefore, it is necessary to map the cylindrical coordinates into spherical coordinates and Abbe's sine condition is used to do this as it describes how the phase pattern propagates from the SLM to the far-field of the particle [138]. When the objective focuses the incoming field, the phase shift on the SLM is mapped to the far-field profile from the objective focus. This maps the SLM coordinates to far-field angular coordinates (θ, ϕ) around the focus. This can be described simply if the SLM coordinates are represented in the polar form (ρ, ϕ). In this case, the mapping preserves ϕ unchanged, while the radial position ρ maps to the angular position θ according to Abbe's sine condition $n_m \sin(\theta) = \rho / C$, where C is the radius of the objective back aperture.

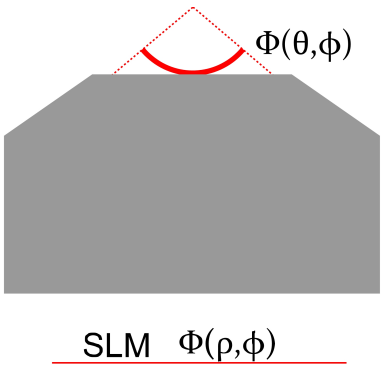

Figure 5.5: **Representation of Abbe's sine condition for this experiment**. The pattern on the SLM applies a phase pattern Φ at the back-focal plane. It is most convenient to use cylindrical coordinates (ρ, ϕ) to represent this. Propagation through the objective then maps this profile to the far-field of a converging spherical wave, which is represented in spherical coordinates (θ, ϕ). The sine condition describes how the phase pattern propagates from the SLM to the far-field of the particle. Figure is taken from ref. [1]

After correctly mapping phase-profile on to the SLM, a sealed sample using two coverglass is prepared in which silica particles float in water and light is then focused on silica particles with high numerical trapping objective. As for a standard single-beam OT, lateral trap stiffness increases with increasing NA [133]. Therefore, higher trap stiffness is expected with this structured illumination because higher order modes which are also spread towards the edges in angular profile can be collected and focused on the particle with higher NA objective which will govern improved coupling of modes and hence higher trap stiffness and accurate scaling of trap stiffness enhancement with trapping objective NA can be studied further.

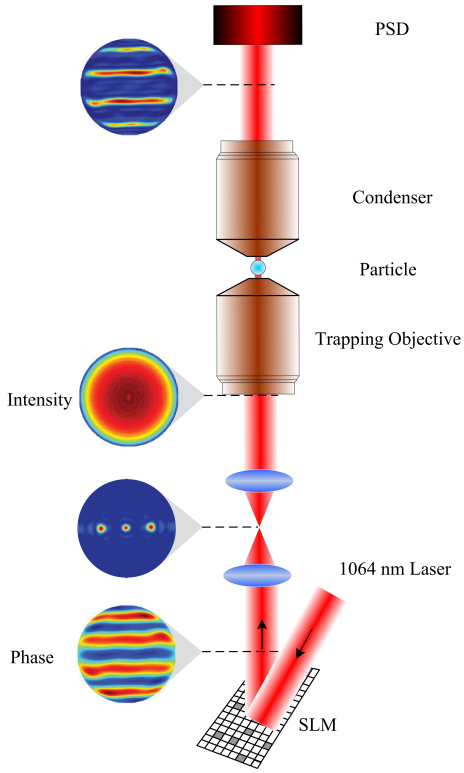

Figure 5.6: **Layout of the experiment.** ENTRAPS is implemented in standard holographic optical tweezers, with an SLM used to apply the calculated phase-profile for structured scattering and, is mapped to the back focal plane of the trapping objective. Using this configuration, the trapping field has an engineered phase and a Gaussian intensity distribution. After interaction with the particle, the light is separated into its discrete fringes. The phase and intensities shown here are calculated for 3.48 μm diameter particles and are scaled to the back aperture size of the objective having NA=1.25. Figure modified from ref. [1]

Afterwards, the scattered light is collected using similar objective which is generally called a condenser, it is directed towards a home-made position sensitive detector (PSD), which is mapped on the back-focal plane of the condenser, to determine the change in optical momentum, and consequently, the applied optical force. Unlike a quadrant photodetector (QPD), the PSD provides a signal which is proportional to the position of the laser intensity centroid on the detector element, and this is directly proportional to the applied optical force. Provided the particle stays within the linear region where $F = -\kappa x$. The back-focal plane imaging and PSD based detection system have been considered as an accurate method to measure the trapping force and particle position [139]. Trapped particles are also visually monitored using a Charged Coupled Device (CCD) with LED illumination. A simple layout of the holographic OT is shown in the figure. 5.6.

5.9 Experimental Measurements

5.9.1 Power Spectrum of Trapped Particles

For experimental verification of trap stiffness enhancement by structured illumination four different sized silica particles 3.48 μm, 5.09 μm (CV=10-15 %, Bangs Laboratories), 7.75 μm (CV=3.7 %Cospheric), and 10.0 μm (CV=10 %Microparticles-Nanoparticles) are trapped in water at room temperature with 250 mW optical power at the back-focal plane of the trapping objective. Particles are firstly trapped with Gaussian beam and then with structured incident light, and scattered light is measured on PSD. Then the power spectrum method is used to determine the trap stiffness by fitting the spectrum with the Brownian motion equation 2.25 to find the corner frequency and relative enhancement in the trap stiffness is measured by comparing the corner frequency for both types of incident beams.

For each particle size, data is averaged for four different measurements to reduce the laser intensity fluctuation noise and averaged spectra are fitted to the theory [54] using non-linear regression (nlinfit) function and its uncertainty is estimated using non-linear regression parameter confidence intervals (nlparci) function in MATLAB. Based on this measurement procedure, measured corner frequencies and trap stiffness enhancement factors are described in the table, and most noticeably for 7.75 μm particle, the corner frequency measured with ENTRAPS is 73.2 ± 2.8 Hz, while the Gaussian trap only achieves 2.66 ± 0.38 Hz. This constitutes an increase in the trap stiffness by a factor of 27.5$\pm$4.1. Given the simplicity of the system, this is remarkably close to the predicted enhancement of 25.

Figure 5.7 shows the power spectra for each of the above-mentioned particle both for a Gaussian and structured scattering illumination. It can be seen that there is a significant enhancement in the trap corner frequency using ENTRAPS. Figure 5.8 shows predicted and experimentally measured stiffness enhancement factor for both types of illumination. The graph in the inset shows that trap stiffness, for a Gaussian trap, decreases for particle sizes larger than 1 μm. However, it increases for ENTRAPS illumination until ~ 8 μm particle. In the main graph, experimentally measured trap stiffness enhancement factor is compared with a theory which has an excellent agreement.

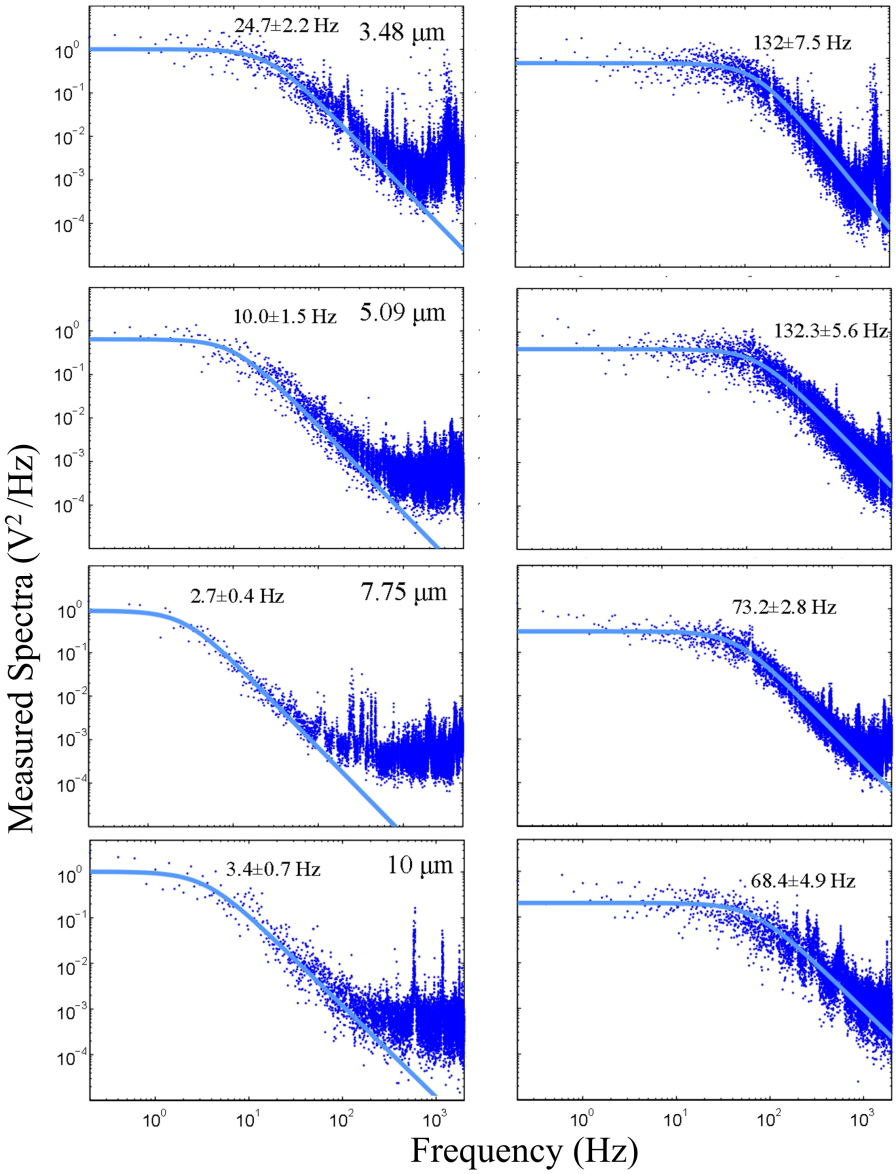

Figure 5.7: **Experimentally measured spectra of motion for all four particle diameters**. Particle sizes are 3.48, 5.09, 7.75, and 10.0 μm , as indicated for each trace. Left column: spectra measured with Gaussian traps, right column: spectra measured with ENTRAPS. The corner frequency is indicated within each plot. In every case, the use of ENTRAPS provided a clear increase in trap stiffness. Additionally, it improved the SNR, as can be seen from the increased amplitude in the characteristic $1/f^2$ roll-off region. Figure is modified from ref. [1]

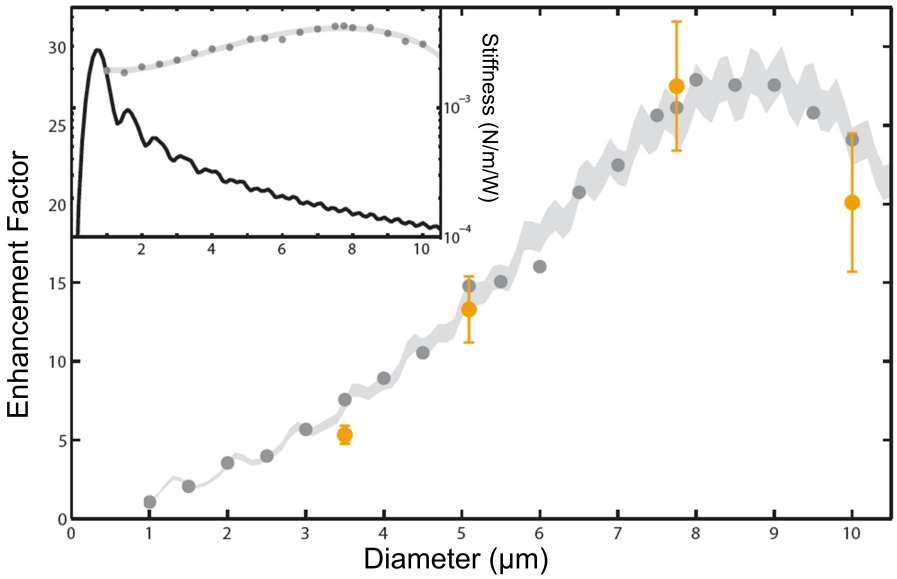

Figure 5.8: **Trap stiffness of ENTRAPS.** Stiffness enhancement factor as a function of particle size. Grey points, simulations; orange points, experiment. Error bars were determined statistically (Supplementary Information). Inset: simulated stiffness of Gaussian (black curve) and ENTRAPS (grey points) traps. Grey band: three-parameter polynomial fit to the ENTRAPS simulation, with width equal to 5% of the stiffness defining a rough uncertainty window for the simulation. The grey band in the main figure is derived from this band. Figure is modified from ref. [1]

5.9.2 Force vs. Displacement Curve

As a robust comparison and verification of stiffness enhancement, force vs displacement curves is considered to be the accurate method. The slope of this curve governs the trap stiffness according to the relation $\kappa = F/x$, provided that particle displacement is comparably small optical forces are in the linear regime [99]. Therefore, after measuring power spectra of the particles, the trapping power is reduced to approximately 1 mW such that the particles sink in the sample and are almost immobilized on the glass coverslip by gravity. Particles are scanned through the laser beam and the scattered light is measured on the PSD. Since the PSD provides an accurate estimate of the applied optical force, this calibration curve accurately maps the force at different displacements. Then this experimentally measured force vs. displacement curve is converted into normalized force units Q by fitting it with the theatrical curve as calculated from the OTT which shows excellent agreement for the Gaussian trapping profile.

Using this, the force could be characterized for ENTRAPS profiles and compared with theoretical predictions made without any fitting parameters. This shows good agreement, though there is a slight

asymmetry in displacement which could be due to the minor relative movement of the particle because of the very weak trap at 1 mW or positioning uncertainty of the nano-stages. Conventionally, particles are immobilized on the coverslip by keeping them unattended for few hours such that they settle down due to gravity, however, it is expected that some changes in their morphology happen near the coverslip and force vs. displacement curve do not show significant enhancement as the structured light field is very sensitive to the shape of the particle and slight deformation could give quite different results as discussed in detail in section 5.10.2.

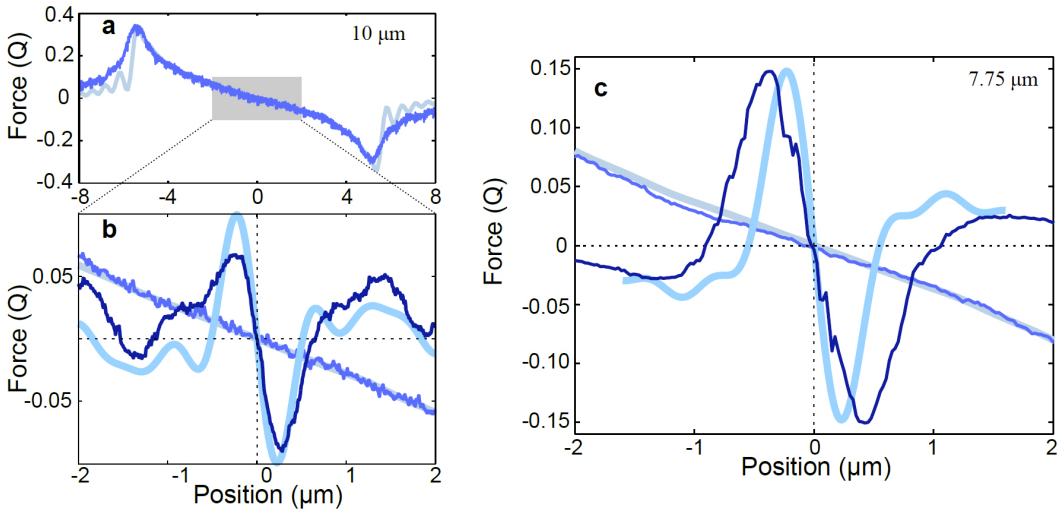

Figure 5.9: **Force-displacement curves measured and compared to theory predictions**. **(a)** The Gaussian trap shows excellent agreement between theoretical predictions (thick line) and the measurement from the PSD (dark curve); data taken with 10 μm particles. This profile was used to normalize the signal from the PSD into the unit Q, which is defined as the proportion of the radiation pressure that is applied as a force. The shaded regions indicate the axes of **(b)**, which compares the force-displacement curve for a Gaussian trap to ENTRAPS. The increase in trap stiffness is evident here, with ENTRAPS drastically increasing the trap gradient over a small range. **(c)** Similar results are also found for 7.75 μm particles, with the increase in stiffness over the use of the Gaussian trap clearly visible. The theory curves are calculated with no fitting parameters. The figure is modified from ref. [1]

In addition to improving the trap stiffness, it is noted that ENTRAPS has also provided a dramatic improvement in the measurement signal-to-noise ratio (SNR). Laser tracking in OT is based on a measurement of the deflection of the trapping light, with a signal that is proportional to the applied optical force F. Within the linear trapping region, this can be considered a position measurement because of $F = \kappa x$. Since ENTRAPS increases the trapping spring constant κ, it also increases the

Diameter	ENTRAPS Corner	Gaussian Corner	Enhancement	Prediction	SNR improvement
3.48 μm	132±7.5 Hz	24.7±2.2 Hz	5.33±0.57	7.5	22.8
5.09 μm	132.3±5.6 Hz	10.0±1.5 Hz	13.3±2.1	14.8	111
7.75 μm	73.2±2.8 Hz	2.66±0.38 Hz	27.5±4.1	26.1	249
10.0 μm	68.4±4.9 Hz	3.4 ± 0.7 Hz	20.1±4.4	24.1	107

Table 5.1: **Predicted and experimentally measured ENTRAPS features**. The characteristics of the spectra shown in Fig.5.7. The corner frequencies and enhancements are shown here, together with the predicted enhancement. Table modified from ref. [1].

measured signal for a small particle displacement. In principle, enhancement in the SNR ratio (SNR) is determined by comparing the relative amplitudes of position spectrum for both types of incident beams and for 7.75 μm particle, ENTRAPS has improved SNR by a factor of 249. For clarity, all parameters associated trap stiffness enhancement and SNR are tabulated in Table 5.1.

5.10 Factors affecting ENTRAPS performance

5.10.1 Optical Aberrations and SLM phase-flicker

There are a number of complicating factors which could could limit the trapping stiffness and prevent the experiment from achieving the full factor of predicted enhancement. In particular, previous characterization of the SLM shows that it does not apply a constant phase, but the phase instead flickers with the video refresh rate with a peak-to-peak flicker amplitude of 15% the applied phase, which corresponds to 1 radian of flicker when applying a 2 π phase shift [140]. The effect of this is to reduce the efficiency with which the SLM generates the desired profile.

It is also important that all the fields be aligned correctly to ensure that the hologram shifts the phase of the trapping light in the manner predicted. This requires the trapping light to be centered on both the SLM and the objective, while the hologram needs to be generated with the correct radius and any aberrations in the system need to be eliminated. In the experiments reported here, aberrations are compensated with the SLM to visually optimize the point spread function of the Gaussian field using a procedure similar to ref. [137]. This procedure approximately eliminates the aberrations, though it is likely that some aberrations remained in the system. Despite these technical limitations, the demonstrated enhancement in trap stiffness is in excellent agreement with theoretical prediction.

This shows that ENTRAPS is remarkably robust and can be applied with relatively basic trapping equipment. Improvements in the holographic OT technology can decrease the particle's variance and therefore, can further increase the trap stiffness [141].

5.10.2 Parameters of particle

One potential challenge to using ENTRAPS is that it relies on pre-calculation of the Mie scattering profile, and this can be inaccurate if the particle size, shape, or refractive index differs from the parameters assumed in the model. ENTRAPS exhibits relatively tight tolerance on the particle diameter, such that the trap stiffness would become zero for 4% change in diameter or refractive index, though the refractive index is determined more precisely by most of the suppliers. Beyond this tolerance limit, trap stiffness is predicted to be of the negative sign which means particle will experience a repulsive force from the trap instead gradient trapping force which pulls the particle towards the equilibrium trapping position.

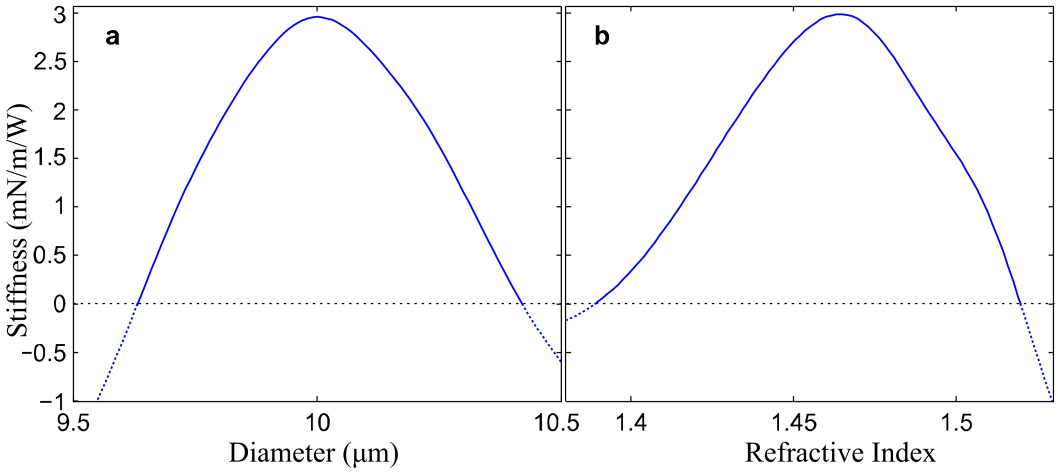

Figure 5.10: **Dependence of the trap stiffness on (a) particle diameter and (b) refractive index, for the 10 μm ENTRAPS hologram.** The particle is centered at the focus, and the trapping field is the same as that used in the main text. The curve is dashed where the trap stiffness falls below zero, as this denotes an anti-trap feature with the particle repelled from the beam center. The trap stiffness can be seen to vary strongly with both the particle diameter and refractive index. Figure is taken from ref. [1]

As shown in the figure 5.10, changing particle size by ~ 2 % reduces the trap stiffness by a factor of 2 and altering refractive index does the same by a similar factor. For 10 μm particle, 0.4 μm diameter and 0.066 refractive index n change can alter the optical path length through the particle by $\sim \lambda/2$ which reverses the sign of scattering fringes.

Experimentally, it is observed that applying hologram calculated for perfectly 10 μm particle to particles with more than 4 % uncertainty do not exhibit a significant increase in the trap stiffness. Therefore, for good efficiency of ENTRAPS, it is necessary to use particles which have very good spherical geometry and have $< 1\%$ uncertainty or tolerance in the diameter and refractive index. Although the tolerance on particle size is tight, it is possible to compensate for small changes in the particle diameter with a linear rescaling of the angular phase profile in the far field and, in X-axis direction while maintaining y-axis scaling.

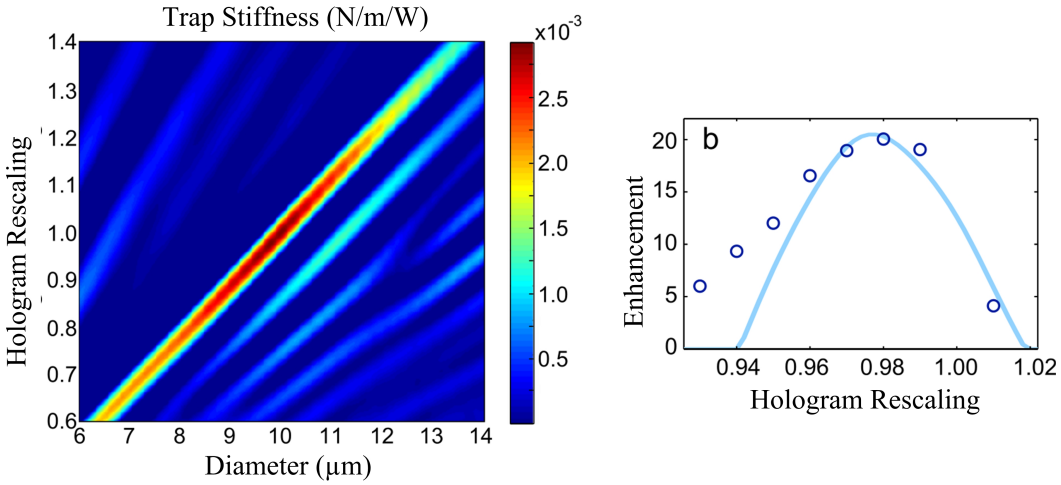

Figure 5.11: **ENTRAPS is implemented based on accurate recalculation of the scattering profile**. This introduces tight tolerances in the particle diameter, as shown in Fig.5.10. However, small changes in the particle diameter can be compensated by rescaling the x axis of the phase hologram (plot **(a)**), as shown for the 10 μm particle hologram. This allows the size tolerance to be broadened by over an order of magnitude, which makes experimental demonstration far easier. Large regions of this plot show no stable trap (dark blue, $\kappa = 0$); in these regions, the trapping phase is mismatched to the particle size such that it is repelled from the optical focus ($\kappa < 0$). Higher order trapping sites are evident where the change in the transmitted phase approaches 2π such that stable trapping can once again become possible. **(b)** We tested the dependence of the stiffness enhancement on the rescaling parameter for a 9.8 μm diameter particle and compared the data to theory. This shows good agreement around the over the peak trapping range, though at very small rescaling parameter we observed stable trapping even when this was not predicted. This is because the trapping field features multiple trapping sites, and when the central trapping site becomes unstable the particle can remain in secondary trap sites. Figure is taken from ref. [1]

Using such a linear rescaling, the phase hologram which is calculated to optimize trapping of 10 μm particles could be used to generate an efficient trap over a 2 μm range, which makes it rela-

tively straightforward to implement in experiments with a promise of getting higher trap stiffness (see Fig.5.11).

5.11 ENTRAPS Features

As the holograms are optimized for one dimension only i.e. x-axis and considering particle is trapped at the focus, it is important to observe the lateral forces at different axial height as particle could be trapped at an axially higher position due to large scattering forces, or at lower position due to the gravity weight of the particle. For this purpose, 10 μm particle is scanned through hologram at different axial positions to get force vs. displacement curves and at 2.54 μm axial height, it is observed that lateral trapping force transforms into the repelling force which pushes the particle away from the trap. As slope of force vs. position determines the trap stiffness, it can be seen in the figure that strong trap stiffness is achieved at zero axial height while at 2.54 μm, the slope is mirrored around y-axis which means reveal of the optical spring force on the particle, though the axial position dependence of this anti-trap phenomenon is not precisely described in this work.

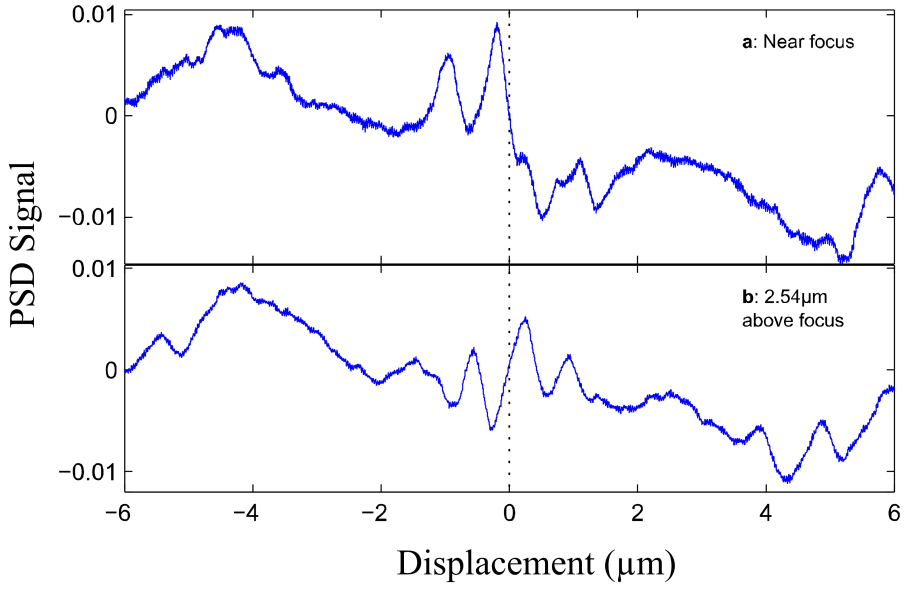

Figure 5.12: **Force-displacement curves measured with the PSD, with a 10 μ particle (a) near the focal plane, and (b) 2.54 μ above the focus**. The trapping field is the same as used for the experimental results. Near the focus the calibration curve shows a strong trapping feature, while above the focus this changes into an anti-trap feature. This data also shows some asymmetry between positive and negative displacements in x, which suggests that optical aberrations were not fully compensated for this set of data. Figure is taken from ref. [1]

Another interesting phenomenon of this structured illumination is the existence of several stable trap-

ping positions as shown in force vs. displacement curves. ENTRAPS achieves significantly higher trap stiffness for small displacements of the particle, however, for larger displacement, multiple equilibrium positions are observed and particles can also be trapped at the slightly different lateral position from the beam axis, with a relatively lower trap stiffness which is also predicted from the theory. As it can be seen from the figure 5.12, 5 trapping positions can be possible for 10 μm particle with relatively lower trap stiffness.

5.12 Limitations of ENTRAPS

Although ENTRAPS governs huge increment in trap stiffness and SNR, there are a few limitations of this method. ENTRAPS is based on populating the lower order Mie-scattering fringes in to higher order modes and, these modes and interference fringes increase with increasing size of the particle. Therefore, ENTRAPS is particularly suitable for larger sized particles and doesn't give any improvements for the particles having a size smaller or comparable to the wavelength of incident beam. Hence, ENTRAPS can barely give any advantages to microrheology measurements in which smaller sized particles are mostly employed [142, 143]. Furthermore, phase profiles have been optimized in one direction only and therefore, trap stiffness and SNR is enhanced only in one direction. This might not be useful for the applications in which a trapped particle is used as a probe to acquire three-dimensional information from the surroundings [26, 144], however, it might be possible to achieve such enhancements in three dimensions by calculating the three-dimensional optimal phase profiles.

Another limiting factor of ENTRAPS is the reduced trapping region which means that ENTRAPS apply high trapping force for very small particle displacement in an optical trap. For instance, a force vs. displacement curve for a 10 μm particle is around 500 nm which is quite small as compared to the simple Gaussian trap which has a trapping region almost equal to the particle size. In principle, the scattering force on an optically trapped particle scales linearly with displacement in proportion to the trap stiffness. As the momentum transfer of light on the particle cannot exceed $\hbar$, the trapping range cannot be exceeded indefinitely with an increase in trap stiffness. In the current experiments, the momentum transfer per photon in $\hbar k/7$ which means that the trapping region can be further increased by 7 times, keeping the traps stiffness constant.

The approach taken here to calculate optimized phase profiles was very computationally expensive. For instance, it took 120 hours on a 4-core 3.4 GHz processor with 16GB of RAM to calculate a hologram for 10 μm particle with $N_{max} = 65$. This potential bottleneck has since been lifted with an improved phase optimization algorithm [131].

Experimentally, ENTRAPS is implemented using electronic controlled phase-only SLMs which have phase-flicker. However, by carefully calculating the phase profiles, hologram patterns can be engraved on an optical phase plate which could give higher efficiencies in all perspectives.

5.13 Conclusions

In this chapter, a new interferometric type optical trapping technique is presented which creates an interference pattern in the particle similar to beam-splitter. In this technique, the Mie scattering fringes from the spherical particle are tailored to produce the strong interference which governs constructive and destructive interference of fringes instead deflecting the light as in the standard optical tweezers (OT). This interference makes the particle behave like a beam-splitter and results in the greater enhancement in optical trap stiffness and signal-to-noise ratio, for particle sizes typically greater than the incident light wavelength. This is achieved by structuring the phase-profile of Gaussian beam and an algorithm is written to run the phase-optimization routine based on the OT computational toolbox (OTT). This structured illumination to enhance the trap stiffness and SNR could have broad range of applications in both both engineering and fundamental science.

Bibliography

[1] M. A. Taylor, M. Waleed, A. B. Stilgoe, H. Rubinsztein-Dunlop, and W. P. Bowen, "Enhanced optical trapping via structured scattering," *Nature Photonics*, vol. 9, no. 10, pp. 669–673, 2015.

[2] N. Mauranyapin, L. Madsen, M. Taylor, M. Waleed, and W. Bowen, "Evanescent single-molecule biosensing with quantum-limited precision," *Nature Photonics*, vol. 11, no. 8, p. 477, 2017.

[3] J. H. Poynting, "On the transfer of energy in the electromagnetic field," *Philosophical Transactions of the Royal Society of London*, vol. 175, pp. 343–361, 1884.

[4] P. Lebedew, "Untersuchungen über die druckkräfte des lichtes," *Annalen der Physik*, vol. 311, no. 11, pp. 433–458, 1901.

[5] R. A. Beth, "Mechanical detection and measurement of the angular momentum of light," *Physical Review*, vol. 50, no. 2, p. 115, 1936.

[6] A. Ashkin, "Acceleration and trapping of particles by radiation pressure," *Physical review letters*, vol. 24, no. 4, p. 156, 1970.

[7] A. Ashkin, J. M. Dziedzic, J. Bjorkholm, and S. Chu, "Observation of a single-beam gradient force optical trap for dielectric particles," *Optics letters*, vol. 11, no. 5, pp. 288–290, 1986.

[8] F. Gittes and C. F. Schmidt, "Interference model for back-focal-plane displacement detection in optical tweezers," *Optics letters*, vol. 23, no. 1, pp. 7–9, 1998.

[9] A. Pralle, M. Prummer, E.-L. Florin, E. Stelzer, J. Hörber, *et al.*, "Three-dimensional high-resolution particle tracking for optical tweezers by forward scattered light," *Microscopy research and technique*, vol. 44, no. 5, pp. 378–386, 1999.

[10] J. C. Crocker and D. G. Grier, "Microscopic measurement of the pair interaction potential of charge-stabilized colloid," *Physical review letters*, vol. 73, no. 2, p. 352, 1994.

[11] Y. Ohshima, H. Sakagami, K. Okumoto, A. Tokoyoda, T. Igarashi, K. Shintaku, S. Toride, H. Sekino, K. Kabuto, and I. Nishio, "Direct measurement of infinitesimal depletion force in a colloid-polymer mixture by laser radiation pressure," *Physical review letters*, vol. 78, no. 20, p. 3963, 1997.

[12] J. C. Crocker, J. Matteo, A. Dinsmore, and A. Yodh, "Entropic attraction and repulsion in binary colloids probed with a line optical tweezer," *Physical review letters*, vol. 82, no. 21, p. 4352, 1999.

[13] O. M. Maragò, P. H. Jones, P. G. Gucciardi, G. Volpe, and A. C. Ferrari, "Optical trapping and manipulation of nanostructures," *Nature nanotechnology*, vol. 8, no. 11, pp. 807–819, 2013.

[14] Y. Arita, M. Mazilu, and K. Dholakia, "Laser-induced rotation and cooling of a trapped microgyroscope in vacuum," *Nature communications*, vol. 4, p. 2374, 2013.

[15] N. Kiesel, F. Blaser, U. Delić, D. Grass, R. Kaltenbaek, and M. Aspelmeyer, "Cavity cooling of an optically levitated submicron particle," *Proceedings of the National Academy of Sciences*, vol. 110, no. 35, pp. 14180–14185, 2013.

[16] D. E. Chang, C. Regal, S. Papp, D. Wilson, J. Ye, O. Painter, H. J. Kimble, and P. Zoller, "Cavity opto-mechanics using an optically levitated nanosphere," *Proceedings of the National Academy of Sciences*, vol. 107, no. 3, pp. 1005–1010, 2010.

[17] T. Li, "Millikelvin cooling of an optically trapped microsphere in vacuum," in *Fundamental Tests of Physics with Optically Trapped Microspheres*, pp. 81–110, Springer, 2013.

[18] A. A. Geraci, S. B. Papp, and J. Kitching, "Short-range force detection using optically cooled levitated microspheres," *Physical review letters*, vol. 105, no. 10, p. 101101, 2010.

[19] A. Bassi, K. Lochan, S. Satin, T. P. Singh, and H. Ulbricht, "Models of wave-function collapse, underlying theories, and experimental tests," *Reviews of Modern Physics*, vol. 85, no. 2, p. 471, 2013.

[20] C. Yi, C.-W. Li, S. Ji, and M. Yang, "Microfluidics technology for manipulation and analysis of biological cells," *Analytica Chimica Acta*, vol. 560, no. 1, pp. 1–23, 2006.

[21] H. Löwen, "Colloidal soft matter under external control," *Journal of Physics: Condensed Matter*, vol. 13, no. 24, p. R415, 2001.

[22] D. L. Vossen, A. van der Horst, M. Dogterom, and A. van Blaaderen, "Optical tweezers and confocal microscopy for simultaneous three-dimensional manipulation and imaging in concentrated colloidal dispersions," *Review of Scientific Instruments*, vol. 75, no. 9, pp. 2960–2970, 2004.

[23] E.-L. Florin, A. Pralle, J. H. Hörber, and E. H. Stelzer, "Photonic force microscope based on optical tweezers and two-photon excitation for biological applications," *Journal of structural biology*, vol. 119, no. 2, pp. 202–211, 1997.

[24] F. Ndoye, M. S. Yousafzai, G. Coceano, S. Bonin, G. Scoles, O. Ka, J. Niemela, and D. Cojoc, "The influence of lateral forces on the cell stiffness measurement by optical tweezers vertical indentation," *International Journal of Optomechatronics*, vol. 10, no. 1, pp. 53–62, 2016.

[25] T. Lu, B. Corliss, S. Lee, and B. Anvari, "Combined optical tweezers and quantitative phase imaging for mechanical characterization of ovarian cells," in *Optical Trapping Applications*, pp. OtTu2E–2, Optical Society of America, 2017.

[26] L. Friedrich and A. Rohrbach, "Surface imaging beyond the diffraction limit with optically trapped spheres," *Nature nanotechnology*, vol. 10, no. 12, pp. 1064–1069, 2015.

[27] N. T. Shaked, Y. Roichman, and M. Habaza, "Live cell trapping and rotation for label-free tomography and 3-d refractive-index imaging," in *Optical Trapping Applications*, pp. OtM4E–3, Optical Society of America, 2017.

[28] J. W. Black, M. Kamenetska, and Z. Ganim, "An optical tweezers platform for single molecule force spectroscopy in organic solvents," *Nano letters*, vol. 17, no. 11, pp. 6598–6605, 2017.

[29] M. Mammen, K. Helmerson, R. Kishore, S.-K. Choi, W. D. Phillips, and G. M. Whitesides, "Optically controlled collisions of biological objects to evaluate potent polyvalent inhibitors of virus-cell adhesion," *Chemistry & biology*, vol. 3, no. 9, pp. 757–763, 1996.

[30] S. B. Smith, L. Finzi, and C. Bustamante, "Direct mechanical measurements of the elasticity of single dna molecules by using magnetic beads," *Science*, vol. 258, no. 5085, pp. 1122–1126, 1992.

[31] R. I. Litvinov, H. Shuman, J. S. Bennett, and J. W. Weisel, "Binding strength and activation state of single fibrinogen-integrin pairs on living cells," *Proceedings of the National Academy of Sciences*, vol. 99, no. 11, pp. 7426–7431, 2002.

[32] M. D. Wang, M. J. Schnitzer, H. Yin, R. Landick, J. Gelles, and S. M. Block, "Force and velocity measured for single molecules of rna polymerase," *Science*, vol. 282, no. 5390, pp. 902–907, 1998.

[33] L. Bai, T. J. Santangelo, and M. D. Wang, "Single-molecule analysis of rna polymerase transcription," *Annu. Rev. Biophys. Biomol. Struct.*, vol. 35, pp. 343–360, 2006.

[34] K. M. Herbert, W. J. Greenleaf, and S. M. Block, "Single-molecule studies of rna polymerase: motoring along," *Annu. Rev. Biochem.*, vol. 77, pp. 149–176, 2008.

[35] E. A. Abbondanzieri, W. J. Greenleaf, J. W. Shaevitz, R. Landick, and S. M. Block, "Direct observation of base-pair stepping by rna polymerase," *Nature*, vol. 438, no. 7067, pp. 460–465, 2005.

[36] L. Tskhovrebova, J. Trinick, J. Sleep, and R. Simmons, "Elasticity and unfolding of single molecules of the giant muscle protein titin," *Nature*, vol. 387, no. 6630, p. 308, 1997.

[37] M. S. Kellermayer, S. Smith, C. Bustamante, and H. L. Granzier, "Mechanical manipulation of single titin molecules with laser tweezers," in *Elastic filaments of the cell*, pp. 111–128, Springer, 2000.

[38] J. Liphardt, B. Onoa, S. B. Smith, I. Tinoco, and C. Bustamante, "Reversible unfolding of single rna molecules by mechanical force," *Science*, vol. 292, no. 5517, pp. 733–737, 2001.

[39] S. M. Block, L. S. Goldstein, and B. J. Schnapp, "Bead movement by single kinesin molecules studied with optical tweezers," *Nature*, vol. 348, no. 6299, pp. 348–352, 1990.

[40] S. Jeney, E. H. Stelzer, H. Grubmüller, and E.-L. Florin, "Mechanical properties of single motor molecules studied by three-dimensional thermal force probing in optical tweezers," *ChemPhysChem*, vol. 5, no. 8, pp. 1150–1158, 2004.

[41] S. C. Kuo and M. P. Sheetz, "Force of single kinesin molecules measured with optical tweezers," *Science*, vol. 260, no. 5105, pp. 232–234, 1993.

[42] J. T. Finer, R. M. Simmons, and J. A. Spudich, "Single myosin molecule mechanics: piconewton forces and nanometre steps," *Nature*, vol. 368, no. 6467, pp. 113–119, 1994.

[43] K. Visscher, M. J. Schnitzer, and S. M. Block, "Single kinesin molecules studied with a molecular force clamp," *Nature*, vol. 400, no. 6740, pp. 184–189, 1999.

[44] J. Molloy, J. Burns, J. Kendrick-Jones, R. Tregear, and D. White, "Movement and force produced by a single myosin head," *Nature*, vol. 378, no. 6553, p. 209, 1995.

[45] D. Weitz, J. Zhu, D. Durian, H. Gang, and D. Pine, "Diffusing-wave spectroscopy: The technique and some applications," *Physica Scripta*, vol. 1993, no. T49B, p. 610, 1993.

[46] D. Wirtz, "Particle-tracking microrheology of living cells: principles and applications," *Annual review of biophysics*, vol. 38, pp. 301–326, 2009.

[47] M. Tassieri, T. Waigh, J. Trinick, A. Aggeli, and R. Evans, "Analysis of the linear viscoelasticity of polyelectrolytes by magnetic microrheometry—pulsed creep experiments and the one particle response," *Journal of rheology*, vol. 54, no. 1, pp. 117–131, 2010.

[48] A. R. Bausch, W. Möller, and E. Sackmann, "Measurement of local viscoelasticity and forces in living cells by magnetic tweezers," *Biophysical journal*, vol. 76, no. 1, pp. 573–579, 1999.

[49] T. Okajima and H. Tokumoto, "Nanorheology of living cells investigated by atomic force microscopy," *Nihon reoroji gakkaishi*, vol. 36, no. 2, pp. 81–86, 2008.

[50] R. Brau, J. Ferrer, H. Lee, C. Castro, B. Tam, P. Tarsa, P. Matsudaira, M. Boyce, R. Kamm, and M. Lang, "Passive and active microrheology with optical tweezers," *Journal of Optics A: Pure and Applied Optics*, vol. 9, no. 8, p. S103, 2007.

[51] M. Atakhorrami, J. I. Sulkowska, K. Addas, G. Koenderink, J. Tang, A. Levine, F. MacKintosh, and C. Schmidt, "Correlated fluctuations of microparticles in viscoelastic solutions: Quantitative measurement of material properties by microrheology in the presence of optical traps," *Physical Review E*, vol. 73, no. 6, p. 061501, 2006.

[52] M. Tassieri, G. M. Gibson, R. Evans, A. M. Yao, R. Warren, M. J. Padgett, and J. M. Cooper, "Measuring storage and loss moduli using optical tweezers: Broadband microrheology," *Physical Review E*, vol. 81, no. 2, p. 026308, 2010.

[53] D. Preece, R. Warren, R. Evans, G. M. Gibson, M. J. Padgett, J. M. Cooper, and M. Tassieri, "Optical tweezers: wideband microrheology," *Journal of optics*, vol. 13, no. 4, p. 044022, 2011.

[54] K. Berg-Sørensen and H. Flyvbjerg, "Power spectrum analysis for optical tweezers," *Review of Scientific Instruments*, vol. 75, no. 3, pp. 594–612, 2004.

[55] B. Lukić, S. Jeney, C. Tischer, A. Kulik, L. Forró, and E.-L. Florin, "Direct observation of nondiffusive motion of a brownian particle," *Physical review letters*, vol. 95, no. 16, p. 160601, 2005.

[56] E.-L. Florin, A. Pralle, E. Stelzer, and J. Hörber, "Photonic force microscope calibration by thermal noise analysis," *Applied Physics A: Materials Science & Processing*, vol. 66, pp. S75–S78, 1998.

[57] H. Felgner, O. Müller, and M. Schliwa, "Calibration of light forces in optical tweezers," *Applied optics*, vol. 34, no. 6, pp. 977–982, 1995.

[58] K. C. Vermeulen, J. van Mameren, G. J. Stienen, E. J. Peterman, G. J. Wuite, and C. F. Schmidt, "Calibrating bead displacements in optical tweezers using acousto-optic deflectors," *Review of Scientific Instruments*, vol. 77, no. 1, p. 013704, 2006.

[59] J. Mas, A. C. Richardson, S. N. S. Reihani, L. B. Oddershede, and K. Berg-Sørensen, "Quantitative determination of optical trapping strength and viscoelastic moduli inside living cells," *Physical biology*, vol. 10, no. 4, p. 046006, 2013.

[60] D. Mizuno, C. Tardin, C. F. Schmidt, and F. C. MacKintosh, "Nonequilibrium mechanics of active cytoskeletal networks," *Science*, vol. 315, no. 5810, pp. 370–373, 2007.

[61] T. Toyota, D. A. Head, C. F. Schmidt, and D. Mizuno, "Non-gaussian athermal fluctuations in active gels," *Soft Matter*, vol. 7, no. 7, pp. 3234–3239, 2011.

[62] A. W. Harrison, D. A. Kenwright, T. A. Waigh, P. G. Woodman, and V. J. Allan, "Modes of correlated angular motion in live cells across three distinct time scales," *Physical biology*, vol. 10, no. 3, p. 036002, 2013.

[63] J. Snider, F. Lin, N. Zahedi, V. Rodionov, C. Y. Clare, and S. P. Gross, "Intracellular actin-based transport: how far you go depends on how often you switch," *Proceedings of the National Academy of Sciences of the United States of America*, vol. 101, no. 36, pp. 13204–13209, 2004.

[64] I. M. Kulić, A. E. Brown, H. Kim, C. Kural, B. Blehm, P. R. Selvin, P. C. Nelson, and V. I. Gelfand, "The role of microtubule movement in bidirectional organelle transport," *Proceedings of the National Academy of Sciences*, vol. 105, no. 29, pp. 10011–10016, 2008.

[65] C. P. Brangwynne, G. H. Koenderink, F. C. MacKintosh, and D. A. Weitz, "Intracellular transport by active diffusion," *Trends in cell biology*, vol. 19, no. 9, pp. 423–427, 2009.

[66] M. Fischer, A. C. Richardson, S. N. S. Reihani, L. B. Oddershede, and K. Berg-Sørensen, "Active-passive calibration of optical tweezers in viscoelastic media," *Review of Scientific Instruments*, vol. 81, no. 1, p. 015103, 2010.

[67] M. Tassieri, F. Del Giudice, E. J. Robertson, N. Jain, B. Fries, R. Wilson, A. Glidle, F. Greco, P. A. Netti, P. L. Maffettone, *et al.*, "Microrheology with optical tweezers: Measuring the relative viscosity of solutions 'at a glance'," *Scientific reports*, vol. 5, p. 8831, 2015.

[68] M. Tassieri, "Linear microrheology with optical tweezers of living cells 'is not an option'!," *Soft Matter*, vol. 11, no. 29, pp. 5792–5798, 2015.

[69] T. Li, S. Kheifets, D. Medellin, and M. G. Raizen, "Measurement of the instantaneous velocity of a brownian particle," *Science*, vol. 328, no. 5986, pp. 1673–1675, 2010.

[70] S. Kheifets, A. Simha, K. Melin, T. Li, and M. G. Raizen, "Observation of brownian motion in liquids at short times: instantaneous velocity and memory loss," *science*, vol. 343, no. 6178, pp. 1493–1496, 2014.

[71] R. Huang, I. Chavez, K. M. Taute, B. Lukić, S. Jeney, M. G. Raizen, and E.-L. Florin, "Direct observation of the full transition from ballistic to diffusive brownian motion in a liquid," *Nature Physics*, vol. 7, no. 7, pp. 576–580, 2011.

[72] J. Mo, A. Simha, S. Kheifets, and M. G. Raizen, "Testing the maxwell-boltzmann distribution using brownian particles," *Optics express*, vol. 23, no. 2, pp. 1888–1893, 2015.

[73] P. M. Neto and H. Nussenzveig, "Theory of optical tweezers," *EPL (Europhysics Letters)*, vol. 50, no. 5, p. 702, 2000.

[74] A. Callegari, M. Mijalkov, A. B. Gököz, and G. Volpe, "Computational toolbox for optical tweezers in geometrical optics," *JOSA B*, vol. 32, no. 5, pp. B11–B19, 2015.

[75] L. Wilson, P. T. Matsudaira, and M. P. Sheetz, *Laser tweezers in cell biology*, vol. 55. Academic Press, 1997.

[76] K. C. Neuman, E. H. Chadd, G. F. Liou, K. Bergman, and S. M. Block, "Characterization of photodamage to escherichia coli in optical traps," *Biophysical journal*, vol. 77, no. 5, pp. 2856–2863, 1999.

[77] D. Palima and J. Glückstad, "Gearing up for optical microrobotics: micromanipulation and actuation of synthetic microstructures by optical forces," *Laser & Photonics Reviews*, vol. 7, no. 4, pp. 478–494, 2013.

[78] J. Köhler, S. I. Ksouri, C. Esen, and A. Ostendorf, "Optical screw-wrench for microassembly," *Microsystems & Nanoengineering*, vol. 3, p. 16083, 2017.

[79] M.-C. Zhong, X.-B. Wei, J.-H. Zhou, Z.-Q. Wang, and Y.-M. Li, "Trapping red blood cells in living animals using optical tweezers," *Nature communications*, vol. 4, p. 1768, 2013.

[80] G. Tomaiuolo, "Biomechanical properties of red blood cells in health and disease towards microfluidics," *Biomicrofluidics*, vol. 8, no. 5, p. 051501, 2014.

[81] R. Agrawal, T. Smart, J. Nobre-Cardoso, C. Richards, R. Bhatnagar, A. Tufail, D. Shima, P. H. Jones, and C. Pavesio, "Assessment of red blood cell deformability in type 2 diabetes mellitus and diabetic retinopathy by dual optical tweezers stretching technique," *Scientific reports*, vol. 6, 2016.

[82] R. Bowman, A. Jesacher, G. Thalhammer, G. Gibson, M. Ritsch-Marte, and M. Padgett, "Position clamping in a holographic counterpropagating optical trap," *Optics express*, vol. 19, no. 10, pp. 9908–9914, 2011.

[83] X. Li, H. Yang, H. Huang, and D. Sun, "A switching controller for high speed cell transportation by using a robot-aided optical tweezers system," *Automatica*, vol. 89, pp. 308–315, 2018.

[84] I. A. Favre-Bulle, A. B. Stilgoe, H. Rubinsztein-Dunlop, and E. K. Scott, "Optical trapping of otoliths drives vestibular behaviours in larval zebrafish," *Nature communications*, vol. 8, no. 1, p. 630, 2017.

[85] D. C. Moore, A. D. Rider, and G. Gratta, "Search for millicharged particles using optically levitated microspheres," *Physical review letters*, vol. 113, no. 25, p. 251801, 2014.

[86] G. Thalhammer, R. Steiger, S. Bernet, and M. Ritsch-Marte, "Optical macro-tweezers: trapping of highly motile micro-organisms," *Journal of Optics*, vol. 13, no. 4, p. 044024, 2011.

[87] T. A. Nieminen, N. R. Heckenberg, and H. Rubinsztein-Dunlop, "Forces in optical tweezers with radially and azimuthally polarized trapping beams," *Optics letters*, vol. 33, no. 2, pp. 122–124, 2008.

[88] A. T. O'Neil and M. J. Padgett, "Axial and lateral trapping efficiency of laguerre–gaussian modes in inverted optical tweezers," *Optics Communications*, vol. 193, no. 1, pp. 45–50, 2001.

[89] Y. Kozawa and S. Sato, "Optical trapping of micrometer-sized dielectric particles by cylindrical vector beams," *Optics Express*, vol. 18, no. 10, pp. 10828–10833, 2010.

[90] A. Jannasch, A. F. Demirörs, P. D. Van Oostrum, A. Van Blaaderen, and E. Schäffer, "Nanonewton optical force trap employing anti-reflection coated, high-refractive-index titania microspheres," *Nature Photonics*, vol. 6, no. 7, pp. 469–473, 2012.

[91] J. E. Molloy and M. J. Padgett, "Lights, action: optical tweezers," *Contemporary physics*, vol. 43, no. 4, pp. 241–258, 2002.

[92] Y. Harada and T. Asakura, "Radiation forces on a dielectric sphere in the rayleigh scattering regime," *Optics communications*, vol. 124, no. 5-6, pp. 529–541, 1996.

[93] K. Svoboda and S. M. Block, "Biological applications of optical forces," *Annual review of biophysics and biomolecular structure*, vol. 23, no. 1, pp. 247–285, 1994.

[94] V. L. Loke, M. P. Mengüç, and T. A. Nieminen, "Discrete-dipole approximation with surface interaction: Computational toolbox for matlab," *Journal of Quantitative Spectroscopy and Radiative Transfer*, vol. 112, no. 11, pp. 1711–1725, 2011.

[95] A. Ashkin, "Forces of a single-beam gradient laser trap on a dielectric sphere in the ray optics regime," *Biophysical journal*, vol. 61, no. 2, pp. 569–582, 1992.

[96] J. Barton, D. Alexander, and S. Schaub, "Theoretical determination of net radiation force and torque for a spherical particle illuminated by a focused laser beam," *Journal of Applied Physics*, vol. 66, no. 10, pp. 4594–4602, 1989.

[97] J. Barton, "Internal and near-surface electromagnetic fields for a spheroidal particle with arbitrary illumination," *Applied optics*, vol. 34, no. 24, pp. 5542–5551, 1995.

[98] G. Gouesbet, "Generalized lorenz–mie theories, the third decade: a perspective," *Journal of Quantitative Spectroscopy and Radiative Transfer*, vol. 110, no. 14, pp. 1223–1238, 2009.

[99] T. A. Nieminen, V. L. Loke, A. B. Stilgoe, G. Knöner, A. M. Brańczyk, N. R. Heckenberg, and H. Rubinsztein-Dunlop, "Optical tweezers computational toolbox," *Journal of Optics A: Pure and Applied Optics*, vol. 9, no. 8, p. S196, 2007.

[100] T. Li, S. Kheifets, and M. G. Raizen, "Millikelvin cooling of an optically trapped microsphere in vacuum," *Nature Physics*, vol. 7, no. 7, p. 527, 2011.

[101] R. Brown, "Xxvii. a brief account of microscopical observations made in the months of june, july and august 1827, on the particles contained in the pollen of plants; and on the general

existence of active molecules in organic and inorganic bodies," *Philosophical Magazine Series 2*, vol. 4, no. 21, pp. 161–173, 1828.

[102] E. Nelson, "Derivation of the schrödinger equation from newtonian mechanics," *Physical review*, vol. 150, no. 4, p. 1079, 1966.

[103] A. Einstein, *Investigations on the Theory of the Brownian Movement*. Courier Corporation, 1956.

[104] A. Einstein, "Theoretische bemerkungen über die brownsche bewegung," *Berichte der Bunsengesellschaft für physikalische Chemie*, vol. 13, no. 6, pp. 41–42, 1907.

[105] I. Oppenheim, "The langevin equation with applications in physics, chemistry and electrical engineering," *Journal of Statistical Physics*, vol. 88, no. 1, pp. 519–520, 1997.

[106] R. Zwanzig and M. Bixon, "Compressibility effects in the hydrodynamic theory of brownian motion," *Journal of Fluid Mechanics*, vol. 69, no. 1, pp. 21–25, 1975.

[107] C. Brennen, "A review of added mass and fluid inertial forces.," tech. rep., BRENNEN (CE) SIERRA MADRE CA, 1982.

[108] E. Hinch, "Application of the langevin equation to fluid suspensions," *Journal of Fluid Mechanics*, vol. 72, no. 3, pp. 499–511, 1975.

[109] H. Clercx and P. Schram, "Brownian particles in shear flow and harmonic potentials: A study of long-time tails," *Physical Review A*, vol. 46, no. 4, p. 1942, 1992.

[110] B. Lukić, S. Jeney, Ž. Sviben, A. J. Kulik, E.-L. Florin, and L. Forró, "Motion of a colloidal particle in an optical trap," *Physical Review E*, vol. 76, no. 1, p. 011112, 2007.

[111] S. Jeney, B. Lukić, J. A. Kraus, T. Franosch, and L. Forró, "Anisotropic memory effects in confined colloidal diffusion," *Physical review letters*, vol. 100, no. 24, p. 240604, 2008.

[112] T. Franosch and S. Jeney, "Persistent correlation of constrained colloidal motion," *Physical Review E*, vol. 79, no. 3, p. 031402, 2009.

[113] V. Garces-Chavez, D. McGloin, H. Melville, W. Sibbett, and K. Dholakia, "Simultaneous micromanipulation in multiple planes using a self-reconstructing light beam," *Nature*, vol. 419, no. 6903, p. 145, 2002.

[114] V. Zharov, T. Malinsky, and R. Kurten, "Photoacoustic tweezers with a pulsed laser: theory and experiments," *Journal of Physics D: Applied Physics*, vol. 38, no. 15, p. 2662, 2005.

[115] A. Samadi and N. S. Reihani, "Optimal beam diameter for optical tweezers," *Optics letters*, vol. 35, no. 10, pp. 1494–1496, 2010.

[116] S. Keen, J. Leach, G. Gibson, and M. Padgett, "Comparison of a high-speed camera and a quadrant detector for measuring displacements in optical tweezers," *Journal of Optics A: Pure and Applied Optics*, vol. 9, no. 8, p. S264, 2007.

[117] M. W. Allersma, F. Gittes, R. J. Stewart, C. F. Schmidt, *et al.*, "Two-dimensional tracking of ncd motility by back focal plane interferometry," *Biophysical journal*, vol. 74, no. 2, pp. 1074–1085, 1998.

[118] K. Svoboda and S. M. Block, "Force and velocity measured for single kinesin molecules," *Cell*, vol. 77, no. 5, pp. 773–784, 1994.

[119] O. Otto, J. Gornall, G. Stober, F. Czerwinski, R. Seidel, and U. Keyser, "High-speed video-based tracking of optically trapped colloids," *Journal of Optics*, vol. 13, no. 4, p. 044011, 2011.

[120] O. Otto, F. Czerwinski, J. L. Gornall, G. Stober, L. B. Oddershede, R. Seidel, and U. F. Keyser, "Real-time particle tracking at 10,000 fps using optical fiber illumination," *Optics express*, vol. 18, no. 22, pp. 22722–22733, 2010.

[121] S. F. Tolić-Nørrelykke, E. Schäffer, J. Howard, F. S. Pavone, F. Jülicher, and H. Flyvbjerg, "Calibration of optical tweezers with positional detection in the back focal plane," *Review of scientific instruments*, vol. 77, no. 10, p. 103101, 2006.

[122] K. C. Neuman and S. M. Block, "Optical trapping," *Review of scientific instruments*, vol. 75, no. 9, pp. 2787–2809, 2004.

[123] M. Sarshar, W. Wong, and B. Anvari, "Comparative study of methods to calibrate the stiffness of a single-beam gradient-force optical tweezers over various laser trapping powers," *Journal of biomedical optics*, vol. 19, no. 11, p. 115001, 2014.

[124] M. J. Villangca, D. Palima, A. R. Bañas, and J. Glückstad, "Light-driven micro-tool equipped with a syringe function," *Light: Science & Applications*, vol. 5, no. 9, p. e16148, 2016.

[125] A. van der Horst, P. D. van Oostrum, A. Moroz, A. van Blaaderen, and M. Dogterom, "High trapping forces for high-refractive index particles trapped in dynamic arrays of counterpropagating optical tweezers," *Applied optics*, vol. 47, no. 17, pp. 3196–3202, 2008.

[126] I. R. Perch-Nielsen, P. J. Rodrigo, and J. Glückstad, "Real-time interactive 3d manipulation of particles viewed in two orthogonal observation planes," *Optics express*, vol. 13, no. 8, pp. 2852–2857, 2005.

[127] P. Zemánek, A. Jonáš, L. Šrámek, and M. Liška, "Optical trapping of rayleigh particles using a gaussian standing wave," *Optics communications*, vol. 151, no. 4-6, pp. 273–285, 1998.

[128] P. W. Milonni and R. W. Boyd, "Momentum of light in a dielectric medium," *Advances in Optics and Photonics*, vol. 2, no. 4, pp. 519–553, 2010.

[129] M. A. Taylor, J. Knittel, and W. P. Bowen, "Fundamental constraints on particle tracking with optical tweezers," *New Journal of Physics*, vol. 15, no. 2, p. 023018, 2013.

[130] A. B. Stilgoe, T. A. Nieminen, G. Knöner, N. R. Heckenberg, and H. Rubinsztein-Dunlop, "The effect of mie resonances on trapping in optical tweezers," *Optics express*, vol. 16, no. 19, pp. 15039–15051, 2008.

[131] M. A. Taylor, "Optimizing phase to enhance optical trap stiffness," *Scientific Reports*, vol. 7, 2017.

[132] C. F. Bohren and A. J. Hunt, "Scattering of electromagnetic waves by a charged sphere," *Canadian Journal of Physics*, vol. 55, no. 21, pp. 1930–1935, 1977.

[133] M. A. Taylor and W. P. Bowen, "A computational tool to characterize particle tracking measurements in optical tweezers," *Journal of Optics*, vol. 15, no. 8, p. 085701, 2013.

[134] M. Mazilu, J. Baumgartl, S. Kosmeier, and K. Dholakia, "Optical eigenmodes; exploiting the quadratic nature of the energy flux and of scattering interactions," *Optics express*, vol. 19, no. 2, pp. 933–945, 2011.

[135] M. Mazilu and K. Dholakia, "Resonance enhanced optical manipulation: the push and pull of light," in *Optical Trapping and Optical Micromanipulation IX*, vol. 8458, p. 845809, International Society for Optics and Photonics, 2012.

[136] J. E. Curtis, B. A. Koss, and D. G. Grier, "Dynamic holographic optical tweezers," *Optics communications*, vol. 207, no. 1, pp. 169–175, 2002.

[137] K. D. Wulff, D. G. Cole, R. L. Clark, R. DiLeonardo, J. Leach, J. Cooper, G. Gibson, and M. J. Padgett, "Aberration correction in holographic optical tweezers," *Optics Express*, vol. 14, no. 9, pp. 4169–4174, 2006.

[138] B. Sun, Y. Roichman, and D. G. Grier, "Theory of holographic optical trapping," *Optics express*, vol. 16, no. 20, pp. 15765–15776, 2008.

[139] A. Farré, F. Marsà, and M. Montes-Usategui, "Optimized back-focal-plane interferometry directly measures forces of optically trapped particles," *Optics express*, vol. 20, no. 11, pp. 12270–12291, 2012.

[140] J. W. Tay, M. A. Taylor, and W. P. Bowen, "Sagnac-interferometer-based characterization of spatial light modulators," *Applied optics*, vol. 48, no. 12, pp. 2236–2242, 2009.

[141] D. Preece, R. Bowman, A. Linnenberger, G. Gibson, S. Serati, and M. Padgett, "Increasing trap stiffness with position clamping in holographic optical tweezers," *Optics express*, vol. 17, no. 25, pp. 22718–22725, 2009.

[142] A. Yao, M. Tassieri, M. Padgett, and J. Cooper, "Microrheology with optical tweezers," *Lab on a Chip*, vol. 9, no. 17, pp. 2568–2575, 2009.

[143] M. A. Taylor, J. Janousek, V. Daria, J. Knittel, B. Hage, H.-A. Bachor, and W. P. Bowen, "Biological measurement beyond the quantum limit," *Nature Photonics*, vol. 7, no. 3, pp. 229–233, 2013.

[144] C. Tischer, S. Altmann, S. Fisinger, J. H. Hörber, E. H. Stelzer, and E.-L. Florin, "Three-dimensional thermal noise imaging," *Applied Physics Letters*, vol. 79, no. 23, pp. 3878–3880, 2001.